AALBORG UNIVERSITY
STUDENT REPORT

Development of Control Strategies for the SvDP Concept

MASTER THESIS

Michael Otto Nielsen
Søren Juul Jensen

Aalborg University
- Department of Energy Technology

June 3rd 2014

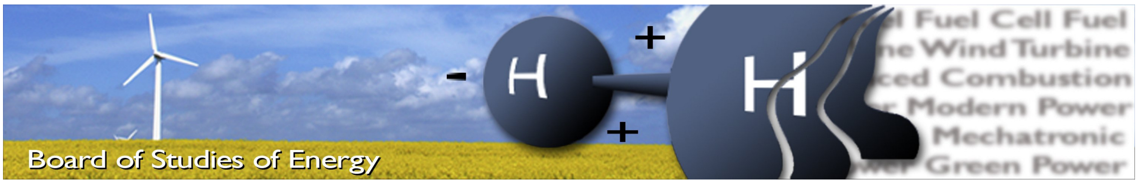

Title:	Development of Control Strategies for the SvDP-Concept
Semester:	10^{th} Semester, Spring 2014
Semester theme:	Master's Thesis
Project period:	February 3rd, 2014 - June 3rd, 2014
ECTS:	30
Supervisors:	Henrik C. Pedersen, Lasse Schmidt and Torben O. Andersen
Project group:	MCE4-1020

Michael Otto Nielsen

Søren Juul Jensen

SYNOPSIS:

In this project different control strategies are designed for the Speed-variable Differential Pump (SvDP)-concept. Initially a nonlinear mathematical model of the system is established. A steady state analysis of the system is then conducted to determine the challenges presented by the system. Several trajectories are designed to test the performance of the designed controllers. The model is simplified and linearized, enabling design of linear controllers for the system. Based on the linear model and the designed trajectories, the critical operating points are determined. Decentralized control strategies are designed, consisting of two sets of linear controllers with- and without pressure feedback. The controllers are implemented in the laboratory on a PLC. Due to noisy signals the controllers utilizing pressure feedback could not be implemented. An rms velocity error of 19.0 and 12.4 mm/s was obtained utilizing controllers without pressure feedback during positive and negative velocity, respectively. A performance of 2-3 mm/s rms velocity error is expected if the controllers with pressure feedback are successfully implemented.

Copies:	6
Pages, total:	141
Appendix:	20
Supplements:	CD attached

By signing this document, each member of the group confirms that all group members have participated in the project work, and thereby all members are collectively liable for the contents of the report. Furthermore, all group members confirm that the report does not include plagiarism.

Preface

This Master's Thesis has been submitted to the Institute of Energy Technology at Aalborg University in partial fulfillment of the requirements for the M.Sc. degree in Energy Engineering. The work has been carried out in cooperation with Aalborg University and Bosch Rexroth A/S.

Acknowledgment
The authors would like to thank the supervisors of the project; Lasse Schmidt, Henrik C. Pedersen and Torben O. Andersen for assistance and feedback throughout the project. Furthermore, we would like to thank our fellow student Chris W. Nielsen for help in the laboratory and for always being available.

Finally, the authors would especially like to thank Thomas Kallestrup, SAE Coordinator at Bosch Rexroth, for help with the test setup in the laboratory, without whom experiments would not be possible.

Reading guide
Chapters in this thesis consist of sections and subsections. Throughout the report, these will be referred to as "Chapter.Section.Subsection". Appendices are named in alphabetic order. Figures are denoted as "Chapter.Figure number". Equations are likewise referred to as (Chapter.Equation number). Sources are referred to by usage the Harvard method (Author,Year of publication). On the back cover of the report, a CD is attached. This CD contains a PDF version of the report, m-scripts, simulink models and relevant data sheets.

Contents

Abstract

The Speed-variable Differential Pump (SvDP)-concept, designed by Bertelsen and Madsen (2013) in collaboration with Bosch Rexroth A/S, is intended to be an alternative to the classic hydraulic setup, which utilizes a valve to direct the oil flow. The valve is replaced with two pumps mounted on the same servo drive, resulting in a higher energy efficiency of the hydraulic system.

Initially, a nonlinear simulation model of the system is established. The simulation model is verified using experimental measurements, obtained in the test facility provided by Bosch Rexroth A/S. To highlight the properties of the SvDP-concept, a thorough steady state analysis of the system is performed. The analysis of the system reveals that the system pressure levels rise when the direction of rotation in the pumps is negative, while the pressure levels always decrease when the direction of rotation is positive. This means that the pressures, in the current configuration of the SvDP-concept, can only be controlled during negative rotation of the pumps.

Two types of trajectories are designed to evaluate the performance of the designed controllers. Two trajectories based on quintic functions are designed, ensuring realizable demands to acceleration and velocity of the piston. In addition to the quintic trajectories, two ramp based trajectories are designed, which require step in velocity.

The model is linearized, and the critical operating points are identified, based on the results of the steady state analysis and the designed trajectories. The linear system, in the critical operating points, results in two linear systems depending on the direction of rotation. A decentralized control strategy is designed for the two linear systems, such that SISO control can be applied. Two sets of controllers are designed, due to limitations in the test facility, where a poor velocity estimate is available. A set of conservative controllers are designed, which can be implemented and tested despite the limitations, and a set of high performance controllers are designed to prove the potential of the SvDP-concept. The high performance controllers utilize pressure feedback to improve the damping of the system, but the proportional gain of the PI-controllers regulating the velocity, prevents implementation, as a noisy position signal results in chattering of the control signal.

The conservative controllers are implemented and tested, resulting in a proof of concept. The rms velocity error, obtained from the experimental results, deviate from the simulations by 23-55 %. Assuming this deviation applies to the simulation results, for the high performance controllers, an rms velocity error of 2-3 mm/s can be expected, when a decent velocity feedback is available. It is therefore concluded that the SvDP-concept can be an alternative to the traditional valve-cylinder configuration.

Resumé

Hastigheds variabel differentialpumpe (SvDP)-konceptet, designet af Bertelsen og Madsen i samarbejde med Bosch Rexroth A/S, har til formål at være et alternativ til den klassiske hydraulikopsætning, hvor en ventil bruges til at styre olieflowet. Ventilen er erstattet af to pumper, som er monteret på samme aksel, hvilket resulterer en højere energieffektivitet af det hydrauliske system.

Indledningsvist er en ulineær simulerings model af systemet etableret. Simuleringsmodellen er verificeret ved hjælp af eksperimentelle målinger fra laboratoriet. For at belyse egenskaberne af SvDP-konceptet, er en grundig stationær analyse af systemet udført. Analysen af systemet afslører at trykket i systemet stiger når omløbsretningen på pumperne er negativ, hvorimod trykket altid falder når omløbsretningen er positiv. Det betyder at trykket kun kan kontrolleres ved negativ omløbsretning af pumperne.

To typer af trajektorier er designet til at evaluere ydelsen af de designede regulatorer. To trajektorier, baseret på femtegrads polynomier, er designet for at sikre at kravene til acceleration og hastighed er realiserbare. Ud over disse trajektorier, er to rampe baserede trajektorier designet, som kræver spring i hastighed.

Modellen er lineariseret og de kritiske operationspunkter er identificeret på baggrund af den indledende system analyse, samt de designede trajektorier. Det lineære system, evalueret i de kritiske operationspunkter, resulterer i to lineære systemer, som afhænger af omløbsretningen. En decentraliseret kontrolstrategi er designet for de to lineære systemer for at SISO kontrol kan anvendes. Grundet begrænsninger i laboratoriet, hvor kvaliteten af hastigheds signalet er lav, designes to sæt regulatorer. Et sæt regulatorer er designet konservativt, sådan at disse kan testes, på trods af den lave kvalitet af hastigheds signalet. Derudover er et sæt regulatorer designet til at vise den potentielle ydeevne af systemet. Regulatorerne, designet for høj ydeevne, anvender tilbagekobling af det virtuelle lasttryk for at øge dæmpningen i systemet. Proportionalforstrækningen i hastighedsregulatorerne umuliggør implementering, da det støjfyldte hastigheds signal resulterer i et uhensigtsmæssigt kontrol signal.

De konservativt designede regulatorer er implementeret og testet i laboratoriet og viser at konceptet virker. Rms hastighedsfejlen, målt i laboratoriet, afviger fra simuleringerne med 23-55 %. Hvis det antages at denne afvigelse også er repræsentativ for simuleringerne med høj-ydeevne-regulatorerne, kan det forventes at opnå en rms hastigheds fejl på 2-3 mm/s. Det er derfor konkluderet at SvDP-konceptet kan anvendes som et alternativ til den traditionelle ventil-cylinder løsning.

Introduction to the SvDP-concept 1

In cooperation with Bosch Rexroth A/S, the M.Sc. students Bertelsen and Madsen (2013) have designed and developed a Speed-variable Differential Pump concept. The SvDP-concept is intended as an energy efficient alternative to a traditional cylinder actuation system, consisting of a hydraulic pump connected to for example a 4/3-valve. To outline the differences between the two concepts, an illustration is provided. To the left in figure 1.1, a simplified illustration of a traditional actuation system for a hydraulic cylinder is given. The SvDP-concept is illustrated to the right.

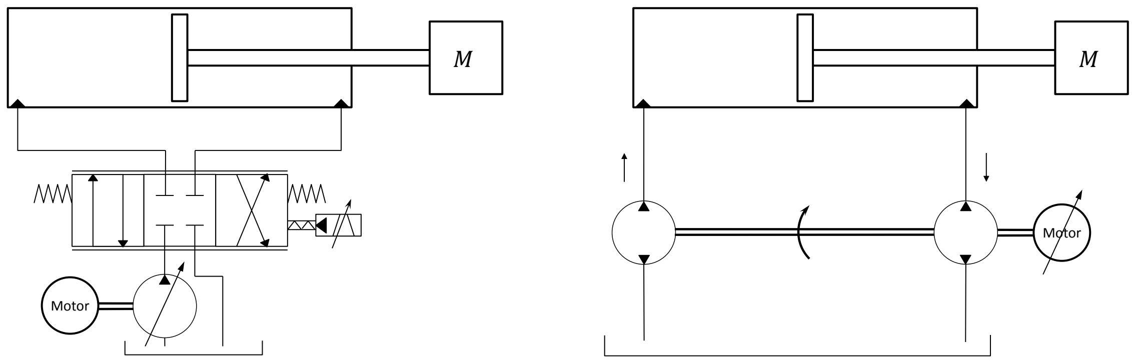

Figure 1.1. Left: Example of a traditional hydraulic actuation system with a valve-cylinder configuration. Right: Simple schematic of the SvDP-concept.

The differences are outlined in the following by a short introduction to the two configurations:

- **Conventional valve-cylinder configuration:**
  In the conventional valve-cylinder configuration, the flow rate is controlled by the valve, mounted between the pump and the actuator. By controlling the flow rate, the velocity of the piston is controlled. In this configuration a given supply pressure is needed to actuate the cylinder, depending on the magnitude of the load. Many configurations are available to supply the system, where examples could be a fixed displacement pump driven at constant speed or by a servo drive. Another example could be a variable displacement pump driven at constant speed etc.

  To reduce the purchase price of the actuation system, a fixed displacement pump is commonly utilized in the industry. Such pumps are cheap, compared to variable displacement pumps, but come with the disadvantage of making the system inefficient with respect to energy consumption. The systems are normally designed to handle the maximum expected demands, where a safety margin is added. When the pump is operated at a fixed speed, the excessive flow rate needs to be throttled. The excessive flow rate is commonly throttled to the tank, by a pressure relief valve connected in parallel with the pump. Throttling of the excessive flow rate, results in a power loss that is equal to the flow rate times the pressure drop. This energy loss can be quite extensive and undesirable as it heats the fluid, whereby cooling elements are required.

- **SvDP-concept:**
  The SvDP-concept, illustrated to the right in 1.1, is developed from the idea of reducing the energy losses, caused by throttling of excessive flow without increasing the purchase price of the actuation system. The idea of the concept is to match two fixed displacement pumps to the area ratio of the piston and drive the pumps simultaneously, with opposite flow directions by a servo drive. Thereby a constant supply pressure is avoided and only the flow rate, needed to complete the desired task, is pressurized to balance the load. Doing this, the pressure losses in the system are reduced, compared to the conventional valve-cylinder configuration, which is shown in (Bertelsen and Madsen, 2013).

1.1 Motivation for the Thesis

As the valve-cylinder configuration has been the industry standard for years, the concept is well-known and reliable. Many types of control strategies have been developed, both linear and nonlinear, ensuring robustness and good tracking abilities of the actuation system. However, the valve configuration results in a pressure drop across the valve, resulting in power losses. As a result, the energy efficiency of such hydraulic systems can be fairly low. By omitting the valve, the pressure drop can be avoided, whereby a higher energy efficiency can be obtained.

In order for the SvDP-concept to be a feasible alternative to the valve configuration, the performance of the system must match the performance of a valve operated system. Furthermore, the price of the system must be competitive with the conventional valve-cylinder configuration. This means, the alternative must consist of cheap off-the-shelf products and the number of sensors must be kept at a minimum.

The motivation for the studies is to determine whether the SvDP-concept can be an alternative to the traditional valve setup illustrated in figure 1.1 (left). The aim is not to make a direct comparison of the two configurations. This was done by Bertelsen and Madsen (2013), which showed that the SvDP-concept, in two different test scenarios, only uses 47.7 % and 62.0 % of the energy consumed by a reference system, consisting of a conventional valve-cylinder combination, supplied by a variable displacement pump. Due to time limitations Bertelsen and Madsen (2013), were not able to design a feasible set of controllers, which included control of the pressure levels. The starting point of the studies, conducted in this thesis, is therefore to continue the work performed by Bertelsen and Madsen (2013). The main focus will not be energy efficiency of the system, but to clarify the properties and potential of the SvDP-concept as an actuation system.

1.2 Aims of the Thesis

The aim of this thesis is to clarify the properties and potential of the SvDP-concept as an actuation system. In order to do so, an analysis of the test setup, provided by Bosch Rexroth A/S, is conducted. Based on this, the aim is to design a set of controllers for testing the system. The purpose of the controllers is to make a proof of concept, with regards to the capabilities of the system and the achievable tracking performance. Finally, the goal is to evaluate the potential of the SvDP-concept, in its current configuration, and based on the analysis of the concept, to provide suggestions for improvements to eliminate undesirable properties.

1.3 Dissertation Outline

In chapter 2, a simulation model of the test facility is established. This includes a mathematical description of the SvDP-concept and the backhoe loader serving as manipulator in the test setup. The simulation model is adjusted and validated by comparison with experiments. In chapter 3, the system is analyzed at steady state piston velocity, to identify the properties of the SvDP-concept and the steady state behavior of the system. Based on the initial analysis, considerations are made on a control scheme for the actuation system.

Trajectories, used for performance evaluation, are designed in chapter 4, which also includes initial tests to determine the pump speed required to have a significant pressure buildup in the system. In chapter 5, the model is linearized and the characteristics of the system are examined. From studies of the hydro-mechanical dynamics, two critical operation points are found with respect to the lowest eigenfrequency. Hereafter, the dynamics of the system are verified by comparison with the nonlinear model and a reduced order linear model is established for simplicity and clarity in the description of the system dynamics.

The technical challenges are outlined in the problem statement, chapter 6. A decentralized control structure is suggested in chapter 7 and controllers are designed to track the designed reference trajectories while maintaining a low pressure in the system. The controllers are implemented in the test setup up and the performance is evaluated in chapter 8.

In chapter 9, the results and conclusions of the thesis, are given. The results are put into perspective in chapter 10, where suggestions for improving the SvDP-concept, are given.

Modeling and Verification the of Hydraulic System 2

A simulation model of the system is developed throughout this chapter. The derivation and documentation of the model is limited to the hydraulic parts, connected to the outer link of a backhoe loader. As previously mentioned, this hydraulic concept was developed and designed by Bertelsen and Madsen (2013). The purpose of the chapter is to establish a nonlinear simulation model of the hydraulic parts, which is to be verified using data from an open-loop experiment. The verified simulation model is hereafter used as a tool to identify potential problems in the SvDP-concept. Furthermore, it is used to test different control strategies that will be developed throughout the project. It is therefore essential that the simulation model is reasonably accurate, such that decisions on physical implementation can be made. Based on this argumentation the simulation model must include all components present in the physical setup, including the safety features. In figure 2.1, a sketch of the hydraulic diagram is provided with notations used throughout the derivation of a simulation model.

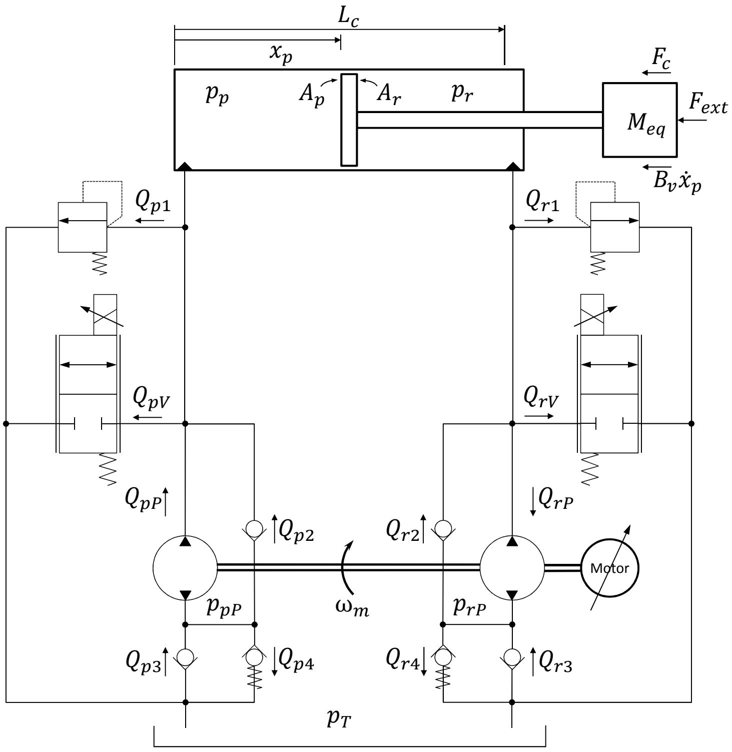

Figure 2.1. Schematic of the hydraulic system connected to the backhoe loader.

The system consists of an electric servo-drive connected to two external gear pumps. These are closely matched to the area ratio of the asymmetric cylinder, that actuates the back-shovel of the backhoe loader. In each line connecting the pumps to the cylinder, a high-performance 2/2 proportional directional valve is present to regulate the line pressures. In the same lines, a direct operated pressure relief valve is mounted as a safety feature in case of overpressure in the lines. The pressure relief valves can be set manually, but are currently set to 170 and 200 bar at the piston- and rod side of the cylinder, respectively.

Two plain check valves and one spring loaded check valve are mounted in a configuration around each pump, serving as an anti-cavitation circuit. The spring loaded check valve in the anti-cavitation circuit causes the chambers P_{pP} and P_{rP} to act as a *virtual pressurized tank*. The virtual pressurized tank ensures a minimum pressure on the back side of the pumps, which ensures a minimum pressure level in the two piston chambers. (Bertelsen and Madsen, 2013) The cracking pressure of the spring loaded check valve is 2.5 bar, ensuring a minimum pressure in the system of 2.5 bar.

2.1 Nonlinear Modeling of the SvDP-concept

In this section an overall model derivation is given, describing the system in terms of the force balance on the cylinder and continuity equations describing the pressures in the lines. The model derivation utilizes the notations given in figure 2.1 on the preceding page.

In equation (2.1) Newton's 2nd law has been applied to the cylinder, setting up the force balance of the actuator.

$$M_{eq} \cdot \ddot{x}_p + B_v \cdot \dot{x}_p + F_c + F_{ext} = A_p \cdot p_p - A_r \cdot p_r \tag{2.1}$$

where:

B_v	Viscous friction coefficient	$\left[\frac{\mathrm{N \cdot s}}{\mathrm{m}}\right]$
F_c	Coulomb friction	[N]
F_{ext}	External forces	[N]
M_{eq}	Equivalent mass acting on the cylinder	[kg]
$\ddot{x}_p$	Acceleration of the piston	$\left[\frac{\mathrm{m}}{\mathrm{s}^2}\right]$

The numerical value of the constant physical quantities are listed in Appendix A, while the variables are clarified further. The friction model F_c is implemented as pure Coulomb friction, but to avoid numerical problems, related to discontinuities, the hyperbolic tangent function is used rather than a *sign* function. The gradient of the hyperbolic tangent around zero velocity is implemented as a tuning factor in the simulation model. Ideally, the gradient should be infinite.

The pressures p_p and p_r are determined by applying the continuity equation to the lines connected to cylinder chambers. This is given in equation (2.2) and (2.3) for the piston- and rod side, respectively.

$$Q_{pP} + Q_{p2} - Q_{pV} - Q_{p1} - Q_{pL} = A_p \cdot \dot{x}_p + \frac{A_p \cdot x_p + V_{pline}}{\beta_p} \cdot \dot{p}_p \tag{2.2}$$

$$-Q_{rP} + Q_{r2} - Q_{rV} - Q_{r1} - Q_{rL} = -A_r \cdot \dot{x}_p + \frac{A_r \cdot (L_c - x_p) + V_{rline}}{\beta_r} \cdot \dot{p}_r \tag{2.3}$$

where:

β_p, β_r	Stiffness of the oil in the piston- and rod side chamber	[Pa]
L_c	Total stroke length	[m]
Q_{pP}, Q_{rP}	Pump flow from the piston- and rod side pump	$\left[\frac{\mathrm{m}^3}{\mathrm{s}}\right]$
Q_{p1}, Q_{r1}	Flow in pressure relief valve at the piston- and rod side line	$\left[\frac{\mathrm{m}^3}{\mathrm{s}}\right]$
Q_{p2}, Q_{r2}	Flow in check valve parallel to the piston- and rod side pump	$\left[\frac{\mathrm{m}^3}{\mathrm{s}}\right]$
Q_{pV}, Q_{rV}	Flow in proportional valve at the piston- and rod side line	$\left[\frac{\mathrm{m}^3}{\mathrm{s}}\right]$
Q_{pL}, Q_{rL}	Leakage flow in the the piston- and rod side line	$\left[\frac{\mathrm{m}^3}{\mathrm{s}}\right]$
V_{pline}, V_{rline}	Hose volume of the lines at the piston- and rod side	$\left[\mathrm{m}^3\right]$

The leakage flows given by Q_{pL} and Q_{rL} in equation (2.2) and (2.3), are not illustrated in figure 2.1 on page 5, as these flows can not be uniquely identified. These flows relate to any leakage there may be across the valves, out of the cylinder and unmodeled leakage across the pumps. It is assumed that the leakage flow is laminar and Dryden's leakage formula is therefore applied. The leakage is thereby modeled as in equation (2.4), which states that the leakage flow is a linear function of the pressure in the respective line.

$$Q_{iL} = p_i \cdot C_{iLeak} \tag{2.4}$$

Rearranging equation (2.2) and (2.3) reveals the pressure gradient in the individual line. The pressure gradients are a function of the flow rates in the system, the stiffness of the fluid, the velocity and position of the piston in the actuator. The pressure gradients are shown in equation (2.5) and (2.6).

$$\dot{p}_p = \frac{\beta_p}{A_p \cdot x_p + V_{pline}} \cdot (Q_{pP} + Q_{p2} - Q_{pV} - Q_{p1} - Q_{pL} - A_p \cdot \dot{x}_p) \tag{2.5}$$

$$\dot{p}_r = \frac{\beta_r}{A_r \cdot (L_c - x_p) + V_{rline}} \cdot (-Q_{rP} + Q_{r2} - Q_{rV} - Q_{r1} - Q_{rL} + A_r \cdot \dot{x}_p) \tag{2.6}$$

Using the same procedure, the pressure gradients on the low pressure side of pumps are determined. The pressures are denoted p_{pP} and p_{rP} for the piston- and rod-side pump respectively. Their gradients are given in equation (2.7) and (2.8).

$$\dot{p}_{pP} = \frac{\beta_{pP}}{V_{pP}} \cdot (Q_{p3} - Q_{pP} - Q_{p4} - Q_{p2}) \tag{2.7}$$

$$\dot{p}_{rP} = \frac{\beta_{rP}}{V_{rP}} \cdot (Q_{r3} + Q_{rP} - Q_{r4} - Q_{r2}) \tag{2.8}$$

where:

β_{pP}, β_{rP}	Bulk modulus in the control volumes at the low pressure side of the pumps	[Pa]
Q_{p3}, Q_{r3}	Flow in check valves connected in series with the pumps	$\left[\frac{m^3}{s}\right]$
Q_{p4}, Q_{r4}	Flow in spring loaded check valves connected in series with the pumps	$\left[\frac{m^3}{s}\right]$

The equations (2.1) and (2.5)→(2.8) provide a description of the actuator movement and the line pressures needed to model the system. In the following subsections, the individual components are examined to determined the respective flow rates, depending on the pressure levels and command signals. Furthermore, a model of the fluid stiffness is established as this also changes considerably with the pressure levels and the air content of the fluid.

2.1.1 Pressure Relief Valves

For the safety of the system, two pressure relief valves (PRV) are connected to each cylinder chamber. Their purpose is to relieve the line pressure by leading some of the oil directly to the tank in case of overpressure. At the piston side the maximum pressure is set to 170 bar, while it at the rod side is set to 200 bar. The main specifications of the PRV's, used in the test-setup, are listed in table 2.1 and the static operation curves are given in figure 2.2.

Description	Data
Product #	DBDS20 G1X/200 (size 20)
Maximum inlet pressure	400 bar
Designed pressure range	200 bar

Table 2.1. Direct Operated Pressure Relief Valve specifications. (Rexroth, 1998)

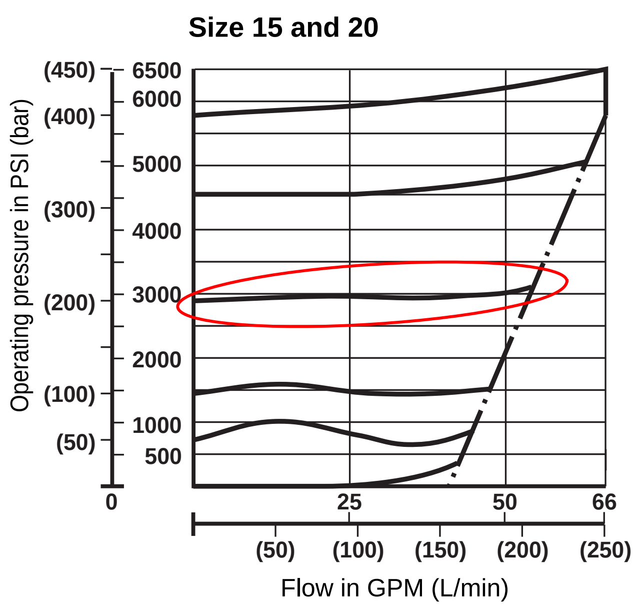

Figure 2.2. Static operation curves of PRV *DBDS20 G1X/200* from (Rexroth, 1998).

Based on the setting of the crack-pressure around 200 bar in the physical setup, the gradient of the third curve from the top in figure 2.2, is used to make a mathematical description of the PRV. It is assumed that the flow rate will not exceed 200 L/min and therefore the saturation curve is omitted in the model. This leads to the description in equation (2.9). The subscript i is utilized rather than p and r, as the equation applies to both sides of the actuator.

$$Q_{i1} = \begin{cases} 0 & p_i < p_{i,crack} + p_T \\ Q\left(p_i\right) & p_i \geqq p_{i,crack} + p_T \end{cases} \tag{2.9}$$

In the data sheet, provided by Rexroth (1998), there is no information about the dynamic behavior of the PRV. It is therefore assumed that the valve dynamics can be modeled as a first order system, with a reasonably fast response. For modeling purposes, it is arbitrary assumed that the valves have a time constant of 2 ms. Therefore the flow rate $Q\left(p_i\right)$ is approximated by (2.10).

$$Q\left(p_i\right) = \frac{k_{PRV}}{1 + \tau_{PRV} \cdot s} \cdot \left(p_i - p_{i,crack} - p_T\right) \tag{2.10}$$

where:

k_{PRV}	Gradient of flow curve in figure 2.2 on the facing page	[Pa]
p_i	Pressure in the respective chamber	[Pa]
$p_{i,crack}$	Crack pressure of the PRV connected to the respective chamber	[Pa]
p_T	Tank pressure	[Pa]
$Q(p_i)$	PRV flow as function of the differential pressure	$\left[\frac{\mathrm{m}^3}{\mathrm{s}}\right]$
τ_{PRV}	Time constant of PRV	[s]

The parameter k_{PRV} is determined based on the PRV's static performance in figure 2.2 on the preceding page, under the assumption that there is a linear correlation between the flow rate and differential pressure. Normally an orifice in a valve would be described using the orifice equation, under the assumption of turbulent flow in the orifice. But due to the almost linear flow versus pressure characteristics of the PRV, this approach is not chosen here.

2.1.2 2/2 Proportional Directional Valve

For controlling the line pressures, a 2/2 high performance Proportional Directional Valve (PDV) is mounted between the pump and the respective actuator chamber. Depending on the differential pressure across the valve, it is capable of leading fluid in and out of the lines to increase or decrease the pressure level. In this system it will only be capable of reducing the line pressure, as this will always be higher than the tank pressure due to the anti-cavitation feature that prevents cavitation in the cylinder. In table 2.2 on the following page the main specifications of the PDV are given.

Description	Data
Product #	KKDSR1NB/HCG24N0K4V
Maximum operating pressure	350 bar
Maximum flow	38 ($1 \rightarrow 2$), 34 ($2 \rightarrow 1$) L/min
Step response 0 to 100 % & 100 to 0 %	< 65 ms
Hysteresis	≤ 5 %
Response sensitivity	≤ 1 %
Supply voltage	24 V
Maximum solenoid current	1.2 A

Table 2.2. 2/2 Proportional Directional Valve specifications. (Rexroth, 2005)

From the specifications of the PDV given in the data sheet (Rexroth, 2005), it is clear that the flow rate depends on the flow direction, however, only the direction ($2 \rightarrow 1$) is utilized in the test setup. In figure 2.3 the flow rate is illustrated as a function of the command signal, given in percentage, and the differential pressure given in bar.

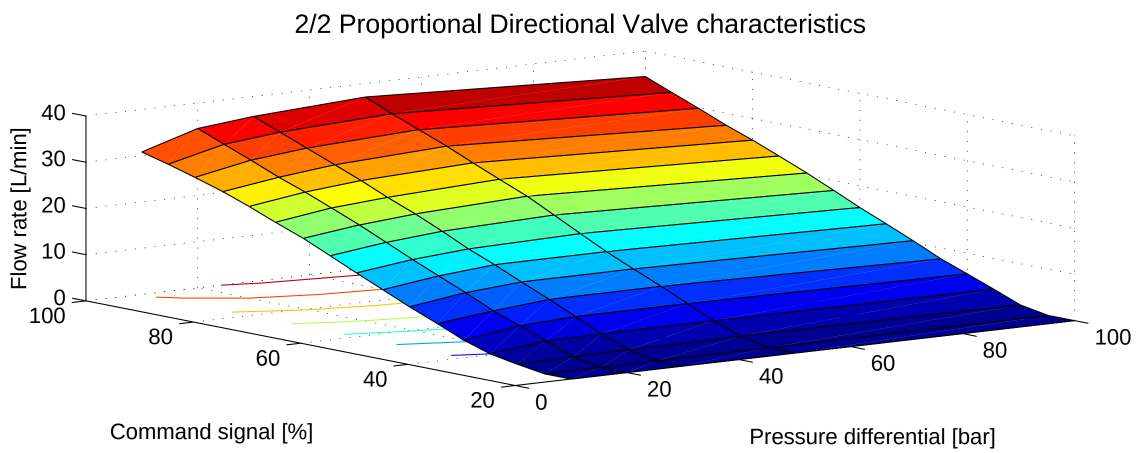

Figure 2.3. Static operation curves of 2/2 Proportional Directional Valve. Data from (Rexroth, 2005).

It should be noted that the flow rate is relatively proportional to the command signal as expected, while the pressure dependency differs from ordinary PDV's. Normally, the flow rate is proportional to the square root of the differential pressure, but in this PDV there is a pressure compensation that changes its characteristics. Therefore the standard modeling approach of utilizing the orifice equation is not chosen here. Instead, the flow characteristics are implemented in the simulation model using a look-up table with linear interpolation. The linear interpolation is considered sufficient due to the relatively smooth surface. The dynamics of the PDV is implemented as a first order system with a time constant of 16 ms in accordance with the specifications listed in table 2.2.

2.1.3 Check valves (with and without spring)

To prevent cavitation in the system, Bertelsen and Madsen (2013) designed and implemented a configuration of check valves (CV), consisting of two regular CV's and one spring-loaded, in each line. This configuration ensures that the pressure cannot drop below the tank pressure in any of the lines. The main specifications of the CV's are listed in table 2.3 and the static operation curves are given in figure 2.4. Note the curve marked as (2) is the operation curve of the spring loaded CV and (0) marks the regular CV.

Description	Data
Product # without spring	S 30 A0.0/
Product # with spring	S 30 A2.0/
Maximum operating pressure	315 bar
Maximum flow	450 L/min

Table 2.3. Check valve specifications. (Rexroth, 2006)

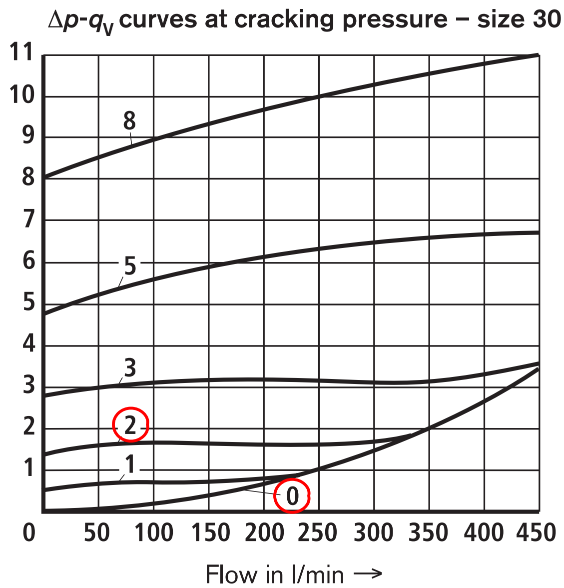

Figure 2.4. Static operation curves of CV *S 30 A0.0/* (0) & *S 30 A2.0/* (2) from (Rexroth, 2006).

From the static operation curves in figure 2.4, it is clear that the regular CV has a characteristic similar to a sharp edge orifice. Therefore these CV's are modeled using the orifice equation. This is given in equation (2.11) for the CV mounted in parallel with the pump.

$$Q_{i2} = \begin{cases} 0 & p_i > p_{iP} \\ k_{CV} \cdot \sqrt{p_{iP} - p_i} & p_i \leq p_{iP} \end{cases} \tag{2.11}$$

It is assumed that the regular CV can be considered as an on/off valve, that is either fully open or completely closed without leakage. The flow rate only depends on the differential pressure. This leads to the assumption of a constant flow gain denoted k_{CV}. The numerical value of k_{CV} is listed in Appendix A. Using the same assumptions, yields the model of the CV placed between the pump and tank, given in equation (2.12).

$$Q_{i3} = \begin{cases} 0 & p_{iP} > p_T \\ k_{CV} \cdot \sqrt{p_{iP} - p_T} & p_{iP} \leq p_T \end{cases} \tag{2.12}$$

From figure 2.4 on the preceding page it is clear that the spring loaded CV has a different characteristic than a sharp edged orifice. Due to the spring mounted in the valve, it has a crack pressure depending on the stiffness of the spring. The spring loaded CV, mounted in the SvDP-concept, cracks open when the differential pressure is 1.5 bar. A model of this CV is given in equation (2.13).

$$Q_{i4} = \begin{cases} 0 & p_{iP} < p_{spring} + p_T \\ Q\left(p_{iP}\right) & p_{iP} \geq p_{spring} + p_T \end{cases} \tag{2.13}$$

To avoid discontinuities in a mathematical model, it is desirable to include the valve dynamics. This data is not available from (Rexroth, 2006) and it is therefore assumed to behave as a first order system with a time constant τ_{CV}. This is shown in equation (2.14).

$$Q\left(p_{iP}\right) = \frac{1}{1 + \tau_{CV} \cdot s} \cdot Q\left(p_{iP}\right) \tag{2.14}$$

It should be noted from figure 2.4 on the previous page that the differential pressure varies slightly with the flow rate. Therefore the flow rate of the spring loaded check valve $Q\left(p_{iP}\right)$ is implemented using a look-up table with linear interpolation.

2.1.4 Servo Drive

The supply system in the SvDP-concept consists of a servo drive connected to two external gear pumps. No documentation is available for the servo drive used in the test setup and the characteristics are therefore examined using experimental results. The servo drive contains an internal control structure, serving as a speed control. Based on this knowledge the servo drive is approximated using a second-order system, in which the parameters are to be identified. The model is given in equation (2.15).

$$\omega_m = \frac{\omega_{n,m}^2}{s^2 + 2 \cdot \zeta_m \cdot \omega_{n,m} \cdot s + \omega_{n,m}^2} \cdot \omega_{ref,m} \tag{2.15}$$

where:

ω_m	Actual rotational speed of the shaft	$\left[\frac{\text{rad}}{\text{s}}\right]$
$\omega_{ref,m}$	Speed reference for the servo-system	$\left[\frac{\text{rad}}{\text{s}}\right]$
$\omega_{n,m}$	Natural frequency of the servo-system	$\left[\frac{\text{rad}}{\text{s}}\right]$
ζ_m	Damping ratio of the servo-system	[-]

The natural frequency and the damping ratio, are obtained from the validation experiments presented in section 2.2. The natural frequency of the servo-system is found at approximately 100 Hz and the damping ratio is 0.35.

2.1.5 External Gear Pumps

To drive the actuator, two external gear pumps are connected to the servo drive with opposite direction of rotation. The ratio of the pump sizes are chosen as the closest match to the area ratio in the cylinder by Bertelsen and Madsen (2013). The specifications of these pumps are given in table 2.4, with the common features listed in the bottom.

Description	Data
Product #	AZPFF-22-028RHO3030KB-S9997
Displacement	28 cm^3/rev
Maximum continuous pressure	170 bar
Maximum peak pressure	240 bar
Product #	AZPFF-22-014RHO3030KB-S9997
Displacement	14 cm^3/rev
Maximum continuous pressure	250 bar
Maximum peak pressure	300 bar
Suction pressure	0.7-3.0 bar
Minimum rotational speed	500 rpm
Maximum rotational speed	3000 rpm

Table 2.4. Specifications of External Gear Pumps. (Rexroth, 2012)

In addition to the information listed in table 2.4, classified experimental test information about the pumps, have been provided in (Rexroth, 2010) and (Rexroth, 2009). Based on these test results, mappings of the pump efficiencies have been obtained. The pumps are modeled by equation (2.16), stating that the pump flow is proportional to the shaft speed, scaled by the fixed displacement and the volumetric efficiency.

$$Q_{iP} = D_i \cdot \eta_{iv} \cdot \omega_m \tag{2.16}$$

where:

D_i	Pump displacement	$\left[\frac{\mathrm{m}^3}{\mathrm{rad}}\right]$
η_{iv}	Volumetric efficiency of the pump	[-]
Q_{iP}	Pump flow	$\left[\frac{\mathrm{m}^3}{\mathrm{s}}\right]$

The displacement of the pump is fixed, but due to leakage in the pump the effective displacement is lower and variable, depending on the amount of leakage. Therefore the factor η_{iv} is introduced in equation (2.16). η_{iv} is the volumetric efficiency, which has been experimentally obtained by Rexroth (2010) and Rexroth (2009) for the 28 cm^3/rev and 14 cm^3/rev pump, respectively. The volumetric efficiencies are illustrated in figures 2.5 and 2.6 on the following page, as a function of the differential pressure and the shaft speed of the pump. Note that the scales are not equal in the figures.

The volumetric efficiencies are implemented in the nonlinear simulation model as look-up tables with linear interpolation.

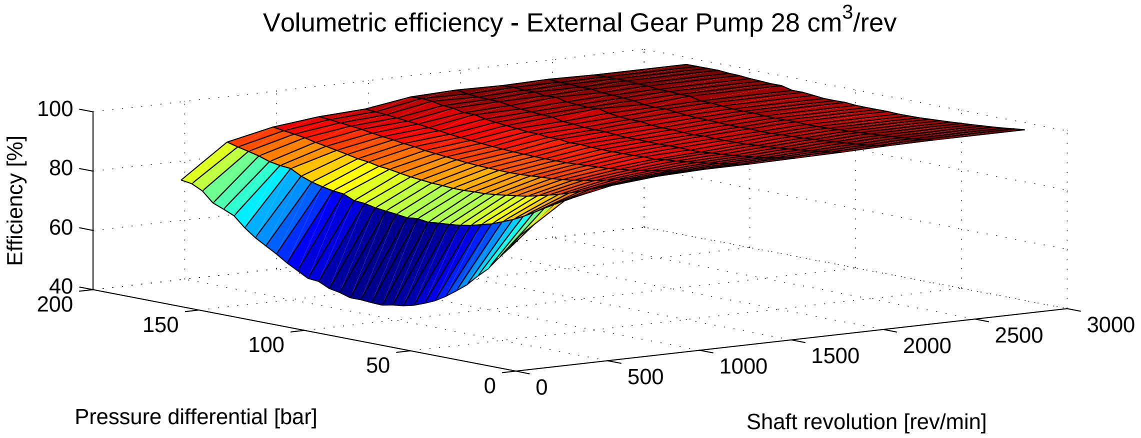

Figure 2.5. Volumetric efficiency 28 cm^3/rev gear pump. Experimental results (Rexroth, 2010).

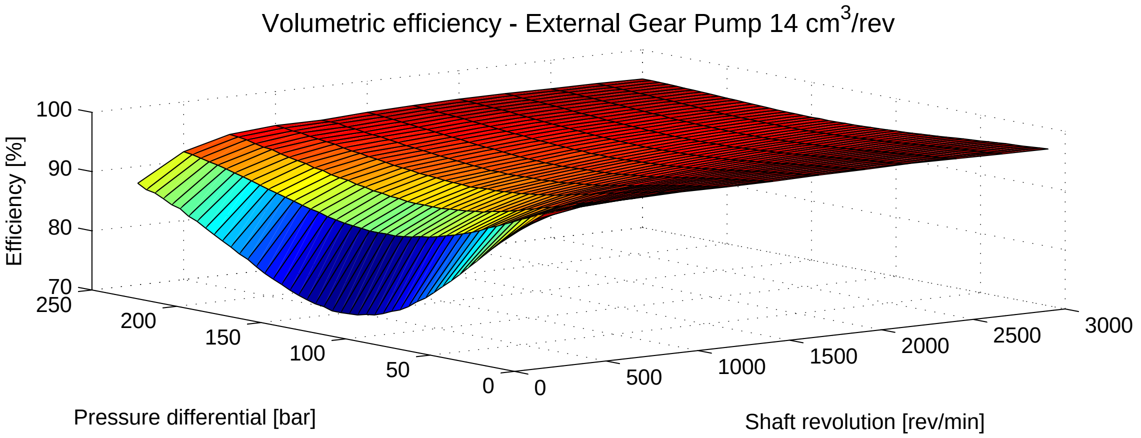

Figure 2.6. Volumetric efficiency 14 cm^3/rev gear pump. Experimental results (Rexroth, 2009).

2.1.6 Fluid Stiffness

To account for the varying compressibility of the hydraulic oil, which depends on the pressure, air content and temperature, a bulk modulus model is implemented in the four control volumes of the simulation model. To simplify the model into parameters that are measurable in the test setup, it is assumed that the air content of the fluid is constant and a constant operation temperature of 40°C is maintained. This simplification is considered reasonable, as the system operates with cooling/heating elements that maintain the fluid temperature at a desired level and where air only can mix with the fluid in the tank. Due to these assumptions the bulk modulus model simplifies to equation (2.17) (Andersen, 2003).

$$\beta_i = \frac{1}{\frac{1}{\beta_F} + \varepsilon_A \cdot \left(\frac{1}{\beta_A} - \frac{1}{\beta_F} \right)} \tag{2.17}$$

where:

β_i	Effective bulk modulus in the control volume i	[Pa]
β_A	Stiffness of air	[Pa]
β_F	Stiffness of the hydraulic oil	[Pa]
ε_A	Volumetric ratio of air content in the fluid	[-]

The stiffness of the air, contained in the fluid, is given by equation (2.18) (Andersen, 2003). The volumetric air ratio, trapped in the fluid, is a variable that depends on the pressure level of the fluid. This volumetric air ratio is found using equation (2.19) assuming a constant fluid temperature (Andersen, 2003).

$$\beta_A = c_{ad} \cdot p_i \tag{2.18}$$

$$\varepsilon_A = \frac{1}{\left(\frac{1-\varepsilon_{A0}}{\varepsilon_{A0}}\right) \cdot \left(\frac{p_{atm}}{p_i}\right)^{\frac{-1}{c_{ad}}} + 1} \tag{2.19}$$

where:

c_{ad}	Adiabatic constant of air	[-]
ε_{A0}	Volumetric ratio of air content in the fluid at p_{atm}	[-]
p_{atm}	Atmospheric pressure	[Pa]

The reference of the volumetric air ratio ε_{A0} is difficult to estimate, but it is assumed that air is let out properly, which can result in an air content lower than 1 % (Andersen, 2003). Using this information and a stiffness of the hydraulic oil β_F of 10.000 bar, the effective bulk modulus is given in figure 2.7 as a function of pressure.

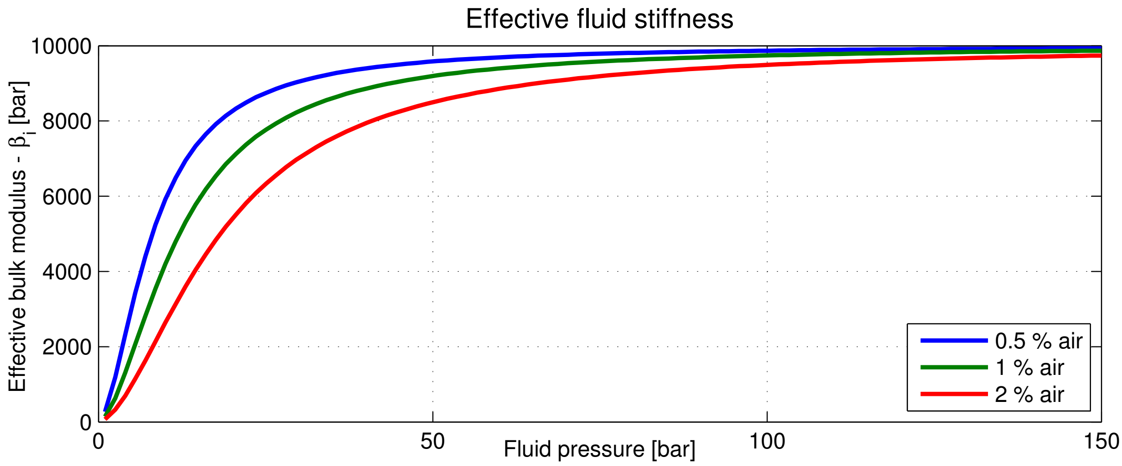

Figure 2.7. Effective bulk modulus of fluid with 0.5-2 % air content.

As a rule of thumb, the effective bulk modulus should not be set higher than 10.000 bar for modeling purposes, unless verified experimentally. (Andersen, 2003)

2.1.7 Model of Mechanical Load

In the test setup of the SvDP-concept, a backhoe loader is used as mechanical load during test. A sketch of the backhoe loader is given in figure 2.8 on the following page.

Link 4 serves as manipulator, while the remaining links are set in a fixed position. Link 4 is chosen due to its capability of serving as a pushing and pulling load, where an unknown weight can be placed in the bucket to test the control systems robustness to varying load conditions.

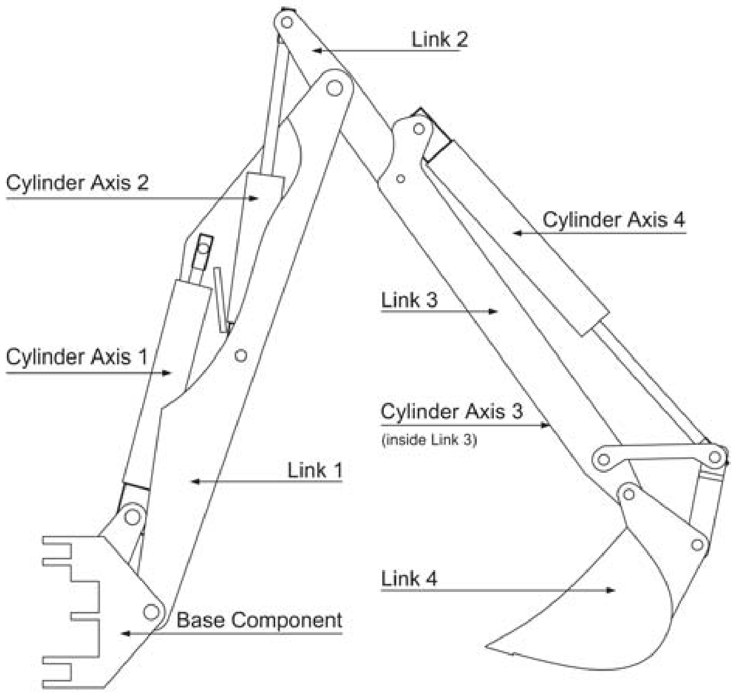

Figure 2.8. Sketch of manipulator in test setup for SvDP-concept. Illustration from (Schmidt, 2013).

The focus of this project is to control the hydraulic system, not to analyze the mechanical structure. Therefore a mechanical model, derived by Schmidt (2013), is utilized in the simulation model. The input to the model is the position of the actuator, from which the the equivalent mass is determined. The mechanical model also includes the gravitational force, however, measurements have shown slight discrepancies between the measured data and the output of the mechanical model. The gravitational load is therefore determined experimentally in section 2.2.

The Coriolis- and centripetal forces are omitted for simplification, due to their relatively low influence compared to the gravitational force and the equivalent mass (Schmidt, 2013). The inertial load is illustrated in figure 2.9 as a function of the piston position.

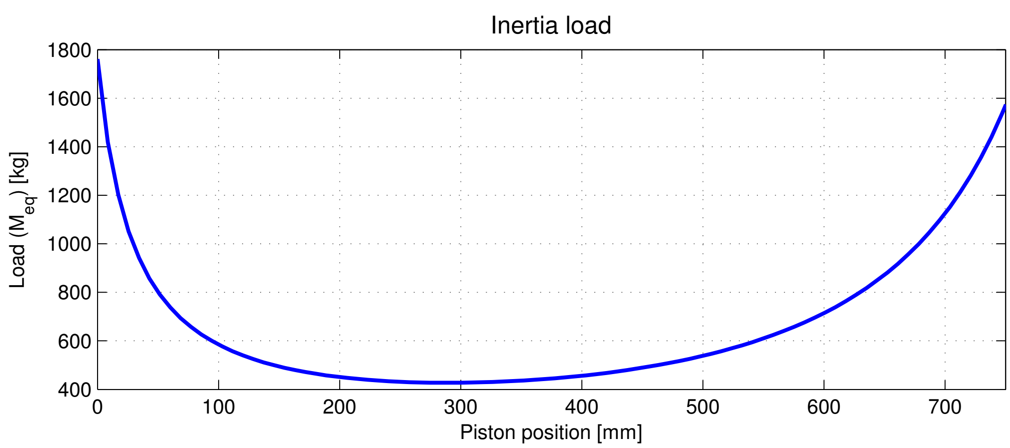

Figure 2.9. Inertial load acting on piston in Link 4. Mechanical model from Schmidt (2013).

2.2 Validation of the Simulation Model

To validate the simulation model, several tests have been carried out. The validation, presented in this section, originates from the experiments documented in Appendix B.

2.2.1 Validation of the Servo Drive

The dynamics of the servo-drive are determined by applying several small step inputs to the test setup. The test results, along with the response of the fitted transfer function, are shown in figure 2.10. The measured responses of the servo-drive are obtained by applying steps of ±100, 200 and 300 rpm to an unloaded test setup i.e the PDVs are opened. The results are normalized in order to compare them. The original measurements are shown in Appendix B.

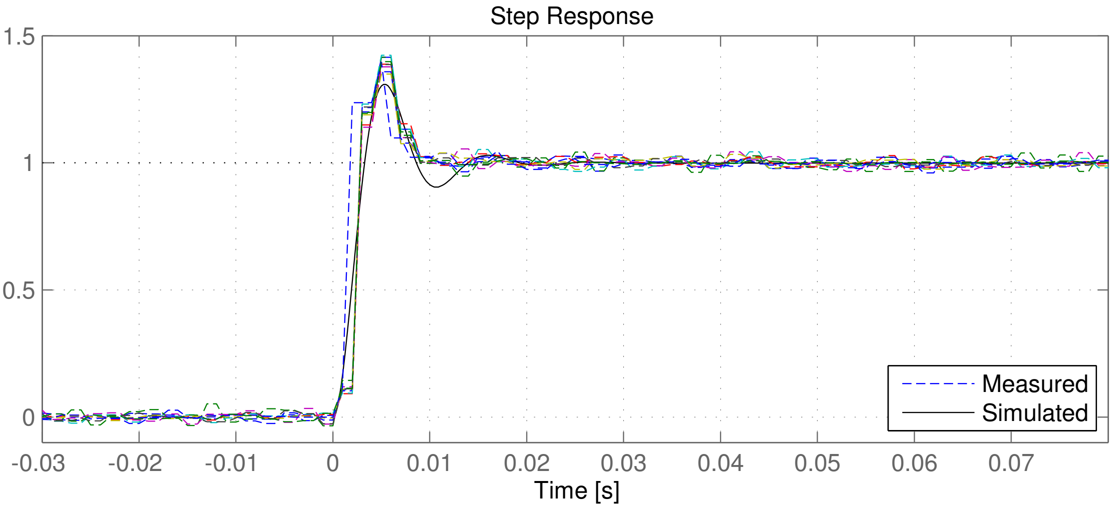

Figure 2.10. Showing the normalized measured response of the servo-drive along with the simulated response, obtained from the fitted transfer function.

The simulated response, shown in figure 2.10, is determined by applying a unit step to the second order transfer function given in equation (2.15) on page 12. The parameter values are listed in table 2.5. As seen in figure 2.10, the simulated response has a slightly larger undershoot than the measured responses, however, this is assessed as negligible, due to the relatively high bandwidth of the servo drive.

Parameter	Value
$\omega_{n,m}$	100 [Hz]
ζ_m	0.35 [-]

Table 2.5. Fitted parameters of the servo drive.

It is known that the dynamics of the servo drive changes with the load. Tests, with the cylinder loaded and with a step of 1500 rpm, shows that $\omega_{n,m}$ may be as low as 80 Hz and ζ_m up to 0.65. Despite this, it is assessed that the parameters listed in table 2.5, can be used for a general small-signal model of the servo drive. The main reason for this is that the eigenfrequency of the servo drive is approximately 5 times faster than the highest eigenfrequency of the cylinder and therefore has little influence on its dynamics. This is shown later in chapter 5, where a linear model of the system is established and analyzed.

2.2.2 Validation of the Gravitational Load

The model of the external forces is obtained by actuating the piston with a very low velocity, whereby the force balance in equation (2.1) on page 6 simplifies to equation (2.20), as described in Appendix B.3.

$$A_p \cdot p_p - A_r \cdot p_r \approx F_c + F_{ext} \tag{2.20}$$

Assuming that the external forces of the load are equal to the gravitational load, the gravitational load F_g can be approximated by a polynomial. The fitted polynomial describing the gravitational load is shown in figure 2.11.

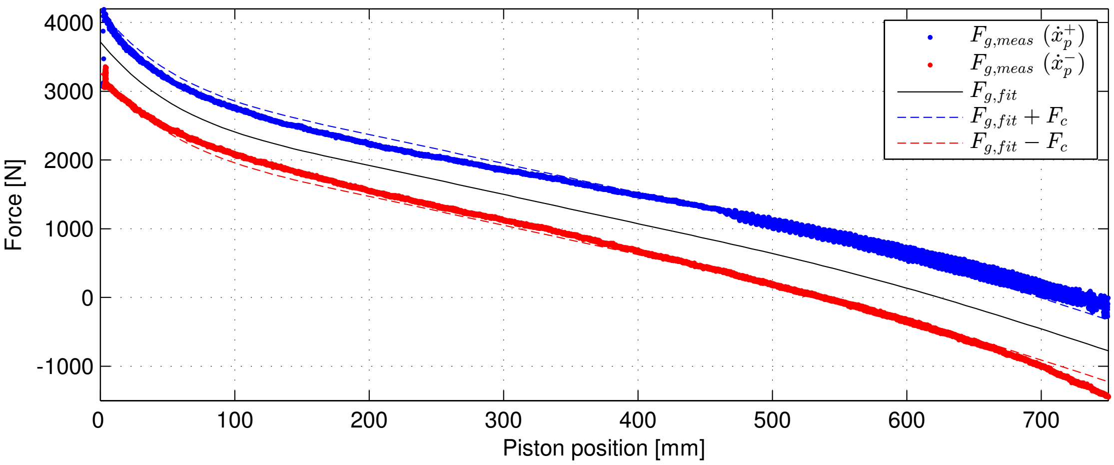

Figure 2.11. Gravitational load in both directions obtained from measurements presented in Appendix B.3, along with the fitted polynomial describing the gravitational load.

The polynomial describing the gravitational load, $F_{g,fit}$ in figure 2.11, is given by the 7th order polynomial, presented in equation (2.21).

$$\begin{aligned} F_{g,fit} = &- 5.69\text{e-}16 \cdot x_p^7 + 1.88\text{e-}12 \cdot x_p^6 - 2.54\text{e-}9 \cdot x_p^5 + 1.80\text{e-}6 \cdot x_p^4 \ \ldots \\ &- 7.22\text{e-}4 \cdot x_p^3 + 0.16 \cdot x_p^2 - 23.90 \cdot x_p + 3.72\text{e}3 \end{aligned} \tag{2.21}$$

Furthermore, the Coulomb friction is determined by half the difference between the two measured curves in figure 2.11, and is approximated to 450 N. It can be seen that the approximated Coulomb friction is slightly higher when the piston is positioned between 100-300 mm, and a little lower when the piston position is greater than 650 mm. However, for the purpose of this project, this difference is assessed as negligible.

2.2.3 Final Verification

The dynamic performance of the simulation model is assessed by applying an input, consisting of a negative speed reference followed by a positive. The verification of the model is based on two tests. In the first test, steps of ± 2250 rpm are applied. This corresponds to 75 % of the maximum speed. The second test is performed with steps of ± 1000 rpm, corresponding to 33 % of the maximum speed. The applied inputs are shown in figures B.6 and B.7 in Appendix B along with the measurements from the experiments.

In order to fit the simulation model with the measurements, the following variables are adjusted:

- Viscous friction in the piston, B_v
- Stiffness of the oil, β_F
- Air content in the fluid, ϵ_{A0}
- Rod and piston side leakage coefficient, C_{rLeak} and C_{pLeak}

These parameters are adjusted by taking both tests into consideration when fitting the model. Compromises have been made to obtain a model that captures the main dynamics of the system and is reasonable accurate at steady state.

When fitting the viscous friction coefficient, it was noticed that the coefficient is approximately 50% lower when $\dot{x}_p$ is positive compared to negative, whereby a direction dependent viscous friction coefficient is implemented. A direction dependent viscous friction coefficient can for example occur due to the sealing of the piston. The friction caused by a sealing can depend on the direction of movement, magnitude of the velocity, pressure level ect. For modeling of the SvDP-concept, it is assessed that the viscous friction coefficient can be approximated to be constant, only dependent on the direction of motion.

In addition, the fitting revealed that the piston side leakage coefficient is larger than the rod side leakage coefficient. This is likely due to a greater leakage across the piston side pump, which is larger than the rod side pump. The greater leakage may also originate from a difference in the two PDV, as these are not leakage proof.

The results of the final verification, with a step of ± 2250 rpm, are shown in figure 2.12 on the following page. The results obtained with a step of ± 1000 rpm, are shown in figure 2.13. The individual results on the force balance and pressure levels are discussed hereafter.

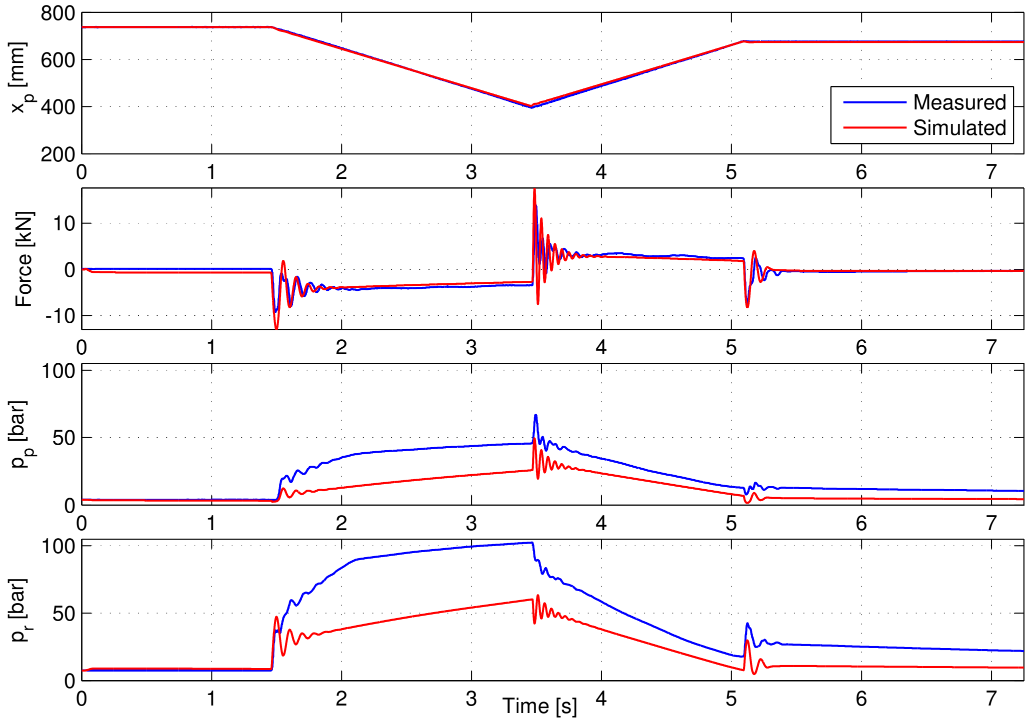

Figure 2.12. Measurements of the validation test along with the simulated result. A step of -2250 rpm is given as input at the time 1.5 s. At the time 3.45 s, the input is changed to +2250 rpm. The force is calculated from the measured pressure levels.

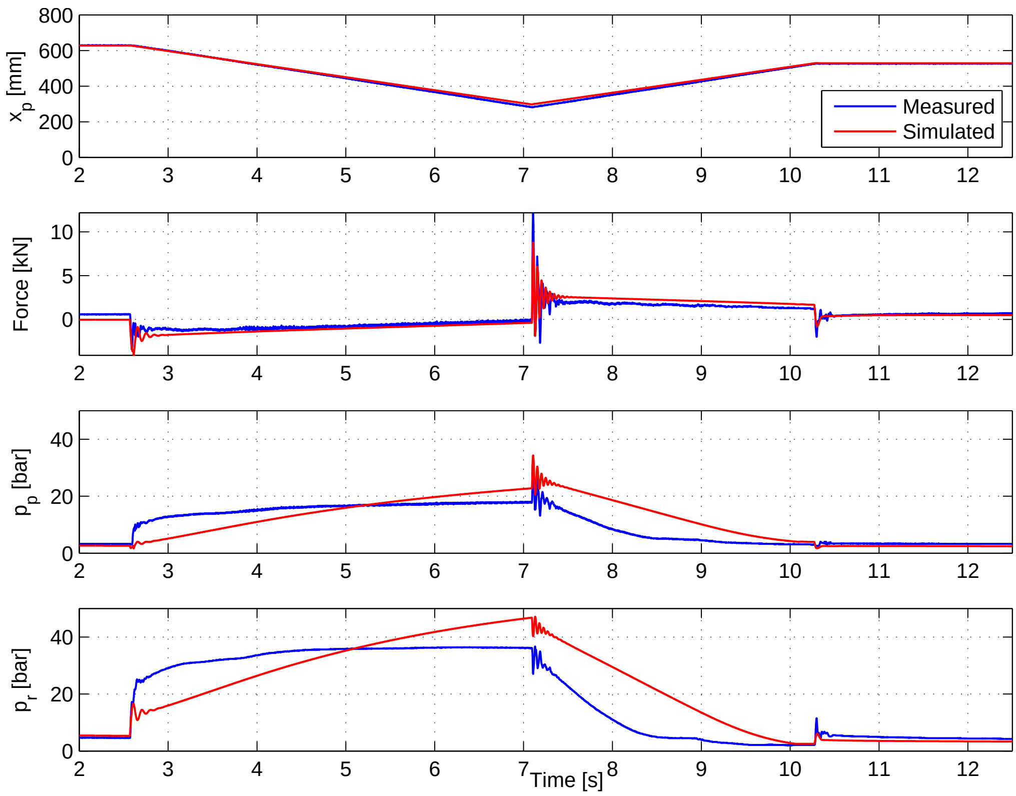

Figure 2.13. Measurements of the validation test along with the simulated result. A step of -1000 rpm is given as input at the time 2.5 s. At the time 7.1 s, the input is changed to +1000 rpm. The force is calculated from the measured pressure levels.

It is observed from the figures 2.12 and 2.13, that the absolute pressure levels in the two chambers are not captured very well by the model. During adjustments of the model, it was found that the pressure levels are highly dependent on the flow balance between the two pumps. The deviation is therefore expected to originate from uncertainties in the volumetric efficiencies. The consequence of adjusting these is illustrated in figure 2.14, which shows the same simulation as in figure 2.12, where the volumetric efficiencies have been altered ±2 % i.e. ±2 % have been added to the volumetric efficiencies (never exceeding 100 %). The adjustments are performed to illustrate the sensitivity in pressure levels with respect to the flow imbalance (thereby the volumetric efficiency of the pumps).

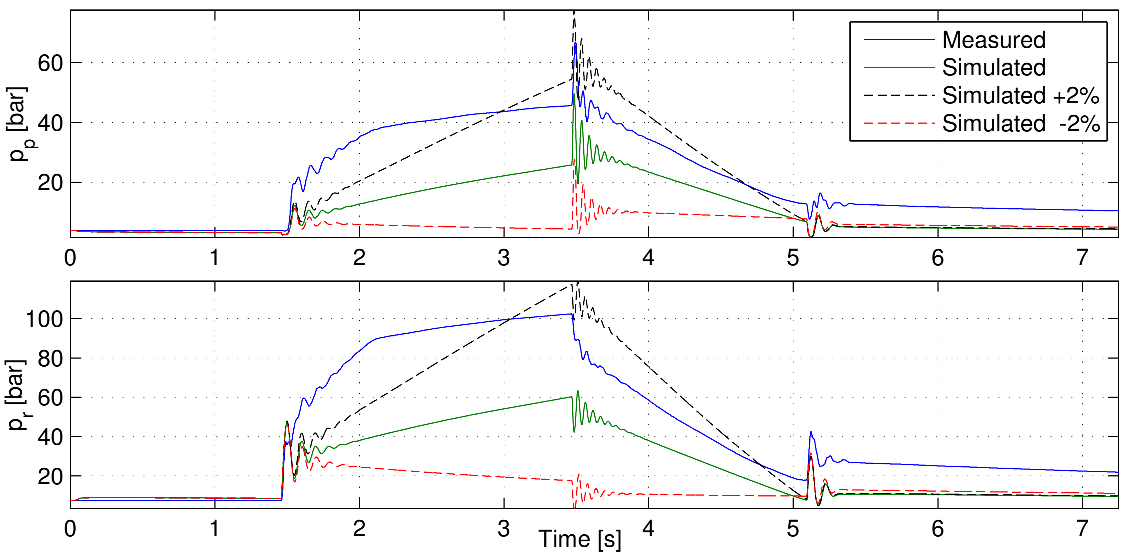

Figure 2.14. The dashed lines show the results of the simulation when the pump efficiencies have been altered ±2%. The solid lines illustrate the original simulation results and measurements.

As seen in figure 2.14, the absolute pressure changes approximately ±50 % when the volumetric efficiencies are altered 2 %. Furthermore, figure 2.14 shows that it is not possible to obtain the measured pressure response by solely adjusting the modeled volumetric efficiencies of the two pumps. To identify the cause of deviation, an extensive analysis is required, which is not within the scope of this project. Therefore, a greater emphasis is placed on the dynamics of the pressure, rather than the absolute values of the pressure. The pressure dynamics are easier assessed by looking at the resulting force from the two pressure levels. This was shown in the second graph of figure 2.12 and 2.13. A section of the force balance in figure 2.12 is shown in figure 2.15 on the next page, for clarity.

Figure 2.15 shows that the frequency of the pressure oscillations is fairly well replicated, except for some nonlinearities, occurring at approximately 1.55 seconds and 3.6 seconds, which have not been modeled. This could be nonlinearities of the friction in the system, as a fairly simple friction model is utilized.

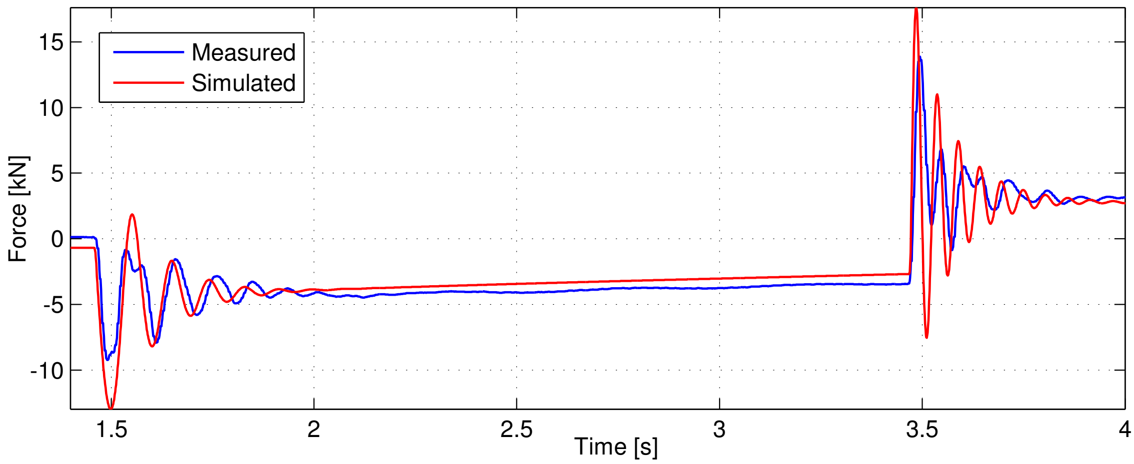

Figure 2.15. A zoom of the force acting on the piston, presented in figure 2.12.

The dynamics of the system are fairly well captured, despite the differences described above. The damping of the modeled system, seems slightly higher in the simulation than the measurement, however, it is assessed that the simulation model reflects the main dynamics of the system, and the model is regarded to be sufficiently accurate for the purpose of this project.

2.3 Summary of the Nonlinear Model

A nonlinear simulation model, describing the SvDP-concept connected to a backhoe loader, is established and validated by experiments in this chapter.

The SvDP-concept is described by Newtons 2nd law, applied to the cylinder, and two continuity equations, describing the chamber pressures. A mechanical model of the backhoe loader, developed by Schmidt (2013), was utilized to describe the equivalent inertia load acting on the piston. The characteristics of the individual hydraulic components are examined and implemented in the simulation model. Hereafter, experiments are utilized to establish a model of the gravitational load, acting on the piston, and to determine the dynamics of the servo drive.

Finally, a validation of the simulation model is performed. The viscous friction coefficient is found as direction dependent and the fluid properties are adjusted to match the fluid stiffness in the experiments. In the validation process it is found difficult to match the simulated pressure levels with those obtained in the experiments. It is found that the difference occurs due to unmodeled effects in the pumps, as the flow balance between the pumps highly influences the pressure gradients. Despite these differences, it is concluded that the nonlinear simulation model provides a sufficiently accurate representation of the physical setup.

Steady State Analysis of the SvDP-concept 3

In this chapter, the system is analyzed in order to examine the problems which may be encountered during operation. The system analysis is performed assuming a steady state piston velocity. Initially, in section 3.1, the system is simplified and analyzed to gain insight in the properties of the SvDP-concept. Later, in section 3.2, it is shown that the results, obtained from the simple analysis, apply for the complete system where leakage is taken into consideration. Based on the results, it is analyzed when and how the pressures can be regulated.

3.1 Simplified Steady State Analysis

Utilizing the simplified system, illustrated in figure 3.1, it is examined which problems may be encountered during operation.

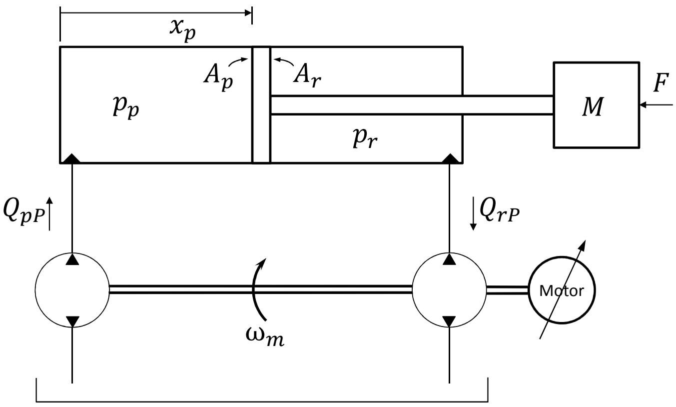

Figure 3.1. Simplified schematic of the hydraulic system.

As seen in figure 3.1, all the valves of the system have been disregarded, along with the leakage flow. To study the impact of the ratio between the piston areas and the pump displacements, the area ratio α, and displacement ratio δ, are defined by equation (3.1) and (3.2), respectively.

$$\alpha = \frac{A_r}{A_p} \tag{3.1}$$

$$\delta = \frac{D_r \cdot \eta_{rv}}{D_p \cdot \eta_{pv}} \tag{3.2}$$

where:

α	Piston area ratio	[-]
A_p	Area of the piston side in the cylinder	$\left[\mathrm{m}^2\right]$
A_r	Area of the rod side in the cylinder	$\left[\mathrm{m}^2\right]$
δ	Pump displacement ratio	[-]
D_p	Displacement of the piston side pump	$\left[\frac{\mathrm{m}^3}{\mathrm{rev}}\right]$
D_r	Displacement of the rod side pump	$\left[\frac{\mathrm{m}^3}{\mathrm{rev}}\right]$
η_{iv}	Volumetric efficiency of the pump	[-]

The area ratio is constant and the magnitude of the parameters are listed in Appendix A. By including the volumetric efficiencies of the two pumps in the displacement ratio δ can vary, such that it can be both larger than α and smaller than α. Therefore the system must be analyzed in both cases.

The system should be able to operate regardless of the applied load. It is therefore decided to analyze the system with two different load types; pushing load and pulling load. A purely inertial load only occurs in one piston position and is therefore not of interest. Finally, the system is analyzed utilizing both a positive and a negative rotational direction of the motor, yielding a total of 8 different scenarios to be analyzed.

To examine the pressure change in the two control volumes, a simplified continuity equation for each chamber is established. Leakage flow is neglected and bulk modulus is assumed constant.

Analysis assuming constant pressure in the piston side chamber

The rod side continuity equation is given by equation (3.3).

$$
\begin{gathered}
-Q_{rP} = \dot{V}_r + \dot{p}_r \cdot \frac{V_r}{\beta_r} \\
\Updownarrow \\
-D_r \cdot \eta_{rv} \cdot \omega_m = -\dot{x}_p \cdot A_r + \dot{p}_r \cdot \frac{V_r}{\beta_r}
\end{gathered}
\tag{3.3}
$$

where:

β	Stiffness of the oil (bulk modulus)	[Pa]
$\dot{p}_r$	Pressure gradient in the rod side chamber	$\left[\frac{\mathrm{Pa}}{\mathrm{s}}\right]$
Q_{rP}	Rod side pump flow	$\left[\frac{\mathrm{m}^3}{\mathrm{s}}\right]$
$\dot{V}_r$	Volume gradient of the rod side chamber in the cylinder	$\left[\frac{\mathrm{m}^3}{\mathrm{s}}\right]$
V_r	Volume of the rod side chamber	$\left[\mathrm{m}^3\right]$
ω_m	Rotational speed of the shaft connected to the pump	$\left[\frac{\mathrm{rev}}{\mathrm{s}}\right]$
$\dot{x}_p$	Piston velocity	$\left[\frac{\mathrm{m}}{\mathrm{s}}\right]$

Assuming that the pressure in the piston side chamber is constant, the flow into the control volume is equal to the chamber expansion. This assumption is performed to simplify the analysis to gain insight in the properties of the SvDP-concept. Later, in section 3.2, it is shown that the results obtained here, also apply for the general case. Utilizing the assumption of constant pressure in the piston side chamber, $\dot{x}_p$ can be expressed by equation (3.4).

$$\begin{aligned} Q_{pP} &= \dot{x}_p \cdot A_p + \cancel{\dot{p}_p \cdot \frac{V_p}{\beta_p}} \\ &\Updownarrow \\ \dot{x}_p &= \frac{D_p \cdot \eta_{pv} \cdot \omega_m}{A_p} \end{aligned} \tag{3.4}$$

Inserting this into equation (3.3), yields:

$$\begin{aligned} -D_r \cdot \eta_{rv} \cdot \omega_m &= -\frac{D_p \cdot \eta_{pv} \cdot \omega_m}{A_p} \cdot A_r + \dot{p}_r \cdot \frac{V_r}{\beta_r} \\ &\Updownarrow \\ \dot{p}_r &= \frac{\beta_r}{V_r} \cdot \omega_m \cdot (D_p \cdot \eta_{pv} \cdot \alpha - D_r \cdot \eta_{rv}) \end{aligned} \tag{3.5}$$

Utilizing the displacement ratio given by equation (3.2), equation (3.5) simplifies to:

$$\dot{p}_r = \frac{\beta_r}{V_r} \cdot \omega_m \cdot D_p \cdot \eta_{pv} \cdot (\alpha - \delta) \tag{3.6}$$

From equation (3.6), it can be seen that the sign of the pressure gradient in the rod side chamber $\dot{p}_r$ is a function of the rotational direction of the motor ω_m and the difference between α and δ, and is given by equation (3.7).

$$\text{sign}(\dot{p}_r) = \text{sign}(\omega_m) \cdot \text{sign}(\alpha - \delta) \tag{3.7}$$

Analysis assuming constant pressure in the rod side chamber

Similarly, the pressure change in the piston side chamber is determined by utilizing the continuity equation for this chamber. This is done in equation (3.8).

$$\begin{aligned} Q_{pP} &= \dot{V}_p + \dot{p}_p \cdot \frac{V_p}{\beta_p} \\ &\Updownarrow \\ D_p \cdot \eta_{pv} \cdot \omega_m &= \dot{x}_p \cdot A_p + \dot{p}_p \cdot \frac{V_p}{\beta_p} \end{aligned} \tag{3.8}$$

where:

$\dot{p}_p$	Pressure gradient in the piston side chamber	$\left[\frac{\text{Pa}}{\text{s}}\right]$
Q_{pP}	Piston side pump flow	$\left[\frac{\text{m}^3}{\text{s}}\right]$
$\dot{V}_p$	Volume gradient of the piston side chamber in the cylinder	$\left[\frac{\text{m}^3}{\text{s}}\right]$
V_p	Volume of the piston side chamber	$\left[\text{m}^3\right]$

Again, by assuming the pressure in the other chamber is constant, $\dot{x}_p$ is determined by:

$$\begin{aligned} -Q_{rP} &= -\dot{x}_p \cdot A_r \\ &\Updownarrow \\ \dot{x}_p &= \frac{D_r \cdot \eta_{rv} \cdot \omega_m}{A_r} \end{aligned} \tag{3.9}$$

Inserting this into equation (3.8), yields:

$$
\begin{aligned}
D_p \cdot \eta_{pv} \cdot \omega_m &= \frac{D_r \cdot \eta_{rv} \cdot \omega_m}{A_r} \cdot A_p + \dot{p}_p \cdot \frac{V_p}{\beta_p} \\
&\Updownarrow \\
\dot{p}_p &= \frac{\beta_p}{V_p} \cdot \omega_m \cdot \left(D_p \cdot \eta_{pv} - \frac{D_r \cdot \eta_{rv}}{\alpha} \right) \\
&\Updownarrow \\
\dot{p}_p &= \frac{\beta_p}{V_p} \cdot \omega_m \cdot D_r \cdot \left(\frac{1}{\delta} - \frac{1}{\alpha} \right)
\end{aligned} \tag{3.10}
$$

Equation (3.10) shows that the pressure change in the piston side chamber also depends on the rotational direction of the motor along with the difference between α and δ, and is given by equation (3.12). For simplicity, the sign of this term is rewritten using equation (3.11). The relationship presented in equation (3.11) is only valid because α and δ are always positive.

$$\text{sign}\left(\frac{1}{\delta} - \frac{1}{\alpha} \right) = \text{sign}(\alpha - \delta) \tag{3.11}$$

$$\Downarrow$$

$$\text{sign}(\dot{p}_p) = \text{sign}(\omega_m) \cdot \text{sign}(\alpha - \delta) \tag{3.12}$$

It is seen that the sign of the pressure gradient in the piston side chamber $\dot{p}_p$ is described in the same manner as the sign of the pressure gradient in the rod side chamber, given in equation (3.7). To determine the pressure difference between the two chambers, the force equilibrium on the cylinder, depending on the load is examined. As mentioned earlier, two loads are examined; pushing and pulling load.

Consequences of a Pushing Load

The relationship between the pressures in the two chambers, when the load pushes on the cylinder, is determined by examining the forces acting on the cylinder. An illustration of the cylinder with a pushing load is given in figure 3.2.

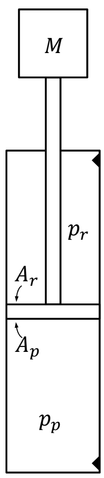

Figure 3.2. Illustration of the cylinder with a pushing load.

The steady state force equilibrium on the cylinder with a pushing load is given by equation (3.13). The external force F is a summation of the gravitational force, the viscous- and Coulomb frictions.

$$F = p_p \cdot A_p - p_r \cdot A_r = A_p \cdot (p_p - \alpha \cdot p_r) \tag{3.13}$$

Equation (3.13) shows that $p_p > \alpha \cdot p_r$, when the external force is positive. Remember that $\alpha < 1$, so the equation does not state the absolute magnitude of the rod side pressure. Combining this result with equation (3.7) and (3.12), the pressure development of the two chambers can be determined for the cases where $\delta > \alpha$ and $\delta < \alpha$, along with both the positive and negative rotational direction of the motor ω_m^+ and ω_m^-, respectively. Note that $\dot{p}^+$ and $\dot{p}^-$ denote a positive and negative pressure gradient, respectively.

- $\alpha > \delta$
  - $\omega_m^+ \rightarrow \dot{p}_p^+$ & $\dot{p}_r^+ \rightarrow$ overpressure may occur in both chambers.
  - $\omega_m^- \rightarrow \dot{p}_p^-$ & $\dot{p}_r^- \rightarrow$ cavitation may occur in both chambers, depending on the magnitude of the load, as $p_p > \alpha \cdot p_r$.
- $\delta > \alpha$
  - $\omega_m^+ \rightarrow \dot{p}_p^-$ & $\dot{p}_r^- \rightarrow$ cavitation may occur in both chambers, depending on the magnitude of the load, as $p_p > \alpha \cdot p_r$.
  - $\omega_m^- \rightarrow \dot{p}_p^+$ & $\dot{p}_r^+ \rightarrow$ overpressure may occur in both chambers.

Consequences of a Pulling Load

Similarly to the above, the forces acting on the cylinder with a pulling load are determined using figure 3.3.

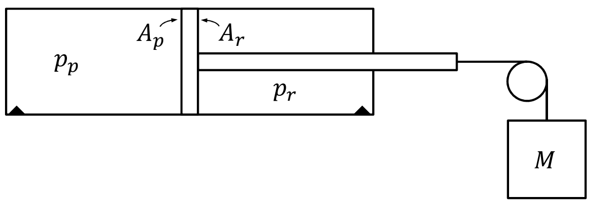

Figure 3.3. Illustration of the cylinder with a pulling load.

The steady state force equilibrium on the cylinder with a pulling load is given by equation (3.14). Again, the external force F is a summation of the gravitational force, the viscous- and Coulomb frictions acting on the piston.

$$F = p_r \cdot A_r - p_p \cdot A_p = -A_p \cdot (p_p - \alpha \cdot p_r) \tag{3.14}$$

Equation (3.14) yields that $p_p < \alpha \cdot p_r$, as F is positive given a pulling load. Applying this along with equations (3.7) and (3.12) for the four cases, yields:

- $\alpha > \delta$
  - $\omega_m^+ \rightarrow \dot{p}_p^+ \;\; \& \;\; \dot{p}_r^+ \rightarrow$ overpressure may occur in both chambers.
  - $\omega_m^- \rightarrow \dot{p}_p^- \;\; \& \;\; \dot{p}_r^- \rightarrow$ cavitation may occur in the piston side chamber, as $p_p < \alpha \cdot p_r$.
- $\delta > \alpha$
  - $\omega_m^+ \rightarrow \dot{p}_p^- \;\; \& \;\; \dot{p}_r^- \rightarrow$ cavitation may occur in the piston side chamber, as $p_p < \alpha \cdot p_r$.
  - $\omega_m^- \rightarrow \dot{p}_p^+ \;\; \& \;\; \dot{p}_r^+ \rightarrow$ overpressure may occur in both chambers.

These results are similar to those obtained with a pulling load. It is thereby shown that the direction of the load only determines which chamber pressure that reaches the lower pressure limit set by the anti-cavitation system.

3.2 Considerations on Control Strategy

The results obtained during initial analysis of the system, where only the pump flows are considered, are generalized in this section such that a control scheme for the pressures can be established.

The general continuity equation for the piston side chamber is given in equation (3.15), where $\sum Q_p$ denotes the flow rate entering the control volume. This is the sum of pump-, leakage- and valve flows. The piston velocity is isolated in equation (3.16).

$$\sum Q_p = A_p \cdot \dot{x} + \frac{V_p}{\beta_p} \cdot \dot{p}_p \tag{3.15}$$

$$\Updownarrow$$

$$A_p \cdot \dot{x} = \sum Q_p - \frac{V_p}{\beta_p} \cdot \dot{p}_p \tag{3.16}$$

The continuity equation for the rod side chamber is given in equation (3.17), where $\sum Q_r$ denotes the flow rate leaving the control volume. Substituting the piston velocity, from equation (3.16), yields equation (3.18).

$$-\sum Q_r = -\alpha \cdot A_p \cdot \dot{x} + \frac{V_r}{\beta_r} \cdot \dot{p}_r \tag{3.17}$$

$$\Downarrow$$

$$-\sum Q_r = -\alpha \cdot \sum Q_p + \alpha \cdot \frac{V_p}{\beta_p} \cdot \dot{p}_p + \frac{V_r}{\beta_r} \cdot \dot{p}_r \tag{3.18}$$

$$\Updownarrow$$

$$\sum Q_p - \frac{\sum Q_r}{\alpha} = \frac{V_p}{\beta_p} \cdot \dot{p}_p + \frac{V_r}{\beta_r} \cdot \frac{\dot{p}_r}{\alpha} \tag{3.19}$$

The flow balance is isolated in equation (3.19). If $\sum Q_p < \frac{\sum Q_r}{\alpha}$ the weighted sum of the pressure gradients must be negative, when the flow rates are positive. With negative flow rates, the weighted sum of the pressure gradients must be positive. This means:

- If the sum of the flows in the system is positive $\Rightarrow$ the total pressure in the system increase.

- If the sum of the flows in the system is negative $\Rightarrow$ the total pressure in the system decrease.

It can not be shown from equation (3.19) which pressure gradient, in the control volumes, is largest, nor if they have equal signs when the piston velocity is in steady state. Only that the total pressure in the system decreases if the sum of the flows is negative. Despite this, the result is similar to the initial analysis, except that this general result is independent of the load situation. The load only determines which chamber pressure is greater or will reach the cavitation pressure.

The properties found in the analysis of the system are illustrated in a scheme in figure 3.4. The conclusions are marked in the red boxes. When the sum of the pressure gradients are negative, the pressure levels go towards zero. This situation is maked "cavitation", meaning that the pressure level is limited by the anti-cavitation system. When positive, the total pressure level increases and will eventually need to be controlled. As it can not be determined which pressure gradient is largest, further analysis is needed to determine how the pressure levels can be reduced.

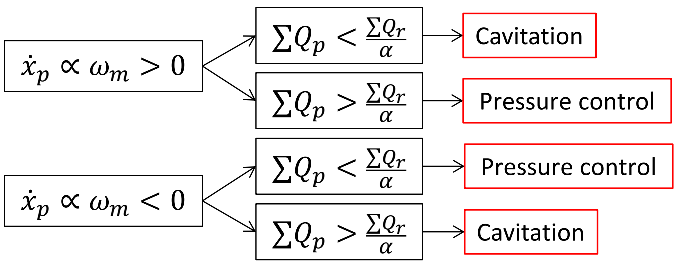

Figure 3.4. Consequences of imbalance between flow rates and the area ratio of the piston. Note the constraint sign (ω_m)=sign $(\sum Q_p)$=sign $(\sum Q_r/\alpha)$.

Due to the configuration of the system, it is not possible, using the PDVs, to increase the pressure levels above tank pressure, as the PDVs are connected to the tank. Thereby the PDVs can only be utilized to reduce the line pressures.

3.2.1 Determination of Pressure Control Strategy

The following analysis and decisions, regarding the control strategy, are made based on the arguments listed below:

1. The piston velocity is regulated by controlling the rotational speed of the pump shaft. The obtainable performance, of this control loop, depends on the hydro-mechanical eigenfrequency. It is known that the hydro-mechanical eigenfrequency depends on the pressure levels, as the fluid stiffness directly influences the stiffness of the controlled system. At low pressure the fluid stiffness is low and a function of

the pressure level (see figure 2.7 on page 15, showing bulk modulus vs. pressure), whilst it is almost constant at a maximum when the pressure level is above 25 bar.

2. If the objective is to minimize the energy consumption of the operating system, it is desirable that the pressure levels are low. Excessive pressure in the control volumes can be reduced, normally through valves/orifices, resulting in heat generation and thereby energy loses. Furthermore, the leakage flows increase with the pressure levels, resulting in increasing pump flows to accommodate the velocity commands.

3. Regulation of the pressure in any chamber, affects the pressure level in both chambers. Independent of the chamber at which pressure control is performed, the pressure levels decrease on both sides of the piston.

4. As a compromise between these objectives, it is decided to regulate the pressures such that the lowest pressure is maintained at 25 bar to ensure high fluid stiffness. The other pressure level (higher pressure), is allowed to vary in accordance with the load acting on the piston.

When an imbalance in the flow rates causes pressure build-up, the absolute pressure levels depend on the magnitude of the flow imbalance and the external load. From the prior analysis, it can not be determined what the pressure levels will be at a given time. The piston velocity is considered constant, but the pressure gradients change in time and their magnitude is determined by the imbalance between the flow rates and the area ratio. Despite this, the pressure difference between the two chambers, can be determined from the external load and the friction acting on the piston. At a steady state piston velocity, the force balance is given by equation (3.20). An analysis of the force balance reveals which pressure level is lowest and thereby which pressure that should be controlled.

$$F_g + B_v \cdot \dot{x}_p + F_c = A_p \cdot (p_p - \alpha \cdot p_r) \tag{3.20}$$

From equation (3.20) the following correlations are know:

- Pushing load: $(F_g + B_v \cdot \dot{x}_p + F_c) > 0 \Rightarrow p_p > \alpha \cdot p_r$
- Pulling load: $(F_g + B_v \cdot \dot{x}_p + F_c) < 0 \Rightarrow p_p < \alpha \cdot p_r$. With $\alpha < 1 \Rightarrow p_p < p_r$

The magnitude of the gravitational load F_g depends on the piston position, while the viscous friction coefficient B_v depends on the direction of movement. This is shown in section 2.2, where the model is validated. The maximum pressure difference occurs (in this system) when the combined load reaches a maximum. This happens at maximum positive piston velocity $\dot{x}_p$ = 225 mm/s and at the piston position x_p = 0 mm. Under these conditions, the combined load is pushing the piston with 6.4 kN, resulting in the pressure difference $p_p - \alpha \cdot p_r \approx 10.5$ bar. In the following steady state analysis, it is the absolute pressure, in the two chambers, that is of interest to determine the lowest pressure.

Figure 3.5 summarizes the results of the pressure analysis. The figure illustrates the load acting on the piston versus the piston side pressure. The blue line is obtained by calculating the load when the two chamber pressures are equal in magnitude. The shaded area under this line indicates the range where the piston side pressure is always lower than the rod side pressure in steady state. Above the line, the rod side pressure is always the lowest steady state pressure. The maximum pushing load is marked with a black line. It is desired to control the lowest pressure level, only when it is higher than 25 bar.

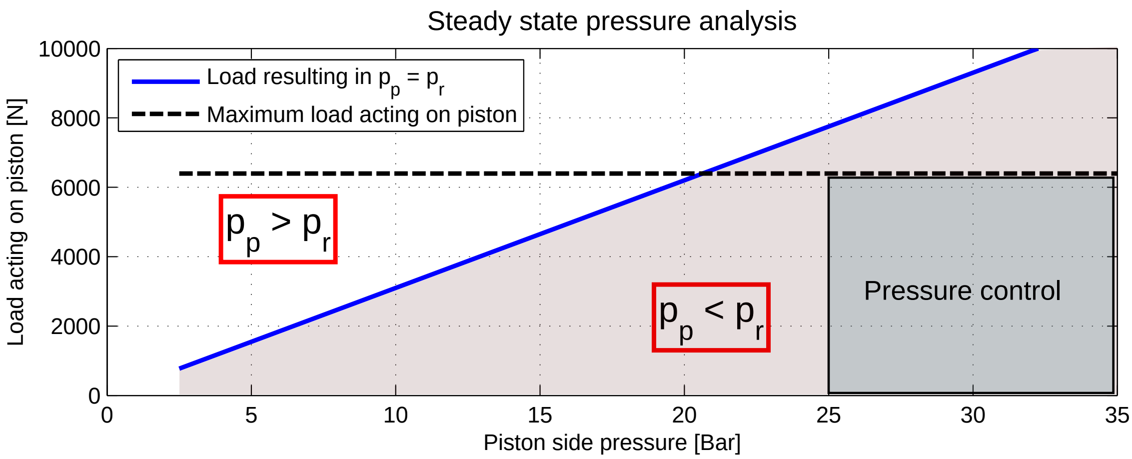

Figure 3.5. Steady state analysis of the pressure levels as a function of the load acting on the piston. The blue line outlines the load resulting in equal chamber pressures. The black line indicates the maximum load obtainable at steady piston velocity for this system.

To clarify figure 3.5, two examples are given:

- If the load, acting on the piston, is equal to the maximum pushing load 6.4 kN, then the pressure difference $p_p - \alpha \cdot p_r \approx 10.5$ bar. If the steady state piston side pressure is 15 bar, then the rod side pressure is 9 bar as the area ratio $\alpha \approx 0.5$ i.e. $p_p > p_r$.

- Using the same load, but with the piston side pressure equal to 30 bar, then the rod side pressure is equal to 39 bar i.e. $p_p < p_r$.

In figure 3.5 it can be seen that whenever $p_p > 21$ bar, it is ensured that $p_p < p_r$ is always satisfied in this system where the maximum steady state load is 6.4 kN.

Whenever it is possible to control the pressure level, it is desired to control the minimum pressure to 25 bar. The criteria ensuring $p_p < p_r$ when the maximum pushing load is acting on the piston, is that $p_p > 21$ bar. When the load is pulling it is always ensured that $p_p < p_r$. This leads to the conclusion, that it is always the piston side pressure that has to be controlled.

In figure 3.4 on page 29, it was shown that the need for pressure control, in this system, depends on the imbalance between the flow rates and the area ratio of the piston. Knowing that p_p is always lower than p_r, when pressure control is needed, the flow balance is reconsidered to determine when pressure control is required. It is shown in the following that pressure control is only needed in this system when the shaft velocity is negative:

- **Case:** $\omega_m > 0$
  When $\omega_m > 0$, it is necessary that $\sum Q_p > \frac{\sum Q_r}{\alpha}$ in order for pressure control to be required, as a positive sum of the weighted pressure gradients increases the pressure level of the system. This was shown in figure 3.4 on page 29. Writing out the flows, reveals the necessary difference in pump efficiencies to fulfill this condition. This is shown in equation (3.21). Opening the PDV will only decrease the flow rate at the piston side. It is therefore considered closed, which reduces the condition to equation (3.22).

$$\sum Q_p > \frac{\sum Q_r}{\alpha}$$
$$\Updownarrow$$
$$D_p \cdot \eta_{pv} \cdot \omega_m - C_{pleak} \cdot p_p - Q_{pV} > \frac{D_r \cdot \eta_{rv} \cdot \omega_m + C_{rleak} \cdot p_r}{\alpha} \tag{3.21}$$
$$\Downarrow$$
$$D_p \cdot \eta_{pv} \cdot \omega_m - C_{pleak} \cdot p_p > \frac{D_r \cdot \eta_{rv} \cdot \omega_m + C_{rleak} \cdot p_r}{\alpha} \tag{3.22}$$

  Equation (3.22) can be rewritten to equation (3.23), where the pump flows are collected at the left hand side.

$$\underbrace{\left(D_p \cdot \eta_{pv} - \frac{D_r \cdot \eta_{rv}}{\alpha}\right)}_{>0 \text{ is necessary}} \cdot \underbrace{\omega_m}_{\text{positive}} > \underbrace{\frac{C_{rleak}}{\alpha} \cdot p_r + C_{pleak} \cdot p_p}_{\text{positive}} \tag{3.23}$$

  All terms at the right hand side of equation (3.23) are positive. Considering the case where $\omega_m > 0$, it is a necessary, but not a sufficient condition that $\left(D_p \cdot \eta_{pv} - \frac{D_r \cdot \eta_{rv}}{\alpha}\right) > 0$ in order for $\sum Q_p > \frac{\sum Q_r}{\alpha}$ to be true. This necessary condition is rewritten into equation (3.24), where known and fixed parameters are collected at the right hand side.

$$\frac{\eta_{pv}}{\eta_{rv}} > \underbrace{\frac{D_r}{D_p \cdot \alpha}}_{\approx 1.05} \tag{3.24}$$

  As shown previously, $p_p = 25$ bar whenever the pressure level is required to be controlled. Using the steady state force balance, the rod side pressure is calculated at different velocities. The rod side pressure level also depends on the piston position, due to varying load, which results in the pressure ranges listed in the intervals below. The volumetric efficiencies are functions of the differential pressures and the shaft revolution of the pumps as shown in figure 2.5 on page 14.

  - 250 rpm$\Rightarrow \begin{cases} p_p = 25 \text{ bar} & \Rightarrow \eta_{pv} = 76.2 \ \% \\ p_r = [35.8, 50.3] \text{ bar} & \Rightarrow \eta_{rv} = [84.8, 88.8] \ \% \end{cases}$

$$\circ\ 1000\ \text{rpm} \Rightarrow \begin{cases} p_p = 25 \text{ bar} & \Rightarrow \eta_{pv} = 95.0\ \% \\ p_r = [33.4, 47.9] \text{ bar} & \Rightarrow \eta_{rv} = [94.0, 94.9]\ \% \end{cases}$$

$$\circ\ 3000\ \text{rpm} \Rightarrow \begin{cases} p_p = 25 \text{ bar} & \Rightarrow \eta_{pv} = 97.2\ \% \\ p_r = [27.0, 41.5] \text{ bar} & \Rightarrow \eta_{rv} = [95.8, 96.1]\ \% \end{cases}$$

The ratios between the volumetric efficiencies are plotted in figure 3.6, which shows that the necessary condition is never fulfilled when the shaft revolution is positive and the piston side pressure should be controlled i.e. $p_p = 25$ bar.

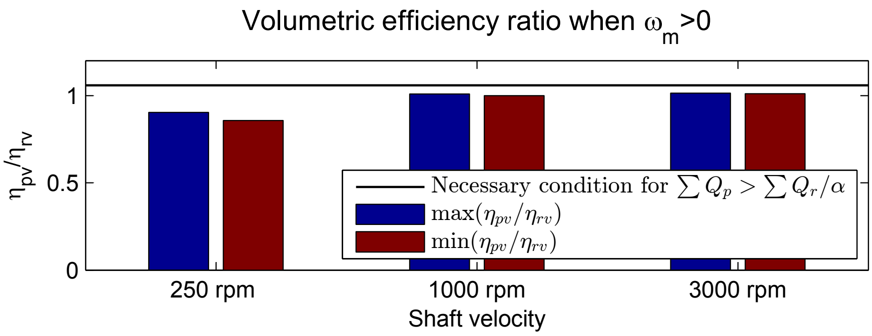

Figure 3.6. Ratio between the volumetric efficiencies when $p_p = 25$ bar, p_r determined by load and shaft velocity equal to 250, 1000 and 3000 rpm. The necessary condition for the pressure level to increase is that the ratio is at least 1.05. This is never the case and the pressure level will therefore always decrease when $\omega_m > 0$.

As the necessary condition is never fulfilled, the pressure level will always decrease when $\omega_m > 0$ and the pressure level is not controllable in this case. Using the simulation model, it is shown in figure 3.7 that the pressure levels indeed decrease when the shaft revolution is positive. The same result is seen in the experiments used for validation of the model.

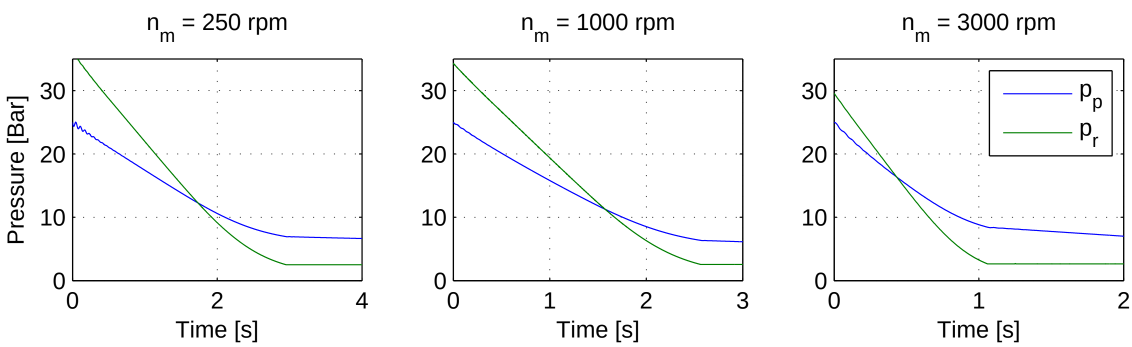

Figure 3.7. Simulations showing that the pressure levels decrease when $\omega_m > 0$. Utilizing the initial piston position $x_p = 0$ mm, and the initial piston velocity $\dot{x}_p = Q_{pP}/A_p$ in all cases.

The validity of the assumptions, made throughout this case study, is discussed to clarify the uncertainty of the result, showing that pressure control is never needed when the shaft revolution is positive:

1. Steady state volumetric efficiencies of the pumps are utilized in the analysis. During validation, in section 2.2, it is observed that not all effects are captured when modeling the pumps. Inaccuracies in the transient pump flow, lead to greater flow imbalance between the two chambers in this period, which result in higher pressure gradients than modeled. The controllers designed after the problem statement in chapter 6, are evaluated using the trajectories presented in chapter 4. Assuming that the controlled system results in smooth behavior of the velocity and the pressure, periods with rapid changes in pump velocity are short compared to the steady state period. It is therefore assessed reasonable to utilize steady state volumetric efficiencies of the pumps for making the conclusions presented in this chapter.

2. From equation (3.23), a necessary condition for an increasing pressure level in the system, was established. With the pump displacements and the area ratio of the piston considered constant, the necessary condition stated that the ratio $\eta_{pv}/\eta_{rv} > 1.05$ in order for the pressure level in the system to increase. Using coherent steady state pressures and pump speed throughout the stroke of the piston, the highest ratio was found at 3000 rpm where $\eta_{pv}/\eta_{rv} = 1.01$. This leaves a minimum margin for uncertainties in the ratio between the pump efficiencies of approximately 4 %. The margin depends on the operation point e.g. at 250 rpm $\eta_{pv}/\eta_{rv} = 0.86$ leaving a margin of 22 % for uncertainties.

3. Using equation (3.23), the sufficient condition for increasing the pressure level in the system is given by equation (3.25).

$$\left(D_p \cdot \eta_{pv} - \frac{D_r \cdot \eta_{rv}}{\alpha}\right) > \underbrace{\left(\frac{C_{rleak}}{\alpha} \cdot p_r + C_{pleak} \cdot p_p\right)}_{\text{positive}} \cdot \underbrace{\frac{1}{\omega_m}}_{\text{positive}} \tag{3.25}$$

   The condition in (3.25) states that a positive imbalance, between the weighted pump flow, must be present and must exceed the weighted sum of leakage flow. A simple ratio between the volumetric efficiencies can not be obtained for examination of this condition. A numerical evaluation of the worst case scenario, with respect to margin of uncertainty, presented previously i.e. $n_m = 3000$ rpm $\Rightarrow \eta_{pv}/\eta_{rv} = 1.01$, is therefore utilized to determine the limit of the condition. Assuming correctly calibrated leakage coefficients, numerical evaluation of the sufficient condition in equation (3.25) shows that $\eta_{pv}/\eta_{rv} > 1.06$ under these operation conditions. This leaves a margin of 5 % for uncertainties. In case this margin is exceed, the pressure may indeed increase when $\omega > 0$

4. The steady state volumetric efficiencies of the pumps are obtained empirically on similar pumps in (Rexroth, 2009) and (Rexroth, 2010). It is recognized that the pump efficiencies may deviate a few percent from these results, due to wear and tear, but is assessed that the margin of 5 % uncertainties is not exceeded.

From the discussion on the assumptions, applied during the analysis of the case $\omega_m > 0$, it is assessed that the result can be applied for further analysis. This means that the cases where $\omega_m > 0$, can be disregarded in the analysis and design of pressure control, as the pressure level in the system always decreases at steady piston velocity.

- **Case:** $\omega_m < 0$
When $\omega_m < 0$, it is necessary that $\sum Q_p < \frac{\sum Q_r}{\alpha}$ in order for the pressure to rise and requiring pressure control. This was shown in figure 3.4 on page 29. Using the same procedure as the previous case where $\omega_m > 0$, the analytical result is given in equation (3.26). In the case where $\omega_m < 0$, a necessary condition based on the sign of an expression is not enough to make a conclusion. Equation (3.26) is therefore a sufficient condition to determined if pressure control is needed.

$$\left(D_p \cdot \eta_{pv} - \frac{D_r \cdot \eta_{rv}}{\alpha}\right) < \underbrace{\left(\frac{C_{rleak}}{\alpha} \cdot p_r + C_{pleak} \cdot p_p\right)}_{\text{positive}} \cdot \underbrace{\frac{1}{\omega_m}}_{\text{negative}} \tag{3.26}$$

Equation (3.26) is the condition for $\sum Q_p < \frac{\sum Q_r}{\alpha}$ i.e. the need for pressure control, as the consequence of the flow imbalance is an increasing pressure level in the system. Instead of showing the general solution, it is sufficient to show at least one case where pressure control is needed. Such a case is given below:

$$\left.\begin{array}{r} \omega_m = -250 \text{ rpm} \\ p_p = 25 \text{ bar} \\ x_p = 750 \text{ mm} \end{array}\right\} \Rightarrow \left\{\begin{array}{r} p_r = 55.4 \text{ bar} \\ \eta_{pv} = 76.2 \ \% \\ \eta_{rv} = 83.4 \ \% \end{array}\right\}$$

$$\Downarrow$$

$$\underbrace{\left(D_p \cdot \eta_{pv} - \frac{D_r \cdot \eta_{rv}}{\alpha}\right)}_{=-5.8 \cdot 10^{-7}} < \underbrace{\left(\frac{C_{rleak}}{\alpha} \cdot p_r + C_{pleak} \cdot p_p\right) \cdot \frac{1}{\omega_m}}_{=-3.2 \cdot 10^{-7}}$$

Similar to the previous case, where it is shown that the pressure levels decrease when $\omega_m > 0$, the simulation model is utilized to show that the pressure levels indeed may increase with $\omega_m < 0$. The results are given in figure 3.8, where the shaft velocity is -250, -1000 and -3000 rpm, respectively. The initial piston position is set to $x_p = 750$ mm.

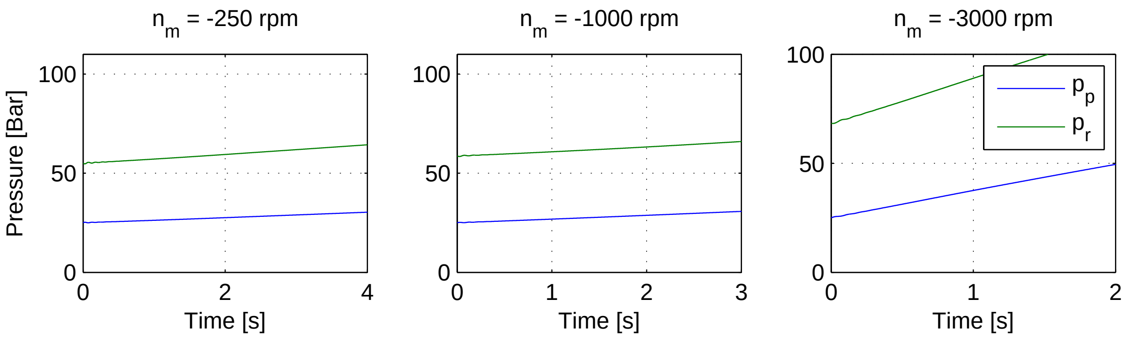

Figure 3.8. Simulations showing that the pressure levels may increase when $\omega_m > 0$. The initial piston position $x_p = 750$ mm i all cases. The initial piston velocity $\dot{x}_p = Q_{pP}/A_p$ i all cases.

Note that, for the case where $\omega_m < 0$, it has not been shown that the pressure levels always increase. It has only been shown that increasing pressure levels can occur. With regard to control of the pressure levels, this conclusion is sufficient to determine the need for pressure control.

From this analysis it is concluded that pressure control is not required when $\omega_m > 0$. However, when $\omega_m < 0$, it is required in at least some cases. The results of the steady state analysis are summarized in the following section.

3.3 Summary of Steady State Analysis

In this chapter, it is shown that the system has the following properties at steady piston velocity:

- The signs of the pressure gradients depend on the load acting on the piston, the flow balance in the cylinder and the rotational direction of the pumps.
- When the flow imbalance yields a decreasing pressure level in the system, one of the chamber pressures will go towards cavitation pressure: (the pressure in the remaining chamber varies in accordance with the load acting on the piston)
  - Pushing load: cavitation in any chamber, depending on the load magnitude.
  - Pulling load: cavitation in piston side chamber.
- When the flow imbalance is positive, it increases the pressure level in the system. The individual pressure levels are functions of time and load, when the piston velocity is in steady state.

Based on these properties, it is discussed when the pressures can be controlled. Furthermore, a strategy to control the pressure levels is formulated for the cases where it is possible:

- The two chamber pressures are coupled and can not be controlled individually i.e. reducing the pressure level in one chamber, using one of the PDVs, also reduces the pressure in the other chamber.
- As a compromise between response time in the piston velocity control loop and energy efficiency of the system, it is desired to hold the lowest chamber pressure at 25 bar, while the remaining varies to balance the load.
- The PDVs can only reduce the pressures, i.e. the pressures can only be controlled when the lowest pressure is above 25 bar.

- It is shown, with the steady state loads in this particular system, that the piston side pressure is always lower than the rod side pressure, whenever the lowest pressure is higher than 25 bar.

- In this system, with this particular load, only the piston side PDV is needed, as it is always the piston side pressure that requires to be controlled to maintain a constant level of 25 bar.

- Pressure control is only required when $\omega_m < 0$. When $\omega_m > 0$ the pressure level in the system always decreases.

4 Trajectories used for Performance Evaluation

In this chapter, a number of trajectories are designed. The trajectories are designed such that performance of the controllers can be evaluated on the ability to track a reference and the robustness towards disturbances and uncertainties. This means, the controllers should have the following properties:

- **Tracking performance:** The closed-loop system should be able to track a given reference trajectory, with as small average- and maximum control error as possible. The closed loop system should also be robust toward disturbances, parameter variations and uncertainties. Therefore the reference trajectory should be designed such that significant parameter variations occur.

To evaluate these properties, two types of trajectories are designed. These are listed below:

- **Quintic** (5th degree polynomial) **trajectory**
- **Ramp trajectory**

In the following, the properties of the two trajectory types are discussed and considerations on the magnitude of the reference signals are presented.

4.1 Quintic Trajectories

Quintic functions are used to design a trajectory which can test the tracking capabilities of a velocity or position controller. Using quintic functions to describe a trajectory, the desired acceleration, velocity and position of the piston can be limited to a finite value. This means that demands of, for example, infinite acceleration is avoided, making it possible for a controller to track the reference with no error, provided that the necessary flow rate and power is available.

A negative and a positive quintic trajectory is designed, as shown on the following page in figure 4.1(top) and 4.1(bottom), respectively. The quintic trajectories are designed from the following considerations:

- To avoid unrealistic motion demands, there cannot be steps in the piston velocity or acceleration.

- The trajectories are designed to go from a position of 100 mm to 650 mm and back or vice versa. This range is chosen such that there is a 100 mm margin to avoid the ends of the cylinder and to ensure significant parameter variations in the system.

- The velocity of the trajectory is designed from a desired servo speed of ±2500 rpm, corresponding to 83 % of the max speed of the servo. Assuming 100 % efficiency of the pumps this yields a steady state piston velocity of ±188 mm/s. The reason for choosing 2500 rpm is given after the trajectories.

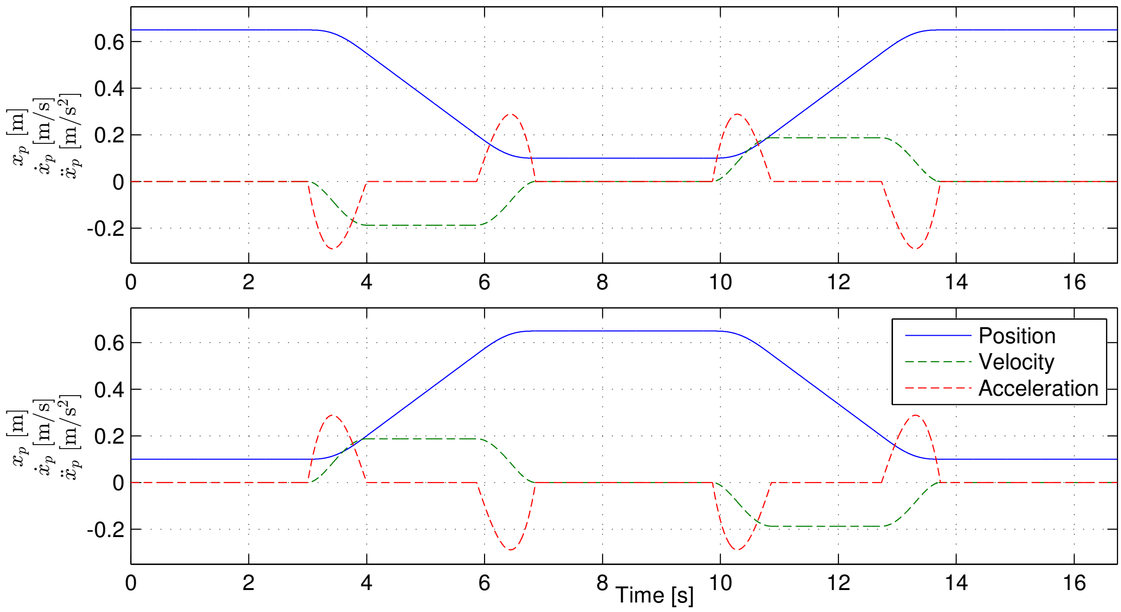

Figure 4.1. Showing the two quintic trajectories designed for testing the performance of the system. The top graph shows the negative trajectory, while the bottom graph shows the positive trajectory.

As seen in figure 4.1, the position, velocity and acceleration demands do not contain steps, providing good conditions for testing the tracking capabilities of the controller designs.

A desired servo speed of ±2500 rpm is chosen to ensure that the pressure in the piston side chamber reaches 25 bar or more. That the piston side chamber reaches 25 bar or more is essential to test the pressure control, which is designed to limit pressure at this level. Initial experiments reveal that this is not the case when the velocity is low. A low velocity trajectory was designed for a servo speed of 500 rpm, however, this does not cause a sufficient rise in pressure, as seen in the results of the experiment shown in figure 4.2 on the next page. The experiment was carried out using a P-controller, which was tuned on site and was not designed to ensure a given performance. An experiment was carried out rather than using the simulation model, as the accuracy of the model is limited, with respect to the magnitude of the pressure level. This was shown during validation of the model in section 2.2.

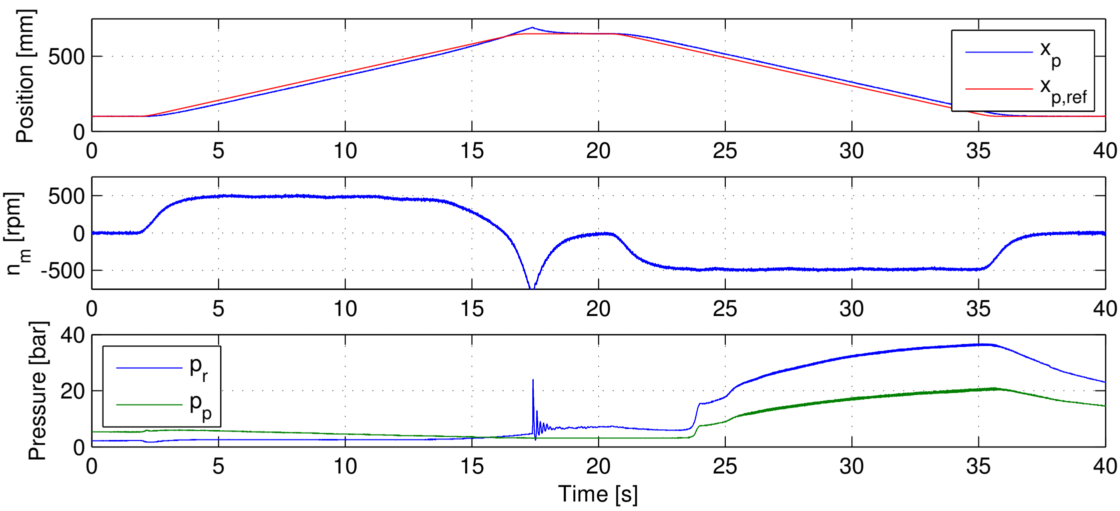

Figure 4.2. Showing the system response to a low velocity quintic trajectory using a P-controller.

As seen in figure 4.2, the piston side pressure do not rise above 25 bar, when applying the low velocity trajectory to the control system. From figure 4.2, it should furthermore be noted that the system is subject to both pushing- and pulling load during the test. This is observed from the pressure levels, which cross after approximately 15 seconds.

Using the same P-controller, an experiment was carried out with the high velocity trajectory in figure 4.1(bottom), designed for a servo speed of ±2500 rpm. The results of the experiment are given in figure 4.3.

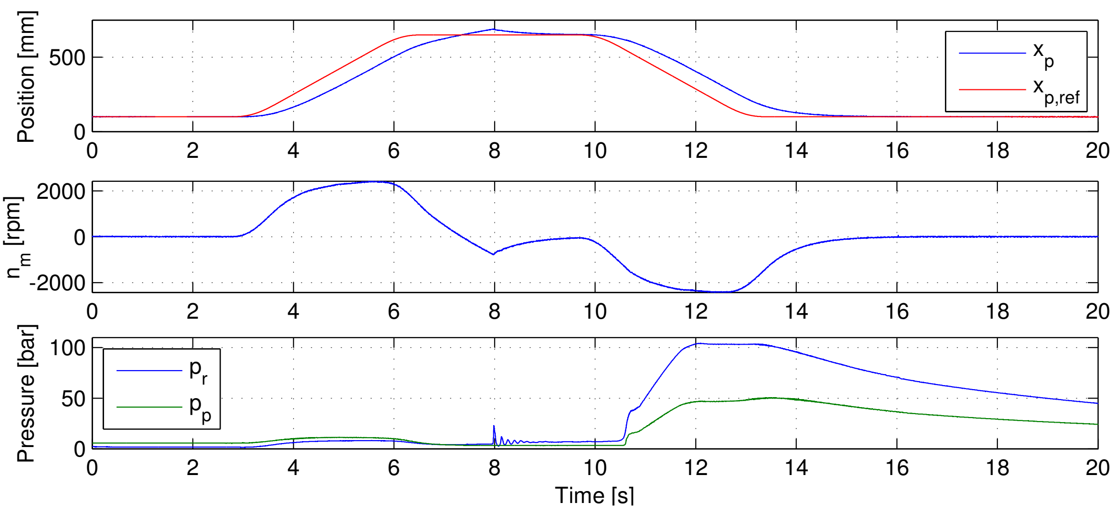

Figure 4.3. Showing the system response to a high velocity quintic trajectory using a P-controller.

The experimental results in figure 4.3, reveal that the piston side pressure indeed rises above 25 bar. This enables evaluation of the pressure control, whereby it is decided only to apply high velocity trajectories.

4.2 Ramp Trajectories

In addition to the quintic trajectory, two ramp trajectories are designed. These are deliberately designed to be impossible to track, as the acceleration demand is infinite. The purpose of the ramp trajectories is to excite the system dynamics. Similar to above, the two ramp trajectories are designed at a servo speed of ±2500 rpm, resulting in the trajectories shown in figure 4.4.

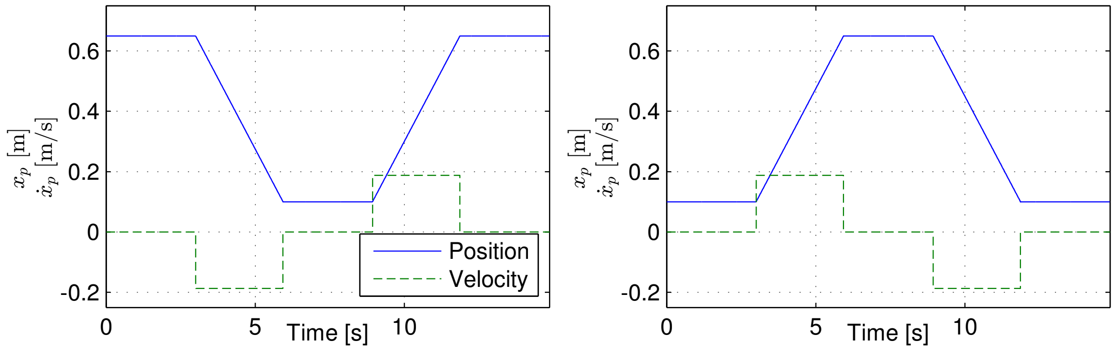

Figure 4.4. Showing the two ramp trajectories designed for testing the transient performance of the system. The left graph shows the negative trajectory, while the right graph shows the positive trajectory.

As seen in figure 4.4, the ramp trajectories consist of steps in velocity, which require infinite acceleration, and are therefore impossible to track without error. However, this is done intentionally to excite the system dynamics, and to assess the performance of the system when subjected to demanding inputs.

4.3 Summary of Trajectory Planning

Two types of trajectories are designed: quintic- and ramp trajectories. Quintic means that the trajectories are composed by pieces of 5th order polynomials, resulting in smooth acceleration-, velocity- and position references. With a smooth acceleration-, velocity- and position reference, the quintic trajectories provide a reference signal which should be achievable to track with little control error. The ramp trajectories are designed such that a step is given in the velocity command. This is done such that the controller performance can be evaluated, when the system dynamics are excited.

The trajectories are designed to provide significant parameter variations in the system when tracking the reference signal. This is achieved by evaluating the system in the stroke interval 100-600 mm, which yields both pushing and pulling load.

Finally, initial experimental tests reveal that high velocity trajectories are required to ensure a piston side pressure above 25 bar. The trajectories are therefore designed for 83 % of the maximum velocity.

Linear Model of SvDP-concept 5

In this chapter the nonlinear model is simplified and the system is linearized. The goal is to obtain a linear representation which enables analysis of the system. Using a combination of the initial system analysis in chapter 3 and this linear analysis, an applicable control structure is developed and controllers are designed in chapter 7. The linear model is obtained using the following simplifications of the system.

- The gravitational load is considered to be constant around any given operation point and therefore neglected in the linear model.
- The safety valves are considered inactive and therefore neglected.
- The PDV at the rod side is disregarded, as it was shown in chapter 3 that it is never needed with this particular load acting on the piston.
- The tank pressure is considered constant.
- The anti-cavitation configuration is assumed to be sufficiently fast to maintain a constant pressure between the pump and tank.
- The fluid temperature, viscosity and density are assumed constant.

Applying these assumptions to the nonlinear model yields the hydraulic diagram in figure 5.1.

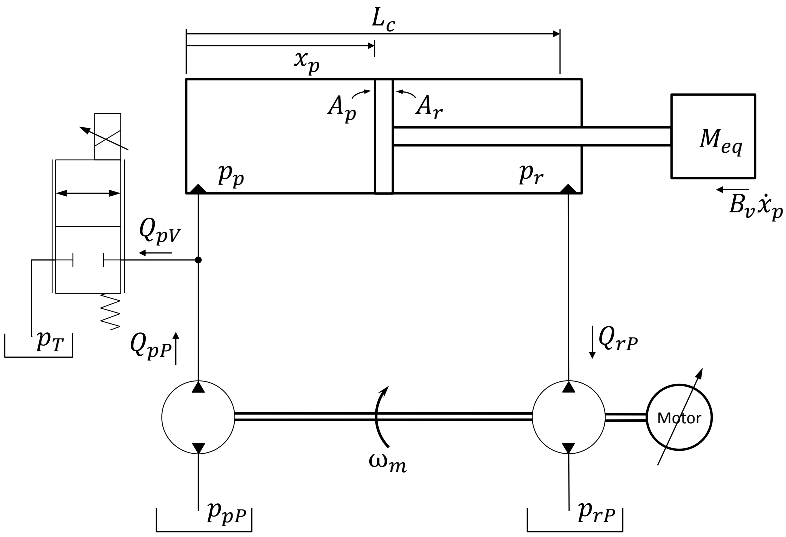

Figure 5.1. Schematic of the simplified hydraulic system.

5.1 Linear Model of the SvDP-concept

The linear model of the SvDP-concept is presented in this section. A thorough derivation of the linear equations is given in Appendix C. Δ is utilized throughout the linear model to symbolize a small change in a given variable and the subscript 0 denotes evaluation of a function in a specified operation point. The operation point (sometimes called linearization point) consists of three independent- and two dependent variables:

- *Independent variables:* piston position x_p, revolution of the pumps ω_m and the spool position of the PDV, denoted x_{pV}. The operation point, and thereby evaluation of the linear model, can be chosen arbitrary within the operation range of these variables.

- *Dependent variables:* chamber pressures p_p and p_r. It is important when linearizing the system around an operation point, that these variables are coherent with the application i.e. they are obtained from the nonlinear model in steady state using the independent variables as input.

The linear system is assumed to be time-invariant i.e. it is described by linear time-invariant (LTI) differential equations, which are derived in Appendix C. The linearized force balance of the piston from equation (2.1) on page 6 is given in equation (5.1).

$$\Delta\ddot{x}_p \cdot M_{eq0} = A_p \cdot \Delta p_p - A_r \cdot \Delta p_r - B_v \cdot \Delta\dot{x}_p \tag{5.1}$$

The change of inertia load, is modeled assuming a constant equivalent mass in the vicinity of the operation point. The equivalent mass is position dependent and the subscript 0 denotes evaluation at the operation point. It should be noted that the linear equations are obtained under the assumption of small changes in variables, and will deviate from the actual solution when moving away from the linearization point.

The linear model of the continuity equations requires a linear representation of the pump flows and the flow through the PDV. These are given in equations (5.2), (5.3) and (5.4), respectively. The derivations are given in Appendix C. Note that, the partial derivatives given in these equations, are obtained numerically, as the respective variables are described in look-up tables. The coefficients denoted K_{xx} are introduced to shorten the notation in the following.

$$\Delta Q_{pP} = \underbrace{D_p \cdot \left(\left.\frac{\partial \eta_{pv}}{\partial \omega_m}\right|_0 \cdot \omega_{m0} + \eta_{pv0}\left(p_{p0}, \omega_{m0}\right) \right)}_{K_{qpP\omega}} \cdot \Delta\omega_m + \underbrace{D_p \cdot \left.\frac{\partial \eta_{pv}}{\partial p_p}\right|_0 \cdot \omega_{m0}}_{K_{qpPp}} \cdot \Delta p_p \tag{5.2}$$

$$\Delta Q_{rP} = \underbrace{D_r \cdot \left(\left.\frac{\partial \eta_{rv}}{\partial \omega_m}\right|_0 \cdot \omega_{m0} + \eta_{rv0}\left(p_{r0}, \omega_{m0}\right) \right)}_{K_{qrP\omega}} \cdot \Delta\omega_m + \underbrace{D_r \cdot \left.\frac{\partial \eta_{rv}}{\partial p_r}\right|_0 \cdot \omega_{m0}}_{K_{qrPp}} \cdot \Delta p_r \tag{5.3}$$

$$\Delta Q_{pV} = \underbrace{\left.\frac{\partial Q_{pV}}{\partial x_{pV}}\right|_0}_{K_{qp}} \cdot \Delta x_{pV} + \underbrace{\left.\frac{\partial Q_{pV}}{\partial p_p}\right|_0}_{K_{qpp}} \cdot \Delta p_p \tag{5.4}$$

The linear representation of the continuity equations (2.5) and (2.6) on page 7 are given in equations (5.5) and (5.6) for the piston- and rod side chamber, respectively. The linear model of pump flows and the flow through the PDV, have been substituted into these equations using the coefficients defined in equations (5.2) → (5.4).

$$\Delta \dot{p}_p = \frac{\beta_{p0}}{V_{p0}} \cdot \left(K_{qpP\omega} \cdot \Delta\omega_m - \underbrace{\left(C_{pLeak} + K_{qpp} - K_{qpPp}\right)}_{K_{pleak}} \cdot \Delta p_p - K_{qp} \cdot \Delta x_{pV} - A_p \cdot \Delta \dot{x}_p \right) \tag{5.5}$$

$$\Delta \dot{p}_r = \frac{\beta_{r0}}{V_{r0}} \cdot \left(-K_{qrP\omega} \cdot \Delta\omega_m - \underbrace{\left(C_{rLeak} + K_{qrPp}\right)}_{K_{rleak}} \cdot \Delta p_r + A_r \cdot \Delta \dot{x}_p \right) \tag{5.6}$$

In equations (5.5) and (5.6) for the piston- and rod side chamber, respectively, the effective bulk modulus and the chamber volumes are considered constant in the vicinity of the operation point. It should be noted that the gradient of bulk modulus is rather high when the pressure level is low, which leads to an inaccurate linear model when moving away from the linearization point. The steep gradient is observed in figure 2.7 on page 15, where the bulk modulus is illustrated as a function of the pressure level.

The dynamics of the spool position in the valve, from input $x_{pV,ref}$ to output x_{pV}, is modeled as a first order system with a time constant τ_{PDV}. This yields the linear equation given by (5.7).

$$\Delta \dot{x}_{pV} \cdot \tau_{PDV} = \Delta x_{pV,ref} - \Delta x_{pV} \tag{5.7}$$

A second order differential equation has proven to be a reasonable approximation of the dynamics in the servo drive during validation in section 2.2. This yields equation (5.8), where $\omega_{ref,m}$ is the input to the motor and ω_m is the output.

$$\Delta \ddot{\omega}_m = \omega_{n,m}^2 \cdot \Delta\omega_{ref,m} - 2 \cdot \zeta_m \cdot \omega_{n,m} \cdot \Delta\dot{\omega}_m - \omega_{n,m}^2 \cdot \Delta\omega_m \tag{5.8}$$

Equations (5.1)→(5.8) conclude the linear model of the system. Next, the linear model is Laplace transformed, such that linear algebra can be utilized to solve the differential equations. When Laplace transforming the equations (5.1)→(5.8), it is assumed that the initial conditions are equal to zero. The Laplace transformed model is given in equations (5.9)→(5.13).

$$\dot{x}_p(s) = \frac{1}{M_{eq0} \cdot s + B_v} \cdot \left(A_p \cdot p_p(s) - A_r \cdot p_r(s)\right) \tag{5.9}$$

$$p_p(s) = \frac{\beta_{p0}}{V_{p0} \cdot s + K_{pleak} \cdot \beta_{p0}} \cdot \left(K_{qpP\omega} \cdot \omega_m(s) - K_{qp} \cdot x_{pV}(s) - A_p \cdot \dot{x}_p(s)\right) \tag{5.10}$$

$$p_r(s) = \frac{\beta_{r0}}{V_r \cdot s + K_{rleak} \cdot \beta_{r0}} \cdot \left(-K_{qrP\omega} \cdot \omega_m(s) + A_r \cdot \dot{x}_p(s)\right) \tag{5.11}$$

$$x_{pV}(s) = \frac{1}{\tau_{PDV} \cdot s + 1} \cdot x_{pV,ref}(s) \tag{5.12}$$

$$\omega_m(s) = \frac{\omega_{n,m}^2}{s^2 + 2 \cdot \zeta_m \cdot \omega_{n,m} \cdot s + \omega_{n,m}^2} \cdot \omega_{ref,m}(s) \tag{5.13}$$

To obtain an overview of the couplings in the system, a block diagram is provided in figure 5.2. The two inputs to the system are $x_{pV,ref}$ and $\omega_{m,ref}$. It is desired to control the states $\dot{x}_p$ and p_p, which are the piston velocity and the piston side chamber pressure, respectively.

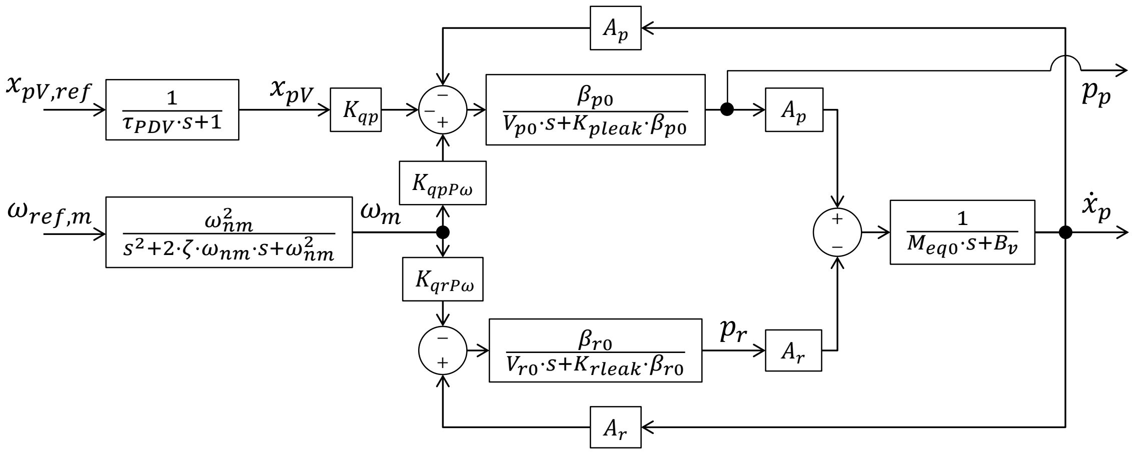

Figure 5.2. Blockdiagram of the Laplace transformed linear system given in equations (5.9) → (5.13).

The block diagram in figure 5.2, reveals that each input interacts with all outputs. The transfer functions can be obtained by manipulation and reduction of the block diagram describing each configuration. With two inputs and outputs, this yields four different configurations and thereby four transfer functions. Rather than deriving the transfer functions from the block diagram, the system is written in a state space representation, which provides a convenient and compact way of modeling the system. The state space representation of a continuous time-invariant linear system is given in equation (5.14).(Glad and Ljung, 2010)

$$\begin{aligned} \dot{\mathbf{x}}(t) &= \mathbf{A} \cdot \mathbf{x}(t) + \mathbf{B} \cdot \mathbf{u}(t) \\ \mathbf{y}(t) &= \mathbf{C} \cdot \mathbf{x}(t) \end{aligned} \tag{5.14}$$

When utilizing the state space representation of the system, given by equation (5.14), matrix manipulation can be utilized to obtain the transfer matrix $\mathbf{G}$. The different entries of $\mathbf{G}$ contain the transfer functions depending on the input/output configurations. The transfer matrix of a system is determined by equation (5.15).

$$\mathbf{G} = \mathbf{C} \cdot (s \cdot \mathbf{I} - \mathbf{A})^{-1} \cdot \mathbf{B} \tag{5.15}$$

In equation (5.14) $\mathbf{x}(t)$ is the time dependent state vector of the system and $\mathbf{u}(t)$ is the input vector or the control vector. $\mathbf{y}(t)$ is the output vector, whereas $\mathbf{A}$, $\mathbf{B}$ and $\mathbf{C}$ are the system-, input- and output matrices, respectively. For convenience (t) is omitted throughout the remaining of this report. The state vector of the system is given in equation (5.16).

$$\mathbf{x} = \begin{bmatrix} \dot{x}_p & p_p & p_r & \omega_m & \dot{\omega}_m & x_{pV} \end{bmatrix}^T \tag{5.16}$$

The input vector $\mathbf{u}$ is given in equation (5.17) and the output vector $\mathbf{y}$ in equation (5.18).

$$\mathbf{u} = \begin{bmatrix} \omega_{ref,m} & x_{pV,ref} \end{bmatrix}^T \tag{5.17}$$

$$\mathbf{y} = \begin{bmatrix} \dot{x}_p & p_p \end{bmatrix}^T \tag{5.18}$$

The system matrix $\mathbf{A}$ is formed based on the state vector and the linear system equations (5.1)→(5.8) on page 45, and is given in equation (5.19).

$$\mathbf{A} = \begin{bmatrix} \frac{-B_v}{M_{eq0}} & \frac{A_p}{M_{eq0}} & \frac{-A_r}{M_{eq0}} & 0 & 0 & 0 \\ \frac{-A_p\beta_{p0}}{V_{p0}} & \frac{-K_{pleak}\beta_{p0}}{V_{p0}} & 0 & \frac{K_{qpP\omega}\beta_{p0}}{V_{p0}} & 0 & \frac{-K_{qp}\beta_{p0}}{V_{p0}} \\ \frac{A_r\beta_{r0}}{V_{r0}} & 0 & \frac{-K_{rleak}\beta_{r0}}{V_{r0}} & \frac{-K_{qrP\omega}\beta_{r0}}{V_{r0}} & 0 & 0 \\ 0 & 0 & 0 & 0 & 1 & 0 \\ 0 & 0 & 0 & -\omega_{n,m}^2 & -2\zeta\omega_{n,m} & 0 \\ 0 & 0 & 0 & 0 & 0 & -\frac{1}{\tau_{PDV}} \end{bmatrix} \tag{5.19}$$

The corresponding $\mathbf{B}$ and $\mathbf{C}$ matrices are given in equations (5.20) and (5.21).

$$\mathbf{B} = \begin{bmatrix} 0 & 0 & 0 & 0 & \omega_{n,m}^2 & 0 \\ 0 & 0 & 0 & 0 & 0 & \frac{1}{\tau_{PDV}} \end{bmatrix}^T \tag{5.20}$$

$$\mathbf{C} = \begin{bmatrix} 1 & 0 & 0 & 0 & 0 & 0 \\ 0 & 1 & 0 & 0 & 0 & 0 \end{bmatrix} \tag{5.21}$$

The natural response and the stability of the system, can be studied from the eigenvalues of the system matrix $\mathbf{A}$. The stability region of a continuous time system is equal to the left half plane, not including the imaginary axis i.e. the real part of the eigenvalues must be negative for the system to be stable, (Glad and Ljung, 2010).

The system consists of six states i.e. six eigenvalues are obtained from $\mathbf{A}$. The poles related to the cylinder dynamics, are a function of the operation point, while the poles related to the dynamics of the servo drive and valve are constant.

A simplified linear system is established, to determined the critical operation point(s) of the cylinder. A critical operation point is considered to be the point at which the lowest possible natural frequency and damping ratio of the cylinder is obtained. In the simplified linear system, the dynamics of the servo drive and valve are disregarded, as these do not change and are assumed to be much faster than the remaining parts of the system. Later, in section 5.5 on page 58, it is shown to be a fair assumption. The simplified system is given in equation (5.22). The subscript $_\mathbf{s}$ is used to indicate that the system is simplified.

$$\underbrace{\begin{bmatrix} \ddot{x}_p \\ \dot{p}_p \\ \dot{p}_r \end{bmatrix}}_{\dot{\mathbf{x}}_\mathbf{s}} = \underbrace{\begin{bmatrix} \frac{-B_v}{M_{eq0}} & \frac{A_p}{M_{eq0}} & \frac{-A_r}{M_{eq0}} \\ \frac{-A_p\beta_{p0}}{V_{p0}} & \frac{-K_{pleak}\beta_{p0}}{V_{p0}} & 0 \\ \frac{A_r\beta_{r0}}{V_{r0}} & 0 & \frac{-K_{rleak}\beta_{r0}}{V_{r0}} \end{bmatrix}}_{\mathbf{A}_\mathbf{s}} \cdot \underbrace{\begin{bmatrix} \dot{x}_p \\ p_p \\ p_r \end{bmatrix}}_{\mathbf{x}_\mathbf{s}} + \underbrace{\begin{bmatrix} 0 & 0 \\ \frac{K_{qpP\omega}\beta_{p0}}{V_{p0}} & \frac{-K_{qp}\beta_{p0}}{V_{p0}} \\ \frac{-K_{qrP\omega}\beta_{r0}}{V_{r0}} & 0 \end{bmatrix}}_{\mathbf{B}_\mathbf{s}} \cdot \underbrace{\begin{bmatrix} \omega_m \\ x_{pV} \end{bmatrix}}_{\mathbf{u}_\mathbf{s}}$$

$$\underbrace{\begin{bmatrix} \dot{x}_p \\ p_p \end{bmatrix}}_{\mathbf{y}_\mathbf{s}} = \underbrace{\begin{bmatrix} 1 & 0 & 0 \\ 0 & 1 & 0 \end{bmatrix}}_{\mathbf{C}_\mathbf{s}} \cdot \begin{bmatrix} \dot{x}_p \\ p_p \\ p_r \end{bmatrix} \tag{5.22}$$

In the following section, the eigenvalues of $\mathbf{A}_\mathbf{s}$ are examined. The critical operation points are analyzed from numerical evaluation of the system. This approach is chosen rather than analyzing the analytical result, as the order of the system is three, which makes it difficult to determine the individual parameters influence on pole locations. If the individual parameters influence can not be determined, the numerical result provides the same information as the analytical.

5.2 Determination of Critical Operation Point(s)

In the following, the system characteristics are examined at different operation points, in order to determine the critical operation point(s) of the system. The operation points, which are examined, are extracted from the trajectories designed in section 4 on page 39.

- The system will operate with shaft velocities around ±2500 rpm and 0 rpm during tracking of the trajectories. Analysis of the system with a pump velocity equal to 0 rpm is not possible, as data is not available in this vicinity. It is therefore assumed that this case can be represented using shaft velocities of ±250 rpm. $n_m = 250$ rpm is the lowest speed, where data of the pumps is available and thereby the lowest speed at which the pump flow can be linearized with confidence in the result.

- The trajectories yield that the system will operate in the stroke interval 100-650 mm. From the literature e.g. (Andersen, 2003), it is known that the natural frequency of a cylinder decreases with an increasing inertia load. In (Andersen, 2003), it is also shown that the minimum natural frequency is obtained when the ratio between the chamber volumes are equal to one. This is provided that the inertia load is constant, which is not the case in this system. In figure 2.9 on page 16, showing the inertia load as a function of piston position, it was shown that the inertia load increases significantly towards the end positions. Simulations of the system reveal that the change of inertia load, throughout the stroke interval 100-650 mm, is the dominating part with respect to changes in the natural frequency of the system. The increasing inertia load towards the end positions, yields a decreasing natural frequency compared to the remaining positions. This property is illustrated with simulations in section 5.4 on page 54, where the linear model is verified. Therefore the characteristics of the system is examined at the operation points $x_p = 100$ and 650 mm. In addition to these operation points, the middle position of 375 mm is chosen arbitrary to confirm and illustrate that the natural frequency indeed is lower at the end positions.

- The PDV is a pressure compensated valve and is therefore considered pressure independent. This is justified in figure 2.3 on page 10, showing that the valve characteristics are almost pressure independent when the pressure is above 20 bar. This means that the leakage coefficient K_{pleak}, is independent of the valve i.e the eigenvalues of the simplified system matrix $\mathbf{A_s}$, are independent of the valve. If this assumption is not true, the leakage coefficient K_{pleak} increases, meaning that the consequence of this assumption is an underestimation of the damping in the system.

Based on this knowledge, the eigenvalues of the simplified system matrix $\mathbf{A_s}$, are examined at the operation points listed in table 5.1 on the next page. The pressure levels, listed at the different operation points, are obtained by solving the nonlinear system equations at the respective piston position and velocity. When solving the equations it is assumed that the system is controlled. This means, the system is considered in a state where the piston side pressure is controlled to 25 bar when possible. In the remaining cases, the load acting on the piston, determines which chamber reaches the crack pressure of the anti-cavitation system. The applied assumptions are marked in the table as follows:

† $\omega_m < 0$ leads to increasing pressure, however, it is assumed that p_p is controlled to 25 bar using the valve. This assumption is made in accordance with the pressure control strategy, formulated in section 3.2 on page 28.

* Due to leakage in the chambers, the pressure in both chambers decreases until one chamber reaches the crack pressure of the anti cavitation system. This property was shown in the initial analysis of the system, chapter 3. The sign and magnitude of the load determines which chamber that reaches the crack pressure.

$^{\diamond}$ $\omega_m > 0$ leads to decreasing pressure, however, the combined load and viscous friction leads to lower pressure in the rod side chamber, whereby the anti cavitation system is activated in the rod side chamber. This property was also shown in the steady state analysis, chapter 3.

	Piston position (x_p)		
Velocity $\dot{x}_p$ (n_m)	100 mm	375 mm	650 mm
-187.5 mm/s (-2500 rpm)	$p_p = 25$ bar† $p_r = 55.7$ bar	$p_p = 25$ bar† $p_r = 59.6$ bar	$p_p = 25$ bar† $p_r = 63.9$ bar
0 mm/s ($\pm$250 rpm)	$p_p = 5.1$ bar $p_r = 2.5$ bar*	$p_p = 3.2$ bar $p_r = 2.5$ bar*	$p_p = 2.5$ bar* $p_r = 5.5$ bar
187.5 mm/s (2500 rpm)	$p_p = 8.9$ bar $p_r = 2.5$ bar$^\diamond$	$p_p = 6.9$ bar $p_r = 2.5$ bar$^\diamond$	$p_p = 4.7$ bar $p_r = 2.5$ bar$^\diamond$

Table 5.1. Overview of the operation points used to analyze the linear model.

Using the operation points listed in table 5.1, the cylinder characteristics are examined in the following with the coherent pump speed, piston position and pressure levels. The natural frequency and damping ratio is in focus during evaluation of the simplified system. Prior to this evaluation, the special case with a piston velocity equal to 0 mm/s, is examined:

- **Special Case $\dot{x}_p = 0$ mm/s:** The purpose of this analysis is to examine if the case where $\dot{x}_p = 0$ mm/s, can be represented using a pump velocity of either -250 rpm or 250 rpm.

  Ideally the pump speed is equal to 0 rpm when the piston velocity is 0 mm/s. In this system, that is not the case during control of the system, due to leakage which the pump must compensate for. Analysis of the system with a pump velocity lower than 250 rpm is not possible, as data is not available. It is therefore assumed that this case can be represented using the shaft velocity of $\pm$250 rpm, which is the lowest velocity where data of the pumps is available.

  It is known that the vicious friction in the cylinder depends on the direction of motion. This was shown during validation of the simulation model in section 2.2 on page 17. At positive velocity, the magnitude of the vicious friction coefficient is half of the coefficient when the velocity is negative. This affects the pressure levels, as these are a function of the combined load acting on the piston. As a consequence of this, the stiffness of the fluid changes. The cylinder characteristics therefore change with the direction of motion.

  The eigenvalues of the simplified system matrix $\mathbf{A_s}$ are illustrated to the left in figure 5.3 on the facing page for the two cases where the pump speed is $\pm$250 rpm and the piston position is 650 mm. Three eigenvalues are obtained in each case. One stable pole is placed in the vicinity of zero, which relates to the flow imbalance between the two chambers. This pole is examined further during control design in chapter 7. For now it is the pressure dynamic that is of interest, represented by the complex conjugated pole pair. The natural frequency and the damping ratio are illustrated for the operation points, where $\dot{x}_p = 0$ mm/s, to the right in figure 5.3.

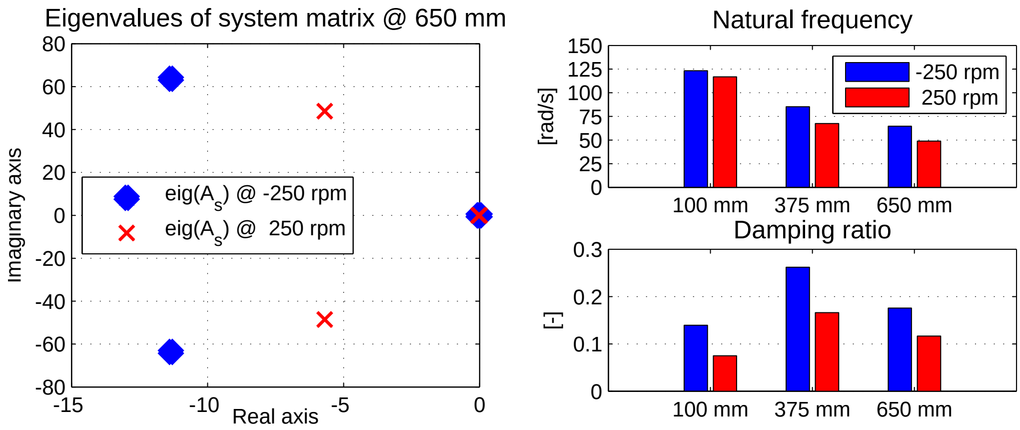

Figure 5.3. Left: Eigenvalues of the simplified system matrix $\mathbf{A_s}$ at x_p = 650 mm and n_m = ±250 rpm. Right: Natural frequency and damping ratio for the operation points listed in table 5.1, where $\dot{x}_p$ = 0 mm/s.

From figure 5.3, it is clear that the natural frequency and damping ratio of the pressure dynamics, in all operation points are lower when the pump speed is positive. With respect to choosing the critical operation point(s), it is therefore decided to represent the case where $\dot{x}_p$ = 0 mm/s, with a pump speed of 250 rpm.

The natural frequency and damping ratio of the pressure dynamics, are illustrated in figure 5.4 for the operation points listed in table 5.1 on the facing page.

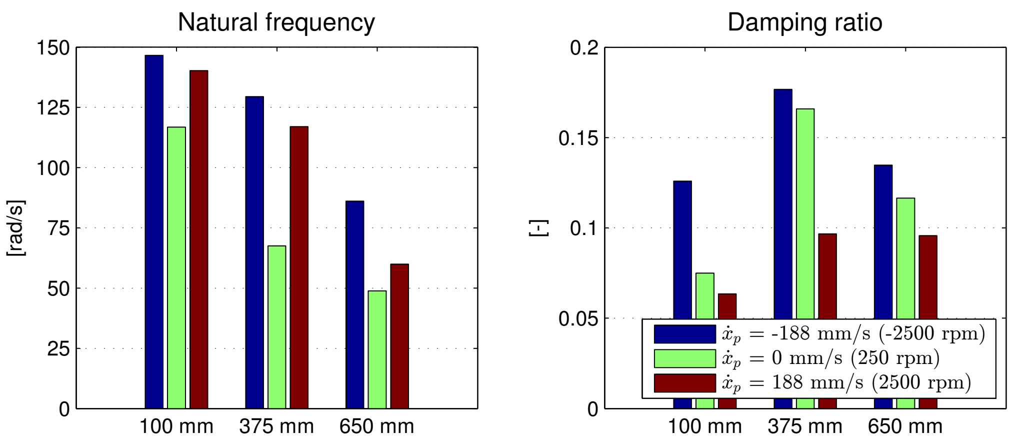

Figure 5.4. Natural frequency (left) and damping ratio (right) of the simplified system for all operation points listed in table 5.1 on the facing page.

From results, presented in figure 5.4, the following considerations are made on the critical operation point(s), with respect to the natural frequency and the damping ratio:

Natural Frequency:

From figure 5.4(left), it should be noted that the natural frequency of the pressure dynamics changes from approximately 50 rad/s to 150 rad/s, depending on the operation point. The eigenfrequency is lowest at the piston position 650 mm, independent of the pump speed and thereby the pressure levels. In general, the eigenfrequency decreases with the pressure level, which results in the lowest natural frequencies at positive pump velocities.

Damping Ratio:

In figure 5.4(right), it is shown that the damping ratio of the system is found in the interval 0.07-0.17 for the operation points listed in table 5.1 on page 50. This means that the damping ratio is relatively low at all operation points, but is generally lower at the end positions.

Depending on the control objective, two operation points are found to be critical. The critical operation points are chosen from the following argumentation on the control objectives. Through this argumentation, a low natural frequency is weighted higher than the damping, when choosing the critical operation points with respect to the control objective:

Velocity Control:

With velocity control as the objective, it is concluded that the critical operation point is found when x_p = 650 mm and the pump speed is positive. At this position the eigenfrequency is 50 rad/s, when n_m = 250 rpm. With n_m = 2500 rpm the eigenfrequency is approximately 60 rad/s. The eigenfrequency is low in both cases, but the margin of uncertainties is relatively large at low pump speeds, with respect to the volumetric efficiencies and thereby the pressure dynamics. The critical operation point, used for further analysis of velocity control, is therefore chosen at n_m = 2500 rpm and x_p = 650 mm. The consequence of this choice, is that the performance requirements must be conservative, as it is known that the natural frequency can be approximately 10 rad/s lower at low pump velocities. This was shown in figure 5.4 on the preceding page.

Piston Side Pressure Control:

When pressure control is the objective, the critical operation point can only be chosen from one of the cases where the piston side pressure is 25 bar or above. In all other cases, the piston side pressure never reaches a level where it requires control. These restrictions yield that the servo speed must be negative. From figure 5.4, the lowest natural frequency is found at n_m = -2500 rpm and x_p = 650 mm.

From the argumentation given above, two critical operation points are found. The linearization variables are listed below:

- $$\begin{array}{ll} \text{Independent variables} & \text{Dependent variables} \\ \left.\begin{array}{ll} x_p & = 650 \text{ mm} \\ n_m & = 2500 \text{ rpm} \end{array}\right\} \Rightarrow & \left\{\begin{array}{ll} p_p & = 4.7 \text{ bar} \\ p_r & = 2.5 \text{ bar} \\ x_{pV} & = 0 \text{ \%} \end{array}\right. \end{array}$$

- $$\begin{array}{ll} \text{Independent variables} & \text{Dependent variables} \\ \left.\begin{array}{ll} x_p & = 650 \text{ mm} \\ n_m & = -2500 \text{ rpm} \end{array}\right\} \Rightarrow & \left\{\begin{array}{ll} p_p & = 25 \text{ bar} \\ p_r & = 63.9 \text{ bar} \\ x_{pV} & = 32.3 \text{ \%} \end{array}\right. \end{array}$$

At the critical operation points, the valve opening becomes a dependent variable, as the PDV is assumed to regulate the piston side pressure to 25 bar. It is only active at negative pump speeds, as shown in the initial analysis of the system in chapter 3. The valve opening is determined such that it compensates the flow imbalance between the pumps, resulting in a constant pressure level. At $x_p = 650$ mm and $n_m = -2500$ rpm, the flow imbalance is 2.12 L/min, corresponding to a valve opening of 30.5 % when the pressure differential across the valve is 25 bar.

In the following section, the linear model is evaluated at the critical operation points and the transfer matrices are obtained. Hereafter, the linear models are verified by comparison with their nonlinear counter parts.

5.3 Transfer Matrices at the Critical Operation Points

Due to the complexity of the system equations and the lack of useful information from the high order characteristic polynomials, the analytical result of the transfer functions are omitted and the system is evaluated at the critical operation point using numerical values. Note that it is the complete system that is evaluated in the following and not the simplified, where the servo- and valve dynamics are disregarded.

When the shaft speed is positive, the transfer matrix is denoted $\mathbf{G}^+$. The system is given in equation (5.23), where the outputs are the piston velocity and the piston side pressure. The system inputs are the reference signals for the servo motor velocity and for the spool position of the piston side PDV. Note that the PDV is inactive when the shaft speed is positive, as the piston side pressure never rises above 25 bar in this case.

$$\underbrace{\begin{bmatrix} \dot{x}_p \\ p_p \end{bmatrix}}_{\mathbf{y}} = \underbrace{\frac{1}{(s^2+11.4s+2569)(s+0.03)} \begin{bmatrix} \frac{7.2\text{e}5(s+0.03)}{(s^2+439.8+3.9\text{e}5)} & 0 \\ \frac{7.5\text{e}10(s+12.6)(s-1.2)}{(s^2+439.8+3.9\text{e}5)} & 0 \end{bmatrix}}_{\mathbf{G}^+} \cdot \underbrace{\begin{bmatrix} \omega_{ref,m} \\ x_{pV,ref} \end{bmatrix}}_{\mathbf{u}} \tag{5.23}$$

Equation (5.23) can be reduced to a SISO control problem, as the piston side pressure can not be controlled and therefore is not of interest, when the pump speed is positive. This reduces the control problem at positive pump velocity to equation (5.24).

$$\frac{\dot{x}_p}{\omega_{ref,m}} = \underbrace{\frac{7.2\text{e}5}{(s^2+11.4s+2569)(s^2+439.8+3.9\text{e}5)}}_{G^+} \tag{5.24}$$

When the shaft speed is negative, the transfer matrix is denoted $\mathbf{G}^{-}$. The system is given in equation (5.25), where the input/output configuration is the same as the previous case, where the shaft speed is positive. Note that the PDV is active in this case, but $x_{pV,ref}$ is restricted to not taking negative values, as the valve is a 2/2-proportional directional valve.

$$\underbrace{\begin{bmatrix} \dot{x}_p \\ p_p \end{bmatrix}}_{\mathbf{y}} = \underbrace{\frac{1}{(s^2+23.14s+7085)(s+0.23)} \begin{bmatrix} \frac{2e6(s+0.24)}{(s^2+439.8s+3.9e5)} & \frac{3.2e4(s-0.43)}{(s+62.5)} \\ \frac{1.6e11(s+26.3)(s-4.1)}{(s^2+439.8s+3.9e5)} & \frac{-4.4e9(s^2+22.3s+3062)}{(s+62.5)} \end{bmatrix}}_{\mathbf{G}^{-}} \cdot \underbrace{\begin{bmatrix} \omega_{ref,m} \\ x_{pV,ref} \end{bmatrix}}_{\mathbf{u}} \tag{5.25}$$

In equation (5.25), it should be noted that a right half-plane zero is present in each off-diagonal element of $\mathbf{G}^{-}$ i.e. in $\mathbf{G}^{-}_{\mathbf{12}}$ there is a zero at s = 0.43 and in $\mathbf{G}^{-}_{\mathbf{21}}$ has a zero at s = 4.1. A zero in the right half-plane makes a system non-minimum phase and is characterized by an unusual step respose in the time domain. When a system contains precisely one right half-plane zero, the step response is initially in the opposite direction of the final value. (Glad and Ljung, 2010) Furthermore the entry $\mathbf{G}^{-}_{\mathbf{22}}$, should be noted. The negative gain makes the transfer function $p_p/x_{pV,ref}$, a non-minimum phase system as $x_{pV,ref}$ is always positive. This means that the phase is shifted 180°. The first considerations on non-minimum phase systems are made in chapter 7, where a decentralized control strategy is designed by treating the MIMO system as two SISO systems. The linear models are verified by comparison with their nonlinear counter parts in the following.

5.4 Verification of the Linear Model

In this section, the linear models are verified by comparison with the nonlinear model. The verifications are performed by comparison of a step response.

Verification of G^{+}

In figure 5.5, the models are compared when the initial pump velocity is 2500 rpm. This means that the transfer function G^{+} is verified. A step of 100 rpm is applied at the time equal to zero. This corresponds to a step of 1.7% of the nominal input range. As the initial velocity is 83% of the maximum speed, the piston position changes from 650 mm to 746 mm during the simulation time of the nonlinear model. As seen in figure 5.5 on the next page, this yields significant parameter variations, which decreases the hydro-mechanical eigenfrequency throughout the simulation.

From figure 5.5 on the facing page, it is seen that the linear model G^{+}, matches the dynamics of the nonlinear system in the vicinity of the operation point, while it starts deviating when the piston position changes. From this, it should be noted that the parameter variations are significant in the vicinity of the operation point, causing a decreasing hydro-mechanical eigenfrequency and increasing damping of the system when the piston moves beyond a position of 650 mm. If the piston moves beyond the position 650 mm due to overshoot in the position control system, a decreasing the hydro-mechanical

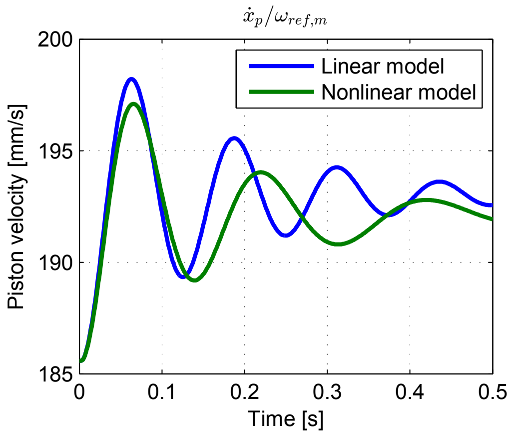

Figure 5.5. Step responses from linear- and nonlinear model with initial velocity n_m = 2500 rpm and initial position x_p = 650 mm i.e. step response of G^+. Applied velocity step: 100 rpm.

eigenfrequency can lead to stability issues during operation of the system. Knowing this, the position control for positive velocity, presented in chapter 7, should ideally be designed such that overshoot is avoided.

Verification of $\mathbf{G}^-$

To verified the linear model $\mathbf{G}^-$ for negative pump velocity, the individual entries of $\mathbf{G}^-$ are compared with the simulation model. $\mathbf{G}^-$ is verified by separately applying a step in the inputs $\omega_{ref,m}$ and $x_{pV,ref}$.

In figure 5.6, the models are compared when the initial pump velocity is -2500 rpm and the initial piston side pressure is 25 bar. Figure 5.6 (left) illustrates the piston velocity, when applying a step of -100 rpm (1.7% of the nominal input range) i.e. G^-_{11} is compared with the simulation model. Figure 5.6 (right) illustrates the piston side pressure, when a step of -100 rpm is applied i.e. G^-_{21} is compared with the simulation model.

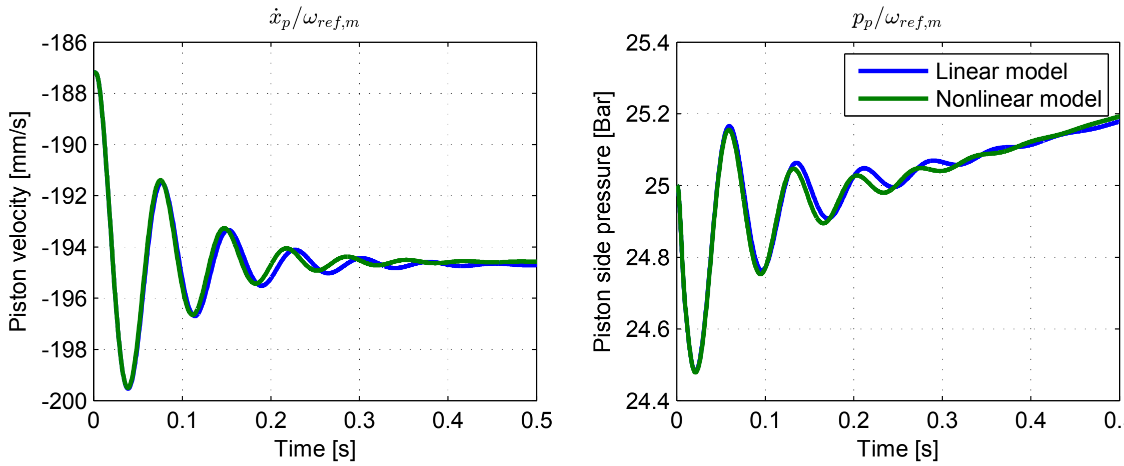

Figure 5.6. Step responses from the linear- and nonlinear model with initial velocity n_m = -2500 rpm, initial position x_p = 650 mm and initial valve opening x_{pV} = 30.5% i.e. step response of G^-_{11} (left) and G^-_{21} (right). Applied velocity step: -100 rpm.

From figure 5.6, it is concluded that the linear models G^-_{11} and G^-_{21}, match the nonlinear model very well in the vicinity of the operation point. Note that the deviation is caused by changing piston position in the nonlinear simulation model. The piston position decreases from 650 mm to 550 mm during the simulation time, resulting in an increasing hydro-mechanical eigenfrequency. This result confirms the analysis in section 5.2 on page 48, where the critical operation point is determined, showing that the lowest hydro-mechanical eigenfrequency is obtained at the end position 650 mm (only considering the operation interval x_p = 100 to 650 mm).

In figure 5.7, the responses of a step in the spool position of the valve, are given. A step corresponding to 5 % of the nominal input range is given to the valve. Such large step is given to illustrate the significant gain change. This is discussed after the figure.

Again, the initial pump velocity is -2500 rpm and the initial piston side pressure is 25 bar. Figure 5.7 (left) shows the response of the linear- and nonlinear model in the piston velocity when a step in the valve opening is applied at time zero. The linear model is given by G^-_{12}. Figure 5.7 (right) illustrates the response of the linear- and nonlinear model in the piston side pressure i.e. the linear model is given by G^-_{22}.

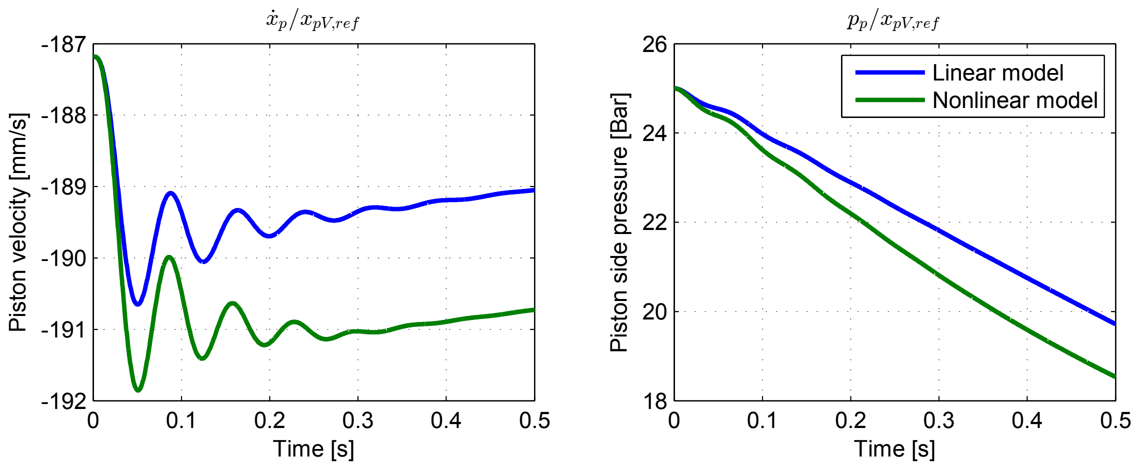

Figure 5.7. Step responses from linear- and nonlinear model with initial velocity n_m = -2500 rpm, initial position x_p = 650 mm and initial valve opening x_{pV} = 30.5% i.e. step response of G^-_{12} (left) and G^-_{22} (right). Applied step to the valve: 5 %.

In figure 5.7, it is clear that the dynamic in the two models are fairly similar. Again the hydro-mechanical eigenfrequency increases during the simulation, as a consequence of the decreasing piston position. It can also be seen in figure 5.7, that the gain is too low in the linear model, resulting in the offset between the two models. The difference in the gain, originates from linearization of the PDV. The PDV is not a proportional valve, which means that the flow gain changes as a function of the spool position. The flow gain of the valve is illustrated in figure 5.8 on the next page at a pressure differential of 25 bar.

From figure 5.8 it should be noted that the flow gain is approximately constant for valve openings above 35 %, while it changes significantly when the valve opening is lower. It is this effect that this seen in figure 5.7, where the step input changes the spool position from the initial value of 30.5 % to 35.5 % opening.

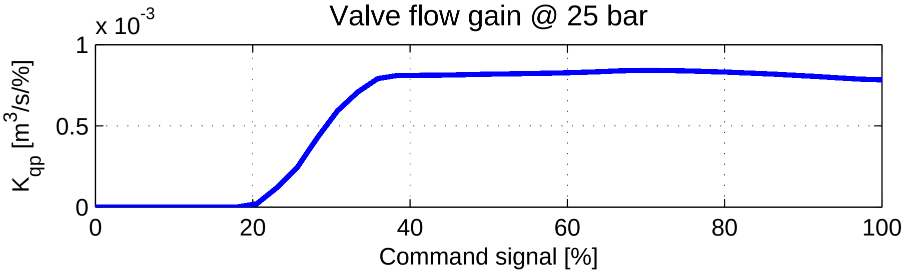

Figure 5.8. Flow gain of the valve as a function of spool position at a pressure differential of 25 bar.

The significant change of the flow gain can be treated during the controller design, by utilizing a conservative gain margin, to ensure stability of the system. Instead of this approach, the system is linearized around a valve opening of 35 % (high flow gain), such that this property does not affect the design process. Thereby is it known that the valve flow gain can only remain constant or decrease during operation. If the flow gain decreases during operation the result is an increasing gain margin. Thereby stability issues are avoided. In figure 5.9, the linear model with a valve opening of 35 %, is compared to the nonlinear simulation model.

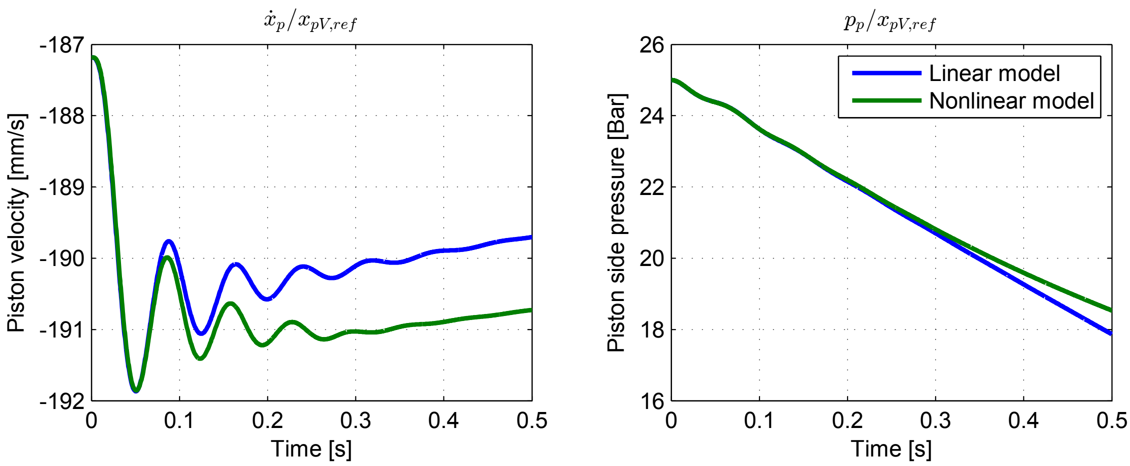

Figure 5.9. Step responses from linear- and nonlinear model with initial velocity n_m = -2500 rpm, initial position x_p = 650 mm and initial valve opening x_{pV} = 35 % i.e. step response of G^{-}_{12} (left) and G^{-}_{22} (right). Applied step to the valve: 5 %.

From figure 5.9, it is observed that both the gain and the dynamics of the linear model, match the nonlinear model in the vicinity of the operation point. The linear models have hereby been verified throughout this section and are observed to be valid in the vicinity of the operation points. In the following section, the verified linear models are simplified.

5.5 Simplified Linear Model

In this section the linear models are simplified for clarity in the transfer functions by neglecting insignificant dynamics of the system. This means that the linear system is simplified such that only the dominating dynamics remain. The simplified linear system is utilized in the process of controller design in the following chapters, whereby only the dominating dynamics are considered. This may lead to additional tuning of the controllers, when implemented in the nonlinear model, however it simplifies the design process as clarity in the transfer functions is obtained.

Simplification of G^+

The transfer function G^+, presented in equation (5.24) on page 53, describing the complete system from $\omega_{ref,m}$ to $\dot{x}_p$, is compared to a simplified version in figure 5.10. The simplified system was presented in equation (5.22) on page 48, where the servo dynamic is omitted. In figure 5.10, it is clear that the servo dynamic is so fast, compared to the hydro-mechanical dynamic, that it can be assumed $\omega_m(t) = \omega_{ref,m}(t)$, which is the case in the simplified linear model.

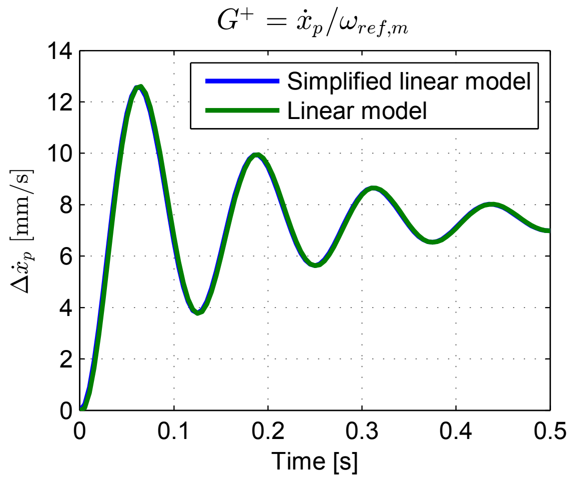

Figure 5.10. Step responses from complete- and simplified linear model. Initial velocity n_m = 2500 rpm and initial position x_p = 650 mm. Applied velocity step: 100 rpm.

Due to the negligible difference between the complete- and simplified linear model in figure 5.10, the transfer function G^+ is approximated by the simplified transfer function G_s^+. This is shown in equation (5.26).

$$\frac{\dot{x}_p}{\omega_{ref,m}} = \underbrace{\frac{7.2\text{e}5}{(s^2 + 11.4s + 2569)(s^2 + 439.8 + 3.9\text{e}5)}}_{G^+} \approx \underbrace{\frac{1.8}{(s^2 + 11.4s + 2569)}}_{G_s^+} \tag{5.26}$$

The simplified transfer function G_s^+ is a second order system from which the natural frequency and damping ratio of the system, are given as:

Dynamic Characteristics of G_s^+	(positive motion)
Natural frequency $\omega_{n,s}$	8.07 [Hz]
Damping ratio ζ_s	0.11 [-]
System gain K_s	707.16e-6 [m/rad]

The simplified transfer function G_s^+ will be used for further analysis of the system and controller designs in the following chapters.

Simplification of $\mathbf{G}^-$

The same procedure is applied to simplify the transfer matrix $\mathbf{G}^-$. The complete linear model from equation (5.25) on page 54 is compared to the simplified linear model, presented in equation(5.22) on page 48, where the servo drive- and valve dynamics are omitted. The step response of the individual entries are shown in figure 5.11

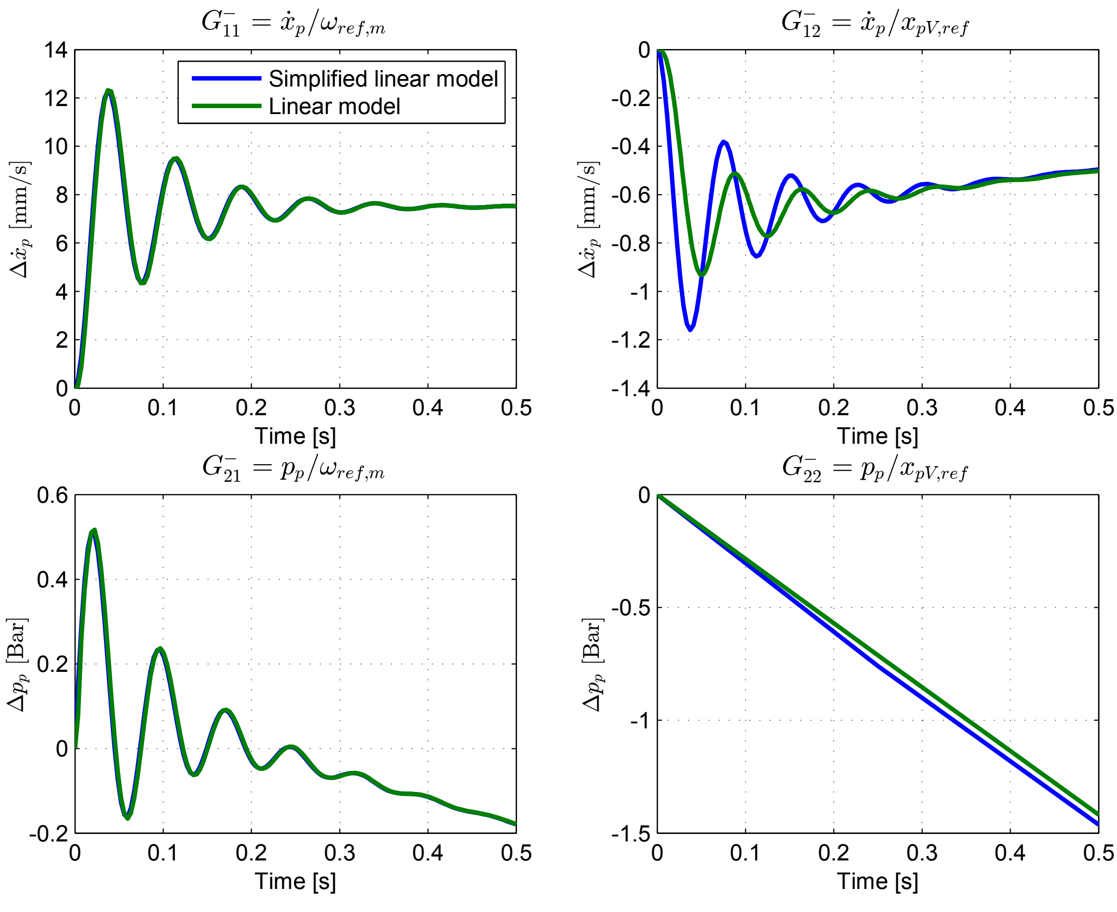

Figure 5.11. Step responses from complete- and simplified linear model. Initial velocity n_m = -2500 rpm, initial position x_p = 650 mm and initial valve opening x_{pV} = 35.0%. Velocity step: 100 rpm applied to G_{11}^- (top-left) and G_{21}^- (bottom-left). Valve step: 1 % applied to G_{12}^- (top-right) and G_{22}^- (bottom-right).

From figure 5.11, it is clear that the dynamics of the servo drive are negligible (see G_{11}^- (top-left) and G_{21}^- (bottom-left)), as the step response of the complete- and simplified linear model is practically identical in the two entries where $\omega_{ref,m}$ is the input. To the right in figure 5.11, it is evident, mainly from the entry G_{12}^{-} (top-right), that the valve dynamics interacts with the hydro-mechanical dynamics. The eigenfrequency and damping are still the same in the two systems, but the first order filter in the valve causes a phase shift in the complete model compared to the simplified. From these observations, it is assessed that the simplified model represents the dominating dynamics of the system and therefore provides a sufficient linear model for control design.

The simplified transfer matrix $\mathbf{G_s^-}$, for negative velocity, is given in equation (5.27) and will be used for further analysis of the system and controller designs in the following chapters.

$$\begin{bmatrix} \dot{x}_p \\ p_p \end{bmatrix} = \underbrace{\begin{bmatrix} \frac{5.05(s+0.24)}{(s^2+23.14s+7085)(s+0.23)} & \frac{-505.3(s-0.43)}{(s^2+23.14s+7085)(s+0.23)} \\ \frac{4e5(s+26.3)(s-4.1)}{(s^2+23.14s+7085)(s+0.23)} & \frac{-7.1e7(s^2+22.3s+3062)}{(s^2+23.14s+7085)(s+0.23)} \end{bmatrix}}_{\mathbf{G}_s^-} \cdot \begin{bmatrix} \omega_{ref,m} \\ x_{pV,ref} \end{bmatrix} \tag{5.27}$$

5.6 Summary of Linear Model Analysis

A linearization of the SvDP-concept is carried out to establish a linear model of the system. The linear equations are written in state space form, which provides a convenient and compact representation of the system. The eigenvalues of the hydro-mechanical system are analyzed from a simplified system (valve- and servo drive dynamics are neglected). The analysis reveals two critical operation points: One point for positive pump speed and one for negative pump speed.

Hereafter, the linear system is considered as two parts. For positive velocities, the transfer matrix $\mathbf{G}$ is reduced to a single transfer function G^+, describing the behavior between the input $\omega_{ref,m}$ and the output $\dot{x}_p$. This is possible because the piston side pressure never needs to be regulated at positive velocities (shown in chapter 3), resulting in the valve being inactive. For negative velocities, the transfer matrix $\mathbf{G}^-$ is established.

The complete linear models (including the dynamics of the servo drive and valve), are verified by comparison with the nonlinear simulation model. The verification reveals significant parameter variations in the vicinity of the operation points. This resulted in an adjustment of the valve flow gain, by linearization of the system around a valve opening of 35 % rather than the original 30.5 %. At valve openings above 35 %, the PDV has a linear flow characteristics with respect to the valve opening. This adjustment ensures that the valve flow gain can only remain constant or decrease. If the flow gain decreases during operation the result is an increasing gain margin. Using this adjustment, complications during operation of the system, with respect to stability issues, are avoided, when the controller design is performed with respect to the high (constant) valve flow gain obtained at 35 % valve opening.

Finally, the complete linear system is reduced by comparing the model with a simplified linear model. The comparison reveals that the valve- and servo drive dynamics can be neglected when designing controllers in the following chapters.

Problem Statement 6

The motivation for this thesis is to investigate if the SvDP-concept can be utilized as an alternative to the traditional valve-cylinder combination, with regards to controlling actuation of a cylinder. For this purpose, a nonlinear simulation model of the SvDP-concept has been established along with a linear model. From these models, the properties of the SvDP-concept have been studied and the analysis reveals that the match between effective pump displacements and the piston area ratio is essential for the system behavior. In the setup provided for experimental tests, the ratio between the effective pump displacements is always higher than the piston area ratio. This yields the system properties listed below, at steady state piston velocity. To determine if pressure control is needed, a requirement of 25 bar in the low pressure chamber, is specified. It is decided that the lowest chamber pressure should be 25 bar when possible, to obtain a stiff system where acceptable tracking performance can be achieved while keeping the pressure level at an acceptable level.

- **Positive shaft speed:** Decreasing pressure levels - pressure control **not** required
- **Negative shaft speed:** Increasing pressure levels - pressure control required

The properties listed above result in characteristics of the system that change with the direction of motion. Therefore, the system is analyzed in both cases, where the two critical operation points are determined. At positive velocity the lowest chamber pressure never exceeds the requirement for pressure control to be needed, reducing the control system to a SISO system. At negative velocity, pressure control is required along with velocity control of the piston. In this case, the SvDP-concept is a MIMO system. From these properties, the problem statement follows:

Is it possible to make a hydraulic cylinder connected to the SvDP-concept track a given velocity reference, while maintaining the lowest chamber pressure at a maximum of 25 bar, such that an energy efficient alternative to the traditional valve-cylinder configuration, is obtained?

To answer the problem statement, the system is divided into the cases listed above, where two control strategies are needed: One for positive velocity and another for negative velocity. This is done to improve the achievable tracking performance, by developing a control strategy where a set of controllers are designed for the system dynamics in the individual case. Such a strategy requires design of a switching strategy, enabling switching between the two sets of controllers, in order for the system to complete a desired task in the industry. The focus will not be on development of a switching strategy, but to clarify the achievable performance by examining the two cases individually.

To prove the concept, a simple design approach is taken, where two sets of SISO controllers are developed. A control strategy with SISO controllers is chosen, as templates for these controller structures are commonly available in industrial control software. The MIMO system, present at negative velocity, is therefore examined to determine a decentralized control strategy, where the system can be considered as two SISO systems. With a decentralized control strategy established, two sets of controllers are designed.

The performance is evaluated by the ability of the control system to track the reference signals, designed in chapter 4, and is measured on the rms velocity error.

7 Decentralized Control Strategy

In this chapter, a decentralized control strategy is developed and evaluated. This means, the MIMO system is considered as two SISO systems, such that SISO control can be applied. The controllers are tested in the laboratory and the test results, obtained with the different controllers, are presented and compared in chapter 8.

Initially the control problem is divided into two situations, in accordance with the results obtained in chapter 5. The two control situations are listed below:

- At positive piston velocity, only the piston velocity can be controlled, as the piston side pressure never reaches a level where it requires control i.e. the control problem is a SISO system.

- At negative piston velocity, both the piston velocity and piston side pressure need to be controlled i.e. the plant is a MIMO system.

The two situations result in two different control problems with very different characteristics of the system. In the first situation, at positive velocity, the control problem is already reduced to a SISO problem, as the pressure level is always low. The low pressure level results in a low hydro-mechanical eigenfrequency, compared to the second situation where the pressure level is higher.

In the second situation, at negative velocity, the pressure level may rise above 25 bar, resulting in a MIMO system as both piston velocity and piston side pressure need to be controlled. The MIMO system is therefore examined to determine a decentralized control strategy, such that the system can be considered as two SISO systems. The main task of the control systems, designed throughout this chapter, is to obtain high tracking performance with respect to the piston velocity. The secondary task is to maintain a limited pressure level of 25 bar. For evaluation of the control systems in the laboratory, an outer control loop is designed to regulate the piston position. A position loop is included to ensure a consistent evaluation basis, as the piston position drifts due to leakage in the system. With a position loop, it is ensured that all controllers are subject to the same parameter variations related to the piston position.

The controller designs are divided into two tasks, due to limitations in the test facilities.

The limitations arise, when estimating the piston velocity from the measured piston position. In chapter 8, is it shown that low frequency noise in the position signal prevents a good velocity estimation, resulting in a chattering control input to the servo drive when velocity controllers with a proportional gain is utilized. The controller designs are therefore divided into two tasks with the following goals:

- **Conservative and robust control:** The goal of this design task is to obtain a set of controllers that can be realized and tested in the current configuration of the physical test setup. The low frequency noise, in the position signal, prevents a good velocity estimation, which limits the achievable bandwidth of the velocity control. A conservative design approach is therefore taken, where for example proportional gain of the chattering velocity error is avoided. Furthermore, the control input is filtered conservatively, such that the control system is robust towards the chattering velocity estimation. These controller designs are carried out in section 7.1 and 7.2, for positive- and negative velocity, respectively.

- **High tracking performance:** The goal of this design task is to obtain a set of controllers, which delivers a high tracking performance, assuming the necessary equipment is available. The controller designs do therefore not encounter the problems, related to the velocity estimation, as it is assumed that a good velocity feedback signal is available. To increase the achievable bandwidth of the velocity control, active pressure feedback is utilized to improve the poor damping of the system. The controllers, designed with the goal of high tracking performance, can not be tested due to the previous argumentation, regarding noisy position measurements, and is therefore only evaluated from simulations. The controller designs and simulations are presented in section 7.3.

Finally, in section 7.4, the need of a switching strategy is elaborated. If the control system is to be realized for tracking of the trajectories presented in chapter 4, an automated strategy for switching between the two control strategies, is needed. Development of a switching strategy has not be prioritized in this thesis and is therefore only discussed, and the need elaborated, in section 7.4.

7.1 Controller Design for Positive Velocity

In this section, controllers (realizable in the current test setup) are designed for positive piston velocity and tested in the simulation model i.e. controllers are designed for the SISO plant G_s^+ from section 5.5. At positive piston velocity, the simplified plant is given by equation (5.26) on page 58, which is reviewed below:

$$\frac{\dot{x}_p}{\omega_{ref,m}} = \underbrace{\frac{1.8}{(s^2 + 11.4s + 2569)}}_{G_s^+} \tag{7.1}$$

The task of the controller is to drive the error of the system to zero and obtain the highest possible bandwidth. The design criteria are elaborated, prior to the controller design, below. It is known from the table on page 58, that G_s^+ is poorly damped with a damping ratio of 0.11 and an eigenfrequency at 8.07 Hz. The Bode diagram of G_s^+ is given in figure 7.1, showing that the poor damping results in a resonance peak of 13 dB at the eigenfrequency 50.1 rad/s. This means, the input is amplified by a factor of 4.5 at the eigenfrequency, compared to the steady state amplification.

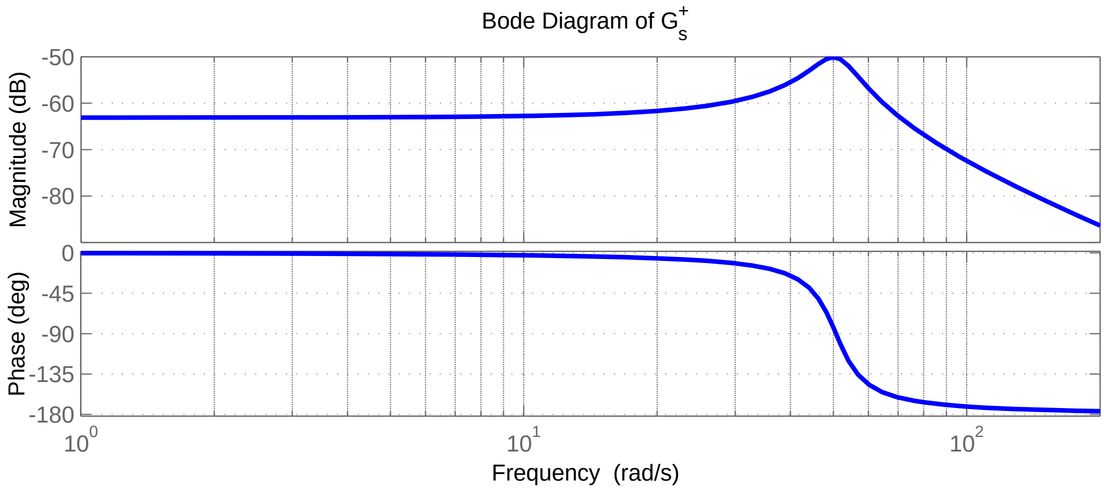

Figure 7.1. Bode diagram of G_s^+, the transfer function from ω_m to $\dot{x}_p$ at positive velocity.

The poor damping ratio, results in a high resonance peak, as shown in figure 7.1, which limits the achievable bandwidth considerably. Using active damping (pressure feedback), the resonance peak can be reduced. However, this feature is not included until the controller designs in section 7.3, where the goal is to obtain a high tracking performance. In this section, where the goal is to obtain a controller design, that can be evaluated in the laboratory, despite noisy signals, the resonance peak is maintained and treated as the limit of achievable bandwidth. In the following a controller is designed to regulate the piston velocity, which is a common task in the industry. This is followed by design of a position controller, which is utilized to ensure consistent evaluation basis, as the piston position drifts due to leakage. The purpose of the position loop is to ensure that all controllers are subject to the same parameter variations, related to the piston position, during tests.

7.1.1 Velocity Controller

In this subsection, a velocity controller, denoted G_{vc}^+, is designed. The control system is sketched in figure 7.2, where $\dot{x}_{ref,p}$ is the velocity reference and $\omega_{ref,m}$ is the control input to the system.

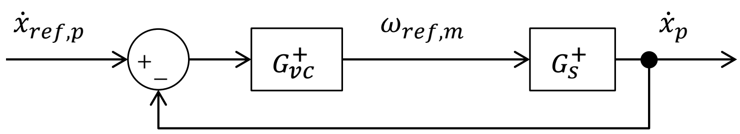

Figure 7.2. Blockdiagram of velocity loop.

A set of design criteria for the velocity control is specified below, where each choice is elaborated. The only strict requirement is stability of the closed loop system. The remaining criteria listed, are aims in the design process. The design criteria are utilized throughout all velocity controller designs performed in this section and in section 7.2 and 7.3.

- **Stability** - The system should be stable at all times. This means that all closed loop poles must be located in the left half-plane. This requirement must be strictly satisfied, whereas the following criteria are aims and not strict requirements.

- **Overshoot < 10 %** - The system is evaluated using the trajectories, presented in chapter 4, which requires 83 % of maximum pump speed in steady state. To avoid saturation of the pump speed, when regulating the flow rate, 10 % overshoot can be accepted, leaving a margin of 7 % for gain variations.

- **Gain Margin: GM > 10 dB** - A conservative gain margin of 10 dB is chosen to encounter for parameter uncertainties and modeling inaccuracies related to the simplifications.

- **Phase Margin: PM $>$** $45°$ - This margin is likewise chosen to encounter for parameter uncertainties and modeling inaccuracies, such that the system remains stable despite uncertainties and inaccuracies in the linear model.

- **Bandwidth: As high as possible** - in general. In this section and 7.2, the bandwidth, with respect to velocity control, is maintained low to ensure that problems, related to poor velocity estimation does not result in chattering control inputs.

The velocity plant G_s^+ is of type 0. If the controller G_{vc}^+ only consists of a proportional gain, a steady state error occurs when a step input is applied to the system. To avoid this steady state error at step inputs, a free integrator is introduced in the controller, making the open velocity loop a type 1 system. As the velocity feedback is of poor quality, due to the argumentation given above and shown in chapter 8, it is decided to filter the control input such that the eigenfrequency of the system is not excited and chatter in the control input is reduced. A second order input filter is placed 16 rad/s below the eigenfrequency, to suppress the resonance peak. The gain is hereafter raised such that the design criteria are met. This yields the velocity controller given in equation (7.2).

$$G_{vc}^+ = \frac{15.6 \cdot 10^6}{s \cdot (s + 34)^2} \tag{7.2}$$

The resulting open loop Bode diagram is given to the left in figure 7.3 on the next page, showing a gain margin of 11 dB and a phase margin of 57.6°, which both meet the design criteria. The closed loop bandwidth is 18.65 rad/s, which is approximately 3 Hz. The bandwidth is not impressive, but cannot be increased, using this controller structure, without violating the design criteria. The step response of the closed loop system is given to the right in figure 7.3, where it is seen that the overshoot is 10 % and there is no steady state error.

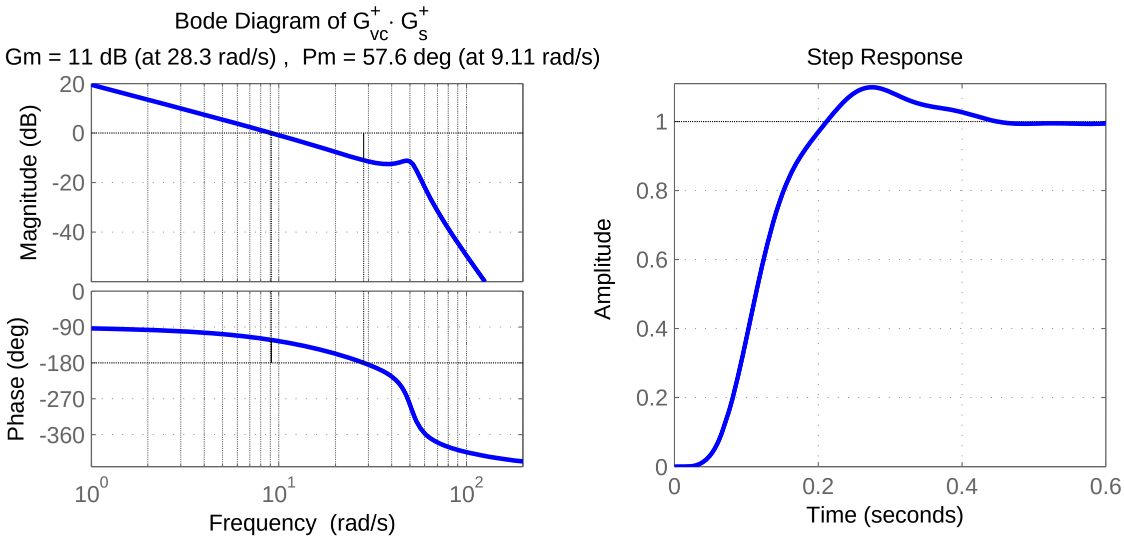

Figure 7.3. Left: Open loop Bode plot of $G_{vc}^{+} \cdot G_{s}^{+}$. Right: Step response of closed velocity loop.

To evaluate the controller performance, the trajectory provides a position reference as input to the system, that is to be tracked. Therefore an additional loop (position loop) is added and a controller is designed in the following.

7.1.2 Position Controller

The complete control system is sketched in figure 7.4, which is now a cascade control structure, where the position controller G_{pc}^{+} is to be designed.

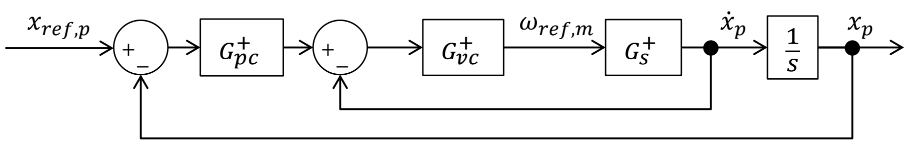

Figure 7.4. Blockdiagram of the control system at positive velocity.

The position controller G_{pc}^{+} is designed, aiming for the same criteria as listed above. The system G_{p}^{+}, that needs to be controlled by the controller G_{pc}^{+}, is given in equation (7.3).

$$G_{p}^{+} = \frac{G_{vc}^{+} \cdot G_{s}^{+}}{1 + G_{vc}^{+} \cdot G_{s}^{+}} \cdot \frac{1}{s} \tag{7.3}$$

The free integrator, seen in equation (7.3), makes the open loop system a type 1 system, so no steady state error occurs at step inputs. The position controller G_{pc}^{+}, is therefore designed as a proportional gain. The gain is determined such that the crossover frequency in the position loop, is approximately half the crossover frequency of the velocity loop. This makes the velocity loop twice as fast as the position loop, allowing the velocity controller to adjust the control input. Ideally, the velocity loop should be at least 5 times faster than the position loop, such that the dynamics of the velocity loop can be disregarded when designing the position controller. If the inner loop is much faster than the outer, it can always be expected that the velocity is equal to the command. But due to the low bandwidth of the velocity loop, it is decided to lower the limit. Furthermore, the proportional gain of G^+_{pc}, is determined such that the overshoot does not exceed 10 %. These requirements yield the position controller given in equation (7.4)

$$G^+_{pc} = 4.8 \tag{7.4}$$

The resulting Bode diagram of the open loop system is given to the left in figure 7.5. The step response of the closed position loop is given to the right in figure 7.5, where an overshoot of 10 % is observed. The closed loop bandwidth is 11.54 rad/s, which is approximately 1.8 Hz.

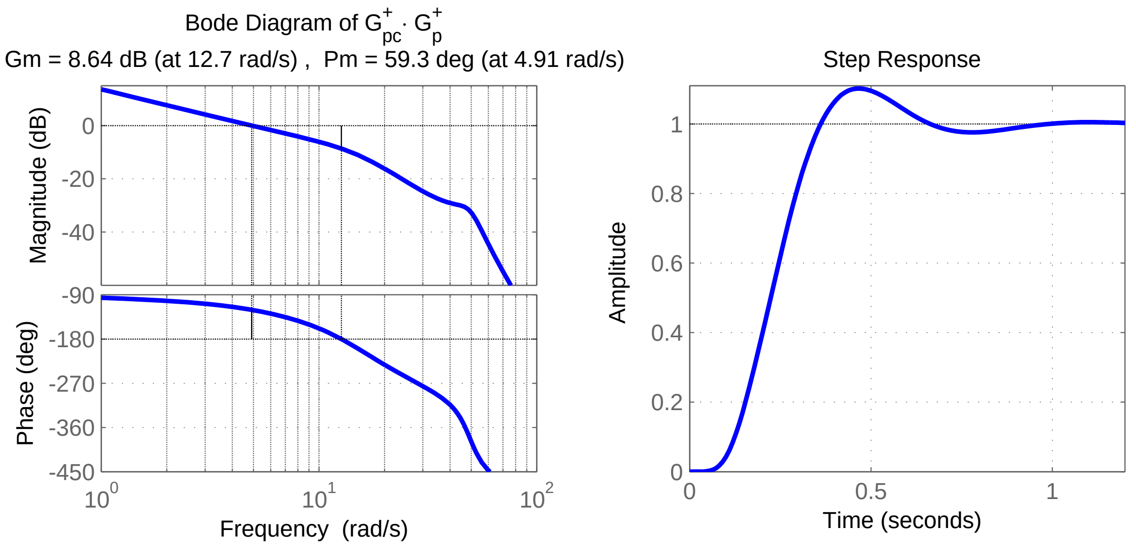

Figure 7.5. Left: Open loop Bode plot of $G^+_{pc} \cdot G^+_p$. Right: Step response of closed position loop.

To improve the response of the control system, the velocity reference is provided as feedforward. This is possible, as the trajectories are designed such that the position reference is differentiable. This yields the control structure illustrated in figure 7.6, which is implemented in the simulation model and the test setup.

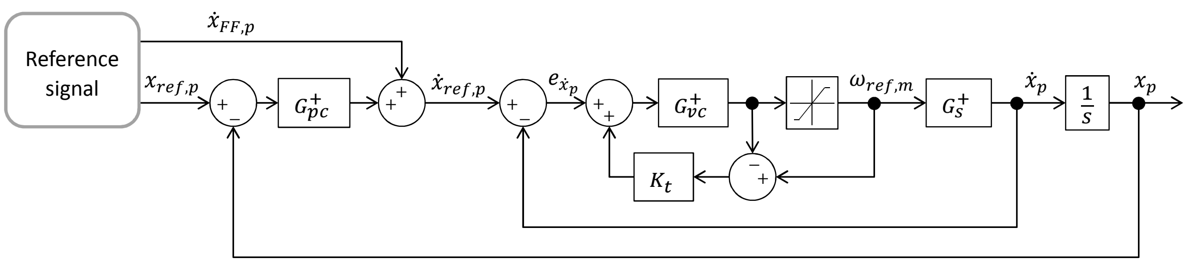

Figure 7.6. Blockdiagram of final control system at positive velocities.

Besides feedforward of the velocity reference, anti windup is implemented to accommodate windup in the velocity controller G_{vc}^{+}. The velocity controller G_{vc}^{+} contains an integrator, which will windup if the control input is saturated. $\omega_{ref,m}$ is limited to ± 3000 rpm, being the maximum speed of the pumps. The factor K_t, shown in figure 7.6, is a tuning factor that is adjusted using the simulation model. K_t determines the rate at which the excessive command signal is subtracted in the integrator. The conventional way of implementing anti windup is to subtract the excessive signal directly from the integrator, but in this case it is fed back through the input filter as well. This is done to ease the implementation process in the laboratory and has revealed no significant difference during simulations.

A simulation of the control system, with the designed controllers, is given in the following subsection for initial performance evaluation.

7.1.3 Simulation of Control System at Positive Velocity

Results of two simulations are presented in the following. The simulations are carried out using parts of the two trajectory types, presented in chapter 4. Only the parts, where the velocity reference is positive, are utilized in the following.

Simulation with Quintic Trajectory

In figure 7.7 on the next page, a simulation is given, where the quintic trajectory is applied as reference to the system. To the left in figure 7.7, the reference position- and velocity of the piston, is compared to the simulated response. The position- and velocity errors are given to the right along with the control input to the servo drive. Furthermore, the simulated pressure levels are provided in the bottom, showing that the pressure levels never exceed 10 bar, resulting in low stiffness of the system.

From the simulation, in figure 7.7 on the following page, it is evident that the control system is capable of tracking the quintic trajectory, given as reference signal, despite closed loop bandwidths of 1.8 and 3 Hz in the position- and velocity loop respectively. The root mean square (rms) error in the piston position is 2.68 mm and the rms velocity error is 15.44 mm/s, throughout the simulation. The errors occur during the transient periods, as both steady state errors are zero.

The position control has an overshoot of up to 6 mm when the input changes, whilst the steady state error is almost zero. The maximum velocity error is 38 mm/s, which occurs at times, where the reference can be approximated by a ramp. This error is expected as the velocity loop is a type 1 system, resulting in a steady state error at ramp inputs. At constant velocity, the error is zero due to the free integrator present in the velocity controller.

At the time 4.4 seconds, an undershoot occurs. The undershoot occurs due to cavitation of the piston side chamber. Here the anti cavitation system is activated, letting oil into the piston side chamber, while the piston side pump is trying to pump oil out of the chamber. This results in no movement of the piston, causing the rod side pressure to increase as the

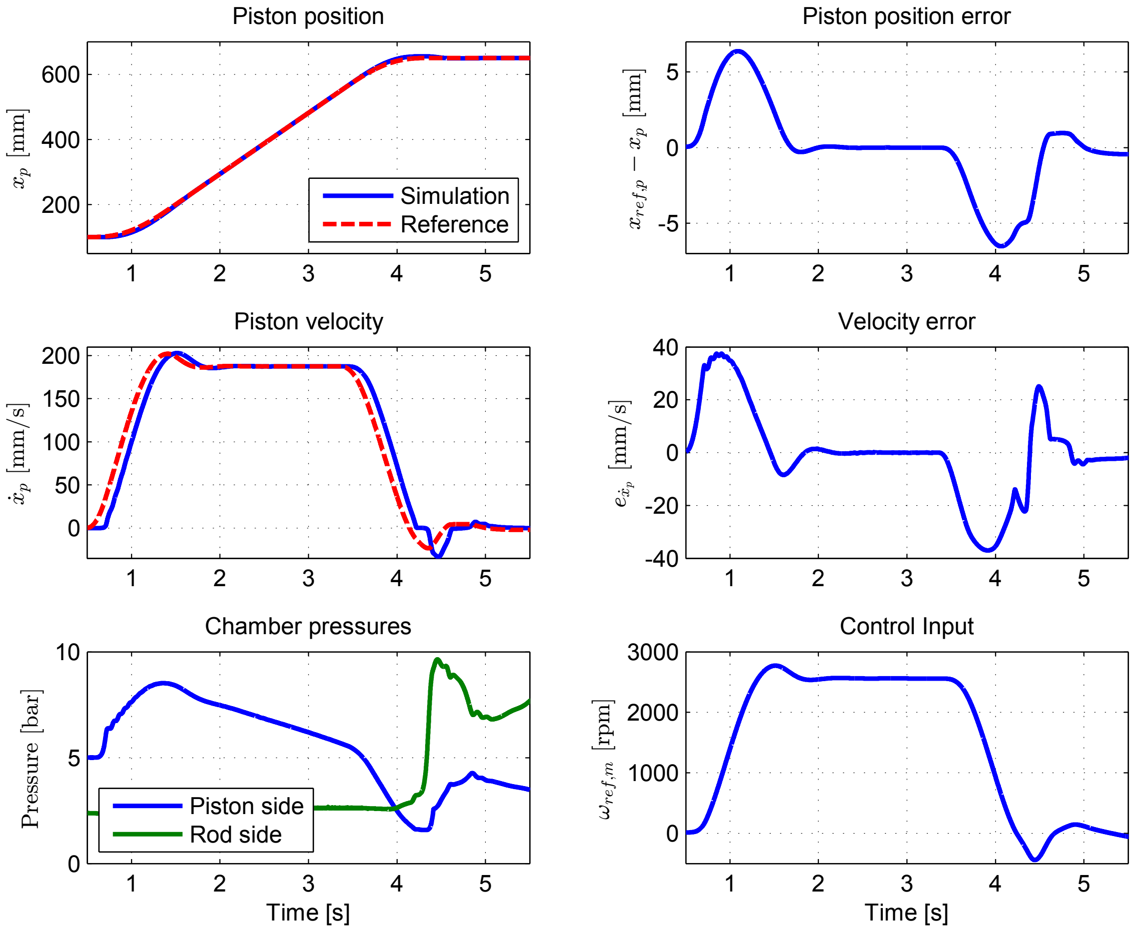

Figure 7.7. Simulation of the system controlled by the controllers designed for positive velocity. Left: Piston position and velocity, compared to the reference signals, along with the chamber pressures. Right: Piston position- and velocity error along this the input signal to the servo drive.

rod side pump is pumping oil into the chamber. Eventually the piston starts moving, but the low bandwidth of the velocity loop results in an overshoot of 25 mm/s.

Furthermore, the control input should be noted. From figure 7.7 it it observed that a continuous and well-behaved input is given to the system. The control input is never saturated by the limit of ± 3000 rpm, so windup in the integrator is not an issue.

With the limitations and performance evaluated, it is assessed that the obtained tracking performance, with respect to the quintic trajectory, is acceptable for both velocity and position control.

Simulation with Ramp Trajectory

In the following the tracking performance of the control system is evaluated with respect to the ramp trajectory, designed in chapter 4. Only the part of the trajectory where the velocity command is positive is utilized in the evaluation. The ramp trajectory provides a step in the velocity command and it is therefore observed in the following that the tracking performance is decreased compared to tracking the quintic trajectory. This is a consequence of the low bandwidth in the closed loop system. The results of the simulated response are given in figure 7.8.

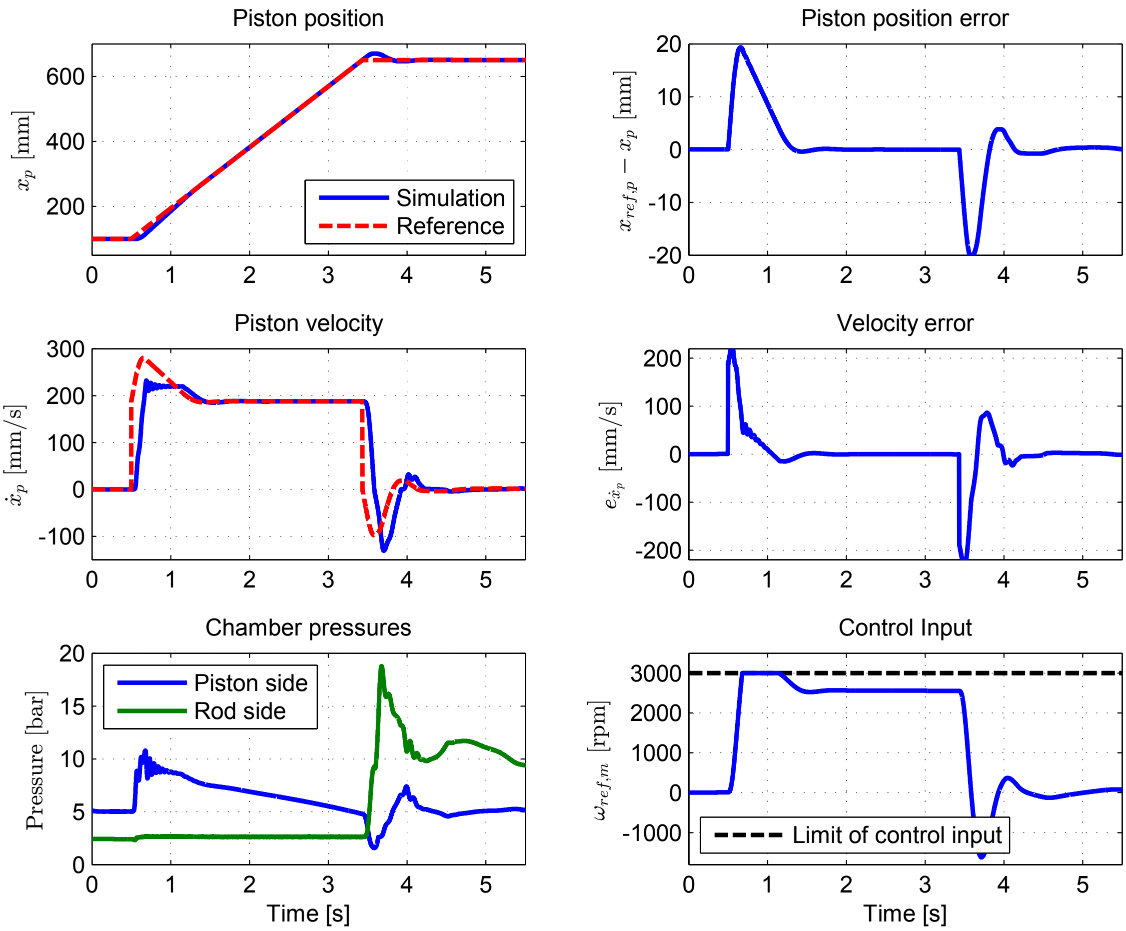

Figure 7.8. Simulation of the system controlled by the controllers designed for positive velocity. The ramp trajectory is applied as reference.

In figure 7.8, it is seen that the tracking performance is poor, compared to tracking of the quintic trajectory. This is due to saturation of the control signal and the low bandwidth of the system. The saturation results in windup of the integrator (in the velocity controller), which is accommodated by the anti windup system described previously. Despite this, the saturation results in momentarily high velocity errors, as the control system cannot track velocity steps. The rms velocity error is 47.5 mm/s, whilst the rms position error is 5.57 mm.

The decreased performance, caused by saturation of the control input, can not be avoided as the necessary flow rate, to track the reference, is not available. It is therefore assessed that the achievable tracking performance is reached. The controllers designed throughout this section are therefore implemented and tested in the physical setup. The results are presented and discussed in chapter 8. Prior to this, controllers are designed for negative velocity in the following section.

7.2 Controller Design for Negative Velocity

In this section, controllers (realizable in the available test setup) are designed for the case where the piston velocity is negative. This means controllers are designed for the system $\mathbf{G_s^-}$. Initially, it is investigated how the decentralized control structure should look like for the system $\mathbf{G_s^-}$. This investigation is only relevant for the system description at negative piston velocity, as the pressure can not be controlled at positive velocities, reducing G_s^+ to a SISO system as shown in section 5.5. After determining a decentralized control structure for the MIMO system $\mathbf{G_s^-}$, the system is treated as two SISO systems, where controllers are designed for controlling the piston velocity and the piston side pressure.

7.2.1 Overview of Control Structure

An overview of the couplings in the system, is provided in figure 7.9, showing that each input is connected to both outputs.

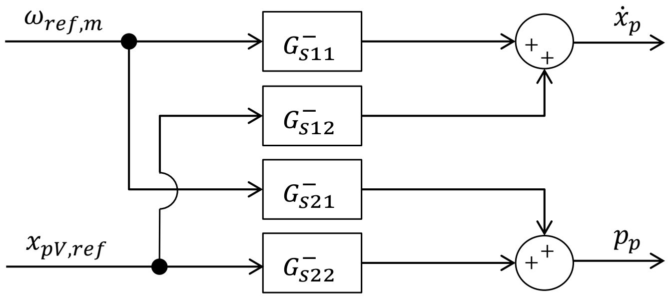

Figure 7.9. Block diagram of the MIMO system at negative velocity.

To treat the system as two SISO systems, an analysis of the relative gain array is carried out in the following. This is performed to determined a suitable input-output pairing, based on the level of interaction in the system.

Analysis of the Relative Gain Array

Initial analysis of the MIMO system is carried out by calculating the relative gain array (RGA) of the transfer matrices. This measure is used to quantify the level of interaction in the system. (Skogestad and Postlethwaite, 2001) The relative gain array is calculated using equation (7.5), where $\circ$ denotes the element wise product.

$$\Lambda\left(i\omega\right) = \mathbf{G}\left(i\omega\right) \circ \left(\mathbf{G}\left(i\omega\right)^{-1}\right)^T \tag{7.5}$$

As seen in equation (7.5), the RGA number depends on the frequency at which it is evaluated. In equation (7.6), the transfer matrix is evaluated at $s = 0$, yielding the DC-gain of the four entries. Furthermore, the RGA is evaluated from $\mathbf{G_s^-}(0)$, to quantify the level of interaction in the system at steady state.

$$\mathbf{G_s^-}(0) = \begin{bmatrix} 0.75\text{e-3} & 134.40\text{e-3} \\ -26.31\text{e3} & -135.27\text{e6} \end{bmatrix} \qquad \Lambda_s^-(0) = \begin{bmatrix} 1.036 & -0.036 \\ -0.036 & 1.036 \end{bmatrix} \tag{7.6}$$

From the steady state RGA, given in equation (7.6), it is clear that the DC-coupling is strongest in a diagonal pairing of the input-output. This suggests that the output $\dot{x}_p$ should be controlled by the input $\omega_{ref,m}$ and the output p_p should be controlled by the input $x_{pV,ref}$. Furthermore it is noted that the off-diagonal DC-coupling is negative and relatively weak. Negative DC-couplings should be avoided, when pairing the input-output, as it potentially can cause instability of the system. This occurs if sub-controllers are designed with integral action (Skogestad and Postlethwaite, 2001). A weak coupling means that changes, in for example the input $x_{pV,ref}$, has little influence on the output $\dot{x}_p$, compared to changes in the input $\omega_{ref,m}$.

As mentioned, the RGA depends on the frequency used in the evaluation. A frequency sweep is therefore performed to test the level of interaction in the system at different frequencies. To illustrate the diagonal dominance, the RGA-number is calculated from equation (7.7) (Skogestad and Postlethwaite, 2001) and illustrated in figure 7.10.

$$\text{RGA-number} = \left\|\Lambda(\mathbf{G_s^-}) - \mathbf{I}\right\|_{\text{sum}} \tag{7.7}$$

For decentralized control, pairings are preferred such that the RGA-number is close to zero. This means that the respective diagonal is dominating. The RGA-number is illustrated as a function of frequency in figure 7.10, where the blue line is obtained from diagonal input-output pairing and the green line from off-diagonal pairing.

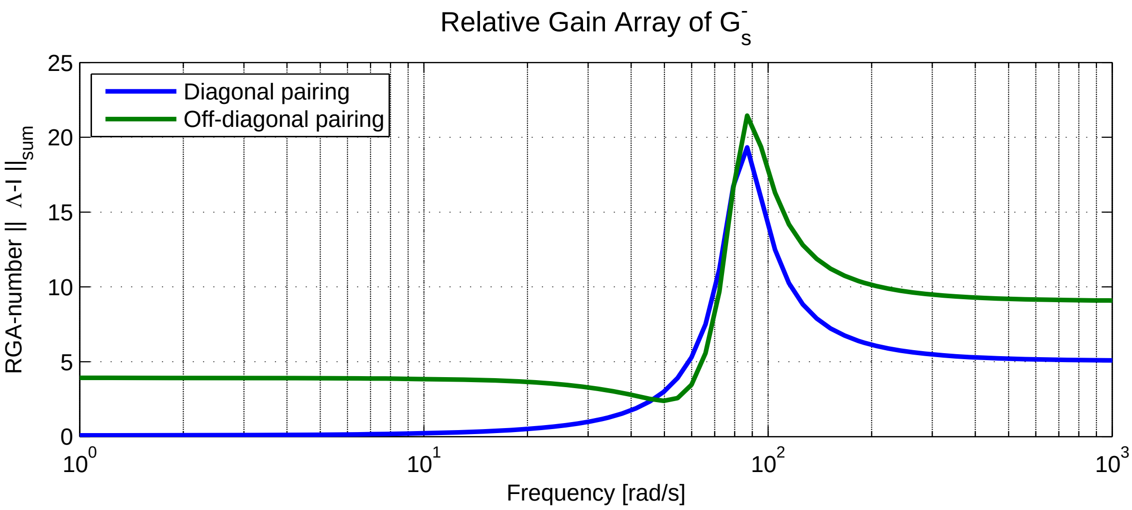

Figure 7.10. Frequency sweep of the RGA-number, with respect to input-output pairing combinations of the transfer matrix $\mathbf{G_s^-}$.

From figure 7.10, it is clear that a diagonal input-output pairing results in the lowest RGA-number throughout most of the frequency spectrum. Around the eigenfrequency of the system, the RGA-number increases dramatically. This is a consequence of large imaginary terms, obtained when evaluating the transfer matrix $\mathbf{G_s^-}$.

In this control problem, the frequencies below the eigenfrequency of the system are of interest. The eigenfrequency of the system is considered the limit of achievable performance, due to the poor damping resulting in a high resonance peak. In the low frequency range (below the eigenfrequency at 84 rad/s), it is clear that a diagonal pairing is preferred, as the RGA-number is closest to zero. In the frequency range 50-80 rad/s it is noted that the RGA-number obtained with an off-diagonal pairing, is lower than the RGA-number obtained with a diagonal pairing. This suggests that an off-diagonal pairing should be preferred in this frequency range. When taking the DC-coupling into consideration, this is not the case though. In equation (7.6), it was shown that the off-diagonal DC-gain is negative, which should be avoided, as it potentially can cause instability of the system, if sub-controllers are designed with integral action (Skogestad and Postlethwaite, 2001). It is assessed, from this RGA analysis, that the off-diagonal coupling can be disregarded and the system can be considered as two SISO systems, using a diagonal pairing of the input-output.

Based on the observations and the argumentation given above, the decentralized control structure is obtained from a diagonal input-output pairing, which is presented in the following.

Decentralized Control Structure

The decentralized control structure is illustrated in figure 7.11, where it is given as two SISO systems. The controller G_{vc}^{-} is designed for controlling the piston velocity, while G_{ppc}^{-} is designed for controlling the piston side pressure. The plants G_{s11}^{-} and G_{s22}^{-} are obtained from the simplified linear system, given in equation (5.27) on page 60.

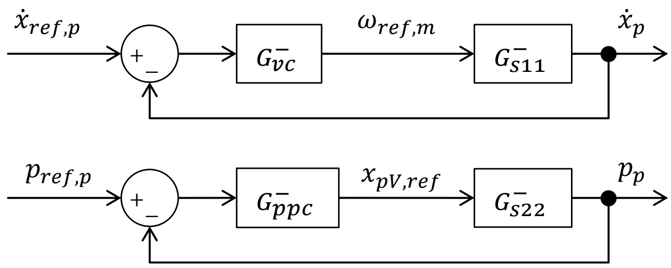

Figure 7.11. Block diagram of the decentralized control structure at negative velocity.

The velocity plant G_{s11}^{-} is repeated in equation (7.8), while the plant describing the pressure dynamic, G_{s22}^{-}, is repeated in equation (7.9).

$$\frac{\dot{x}_p}{\omega_{ref,m}} = \underbrace{\frac{5.05}{(s^2 + 23.14s + 7085)}}_{G_{s11}^{-}} \tag{7.8}$$

$$\frac{p_p}{x_{pV,ref}} = \underbrace{\frac{-7.1e7(s^2 + 22.3s + 3062)}{(s^2 + 23.14s + 7085)(s + 0.23)}}_{G_{s22}^{-}} \tag{7.9}$$

The Bode diagrams of the two transfer functions are given in figure 7.12 on the next page. The frequency response of the velocity plant is given to the left and the response of the pressure dynamic to the right. Note the different scaling of the two graphs. The plant

G^-_{s11} has the input unit rad/s and output unit m/s. The plant G^-_{s22} has no input unit (relative spool position of the valve) and output unit is Pa.

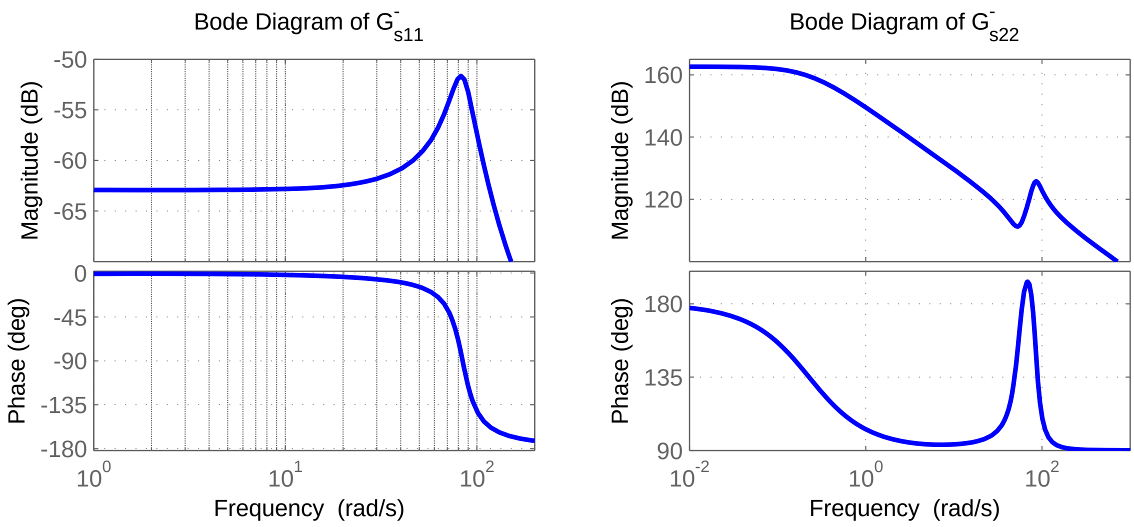

Figure 7.12. Left: Bode diagram of G^-_{s11} - transfer function from $\omega_{ref,m}$ to $\dot{x}_p$. Right: Bode diagram of G^-_{s22} - transfer function from $x_{pV,ref}$ to p_p.

In figure 7.12, it is evident that the resonance peak in G^-_{s11}, around the eigenfrequency 84.2 rad/s, is approximately 13 dB, due to low damping of the system. Furthermore, it is noted that G^-_{s11} is a type 0 system, which results in a steady state velocity error at step inputs, if the system is simply controlled by a proportional controller.

From figure 7.12, it is noted that the phase of the pressure dynamic G^-_{s22} starts at 180° due to the negative gain of the transfer function. This property is taken into account later, when the pressure controller is designed. The characteristics of G^-_{s22} is caused by a pole placed at 0.23 rad/s, two complex conjugated zeros at 55.3 rad/s and two complex conjugated poles at 84.2 rad/s. With respect to controlling the pressure, this limits the achievable bandwidth as discussed when the pressure controller is designed.

In the following, the pressure controller is initially designed. This is followed by a design of the velocity controller. Finally a position controller is designed for evaluation purposes.

7.2.2 Pressure Controller

The pressure controller is designed based on the considerations given below:

- The input to the plant G^-_{s22} is a relative spool position. As the PDV is a two-way valve, the control input needs to be a value between zero and one. To accommodate this a negative gain is required in the controller G^-_{ppc}.

- The pressure buildup, in the two chambers, is caused by an imbalance between the flow rates and the piston area ratio. The pressure level therefore depends on the system controlling the velocity. Similarly, the velocity dynamic changes with the pressure level, making the two outputs coupled. To avoid complications related to opposing control demands, it is assessed that one of the control loops needs to be faster than the other.

- The primary target is a good velocity control. In this context it is therefore decided to prioritize the bandwidth of the velocity loop. Later, it is shown that a bandwidth of 34.77 rad/s is obtained in the velocity control at negative velocity. The pressure controller is therefore designed with a crossover frequency approximately five times lower than the bandwidth of the velocity loop.

- A steady state error is acceptable, as it is not crucial, that the piston side pressure is exactly 25 bar. An integrator can therefore be omitted in the control structure.

Based on the considerations listed above, it is sufficient to control the piston side pressure with a proportional gain. The pressure controller G^{-}_{ppc} is given in equation (7.10). The magnitude of the gain is determined such that the resonance peak is suppressed by 8 dB, to ensure that the system does not go into resonance.

$$G^{-}_{ppc} = -2 \cdot 10^{-7} \tag{7.10}$$

The Bode diagram of the open loop system is given to the left in figure 7.13, showing a crossover frequency at 6.1 rad/s, which is 5.7 times lower than the bandwidth of the velocity loop. The closed loop step response is given to the right.

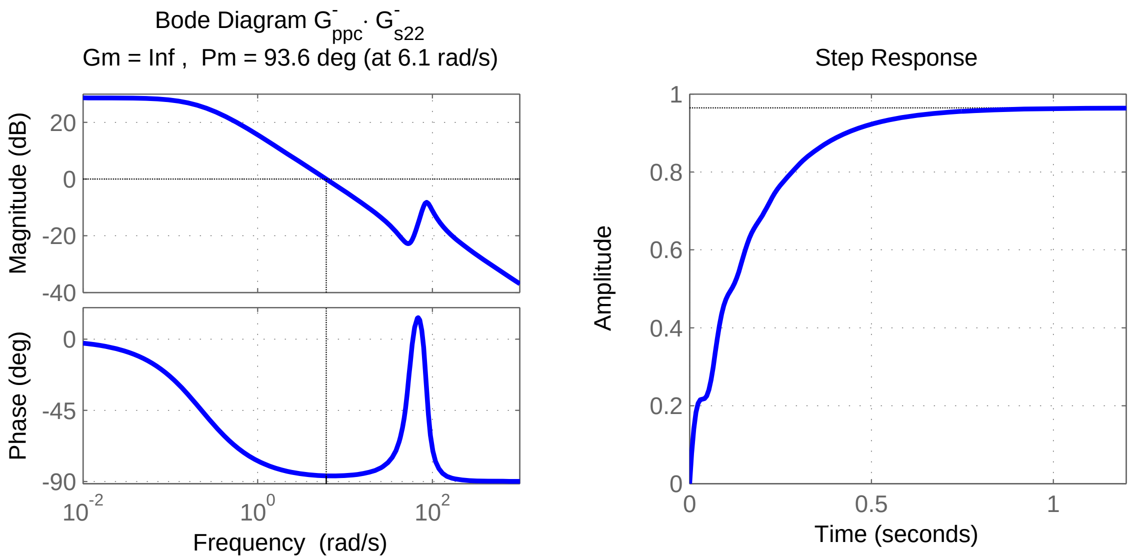

Figure 7.13. Left: Open loop Bode diagram of $G^{-}_{ppc} \cdot G^{-}_{s22}$. Right: Step response of closed pressure loop.

The step response reveals an acceptable steady state error of 3.6 %. The bandwidth of the pressure loop is 6.2 rad/s, which is assessed sufficient as a relatively large error margin can be accepted if a good velocity response is obtained. In the following, the velocity controller is designed.

7.2.3 Velocity Controller

The velocity controller G_{vc}^{-}, is designed from the same criteria as the velocity controller at positive velocities. The criteria was listed in subsection 7.1.1 on page 65. An integrator is included to obtain a type 1 system, removing the steady state error at step inputs. Furthermore a second order input filter is placed 20 rad/s below the eigenfrequency, to suppress the resonance peak and filter the control input. The gain is hereafter raised until a 10 dB gain margin is reached. The resulting velocity controller is given in equation (7.11).

$$G_{vc}^{-} = \frac{96.26 \cdot 10^6}{s \cdot (s+64)^2} \tag{7.11}$$

The open loop Bode diagram is given to the left in figure 7.14, showing a gain margin of 10 dB and a phase margin of 58.2°. These both meet the design criteria listed in subsection 7.1.1 on page 65. To the right in figure 7.14, the closed loop step response is given. The step response reveals an overshoot of 8 %, which meets the criteria of an overshoot < 10 %.

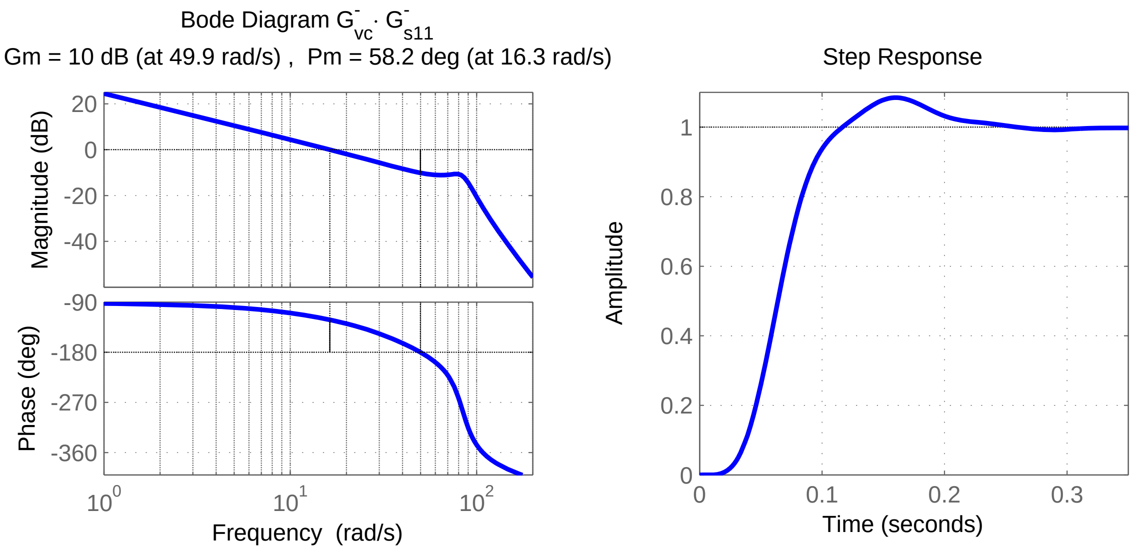

Figure 7.14. Left: Open loop Bode diagram of $G_{vc}^{-} \cdot G_{s11}^{-}$. Right: Step response of closed velocity loop.

A bandwidth of 34.77 rad/s is obtained in the velocity control, which is approximately 5.5 Hz. This is a 46 % increase, compared to the achieved bandwidth at positive velocities (BW = 3 Hz). Due to the higher bandwidth, the performance is expected to be increased, compared to the controlling the system at positive velocities.

As previously, an outer position loop is introduced to evaluated the tracking performance, by applying the trajectories presented in chapter 4 as reference.

7.2.4 Position Controller

A blockdiagram of the position control system is provided in figure 7.15 on the following page.

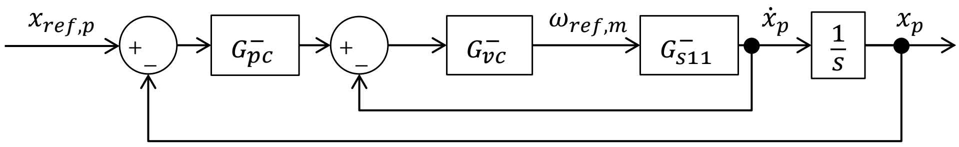

Figure 7.15. Blockdiagram of position control system.

The plant G_p^-, for which the position controller G_{pc}^- is designed for, is given by equation (7.12).

$$G_p^- = \frac{G_{vc}^- \cdot G_{s11}^-}{1 + G_{vc}^- \cdot G_{s11}^-} \cdot \frac{1}{s} \tag{7.12}$$

As for positive velocities, it is sufficient to control the position with a proportional gain, due to the free integrator present in the plant G_p^-. The gain is determined such that a 10 dB gain margin is obtained. The controller is given in equation (7.13).

$$G_{pc}^- = 7.5 \tag{7.13}$$

The resulting open loop Bode diagram is given in figure 7.16, showing a gain margin of 10 dB and a phase margin of 63.4°. These both meet the design criteria listed in subsection 7.1.1 on page 65. To the right in figure 7.16, the closed loop step response is given. The response reveals an overshoot of 3 %, which is assessed acceptable. The bandwidth of the position control is 17.34 rad/s, which is half the bandwidth of the velocity loop.

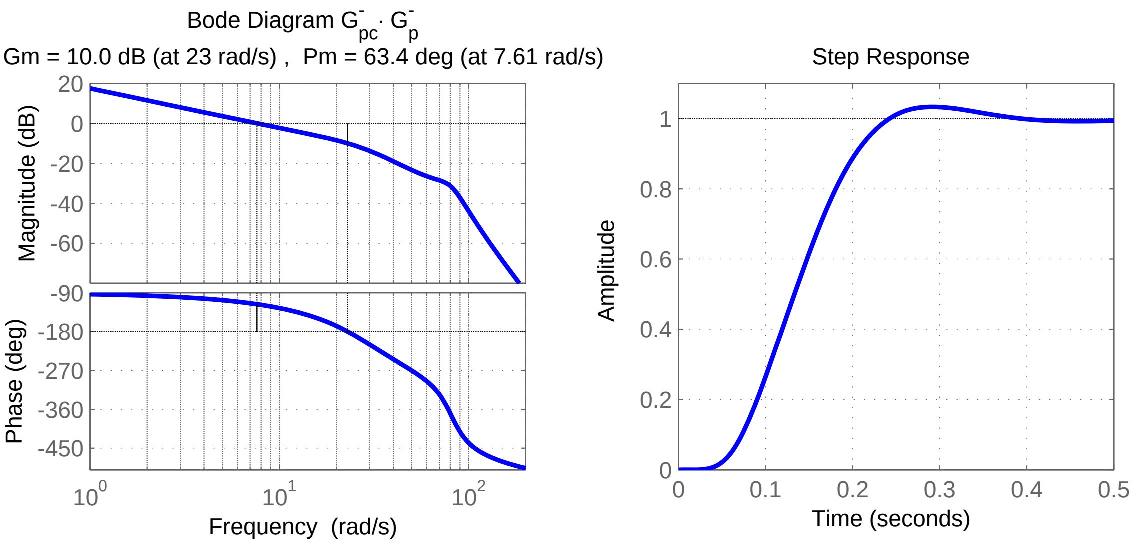

Figure 7.16. Left: Open loop Bode diagram of $G_{pc}^- \cdot G_p^-$. Right: Step response of closed position loop.

As previously, the controllers are implemented and tested in the simulation model. Feedforward of the velocity reference is included, along with anti windup of the integrator in the velocity controller G_{vc}^-. The results are presented in the following section.

7.2.5 Simulation of Control System at Negative Velocity

The simulations are carried out using parts of the two trajectory types, presented in chapter 4, where the velocity references are negative. In figure 7.17, a simulation is given, where the quintic trajectory is applied as reference to the system. From the simulation, it is clear that the increased bandwidth in both the position- and velocity loop, has increased the tracking performance of the system compared to the performance obtained at positive velocities. The rms position error is 0.97 mm and the rms velocity error is 8.00 mm/s. The performance is assessed to be acceptable considering the assumptions made throughout the designed process. A MIMO system is represented by two SISO systems, linear controllers are designed for a nonlinear system, the servo drive- and valve dynamics are neglected. Furthermore, during tracking of the trajectories, significant parameter variations occur in the system. The control system is therefore considered robust towards disturbances, parameter variations and uncertainties. The performance obtained during physical tests are presented in chapter 8.

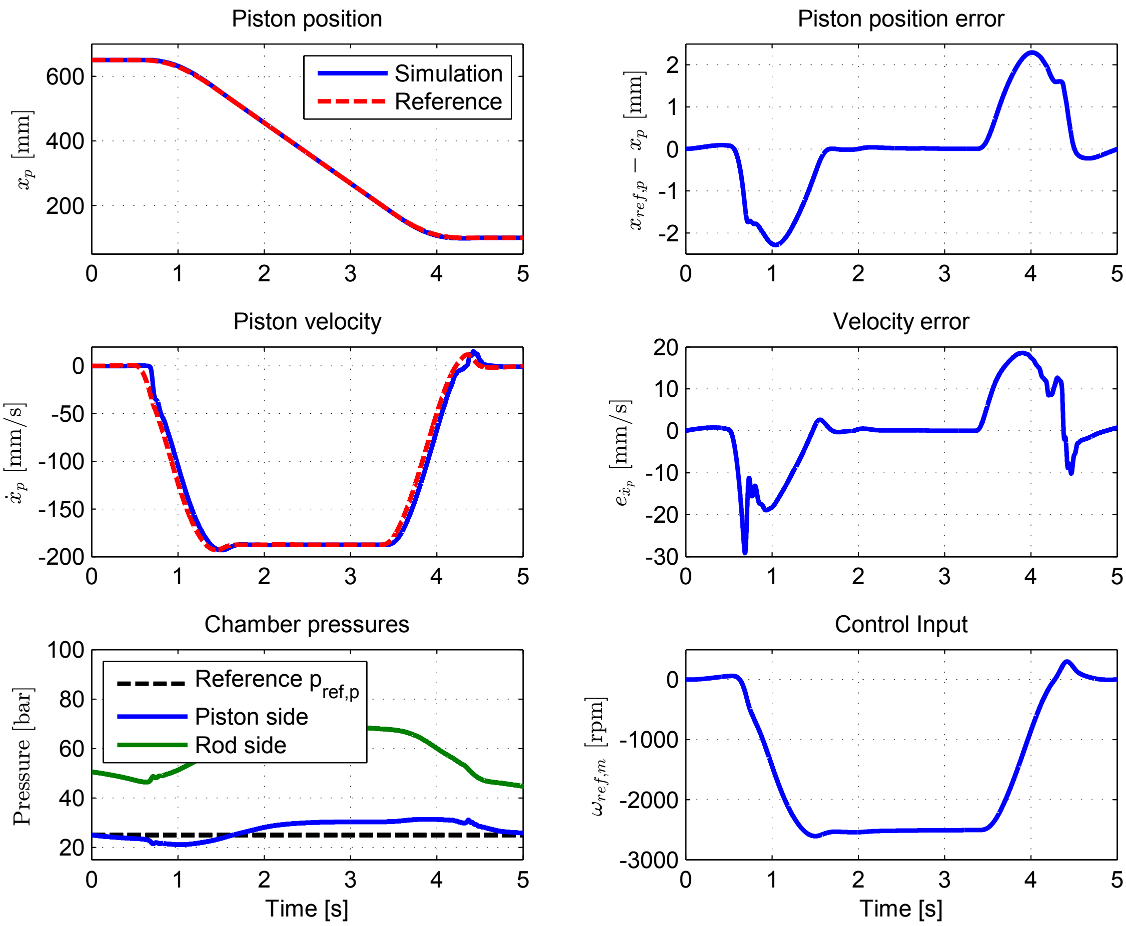

Figure 7.17. Simulation of the system controlled by the controllers designed for negative velocity. The quintic trajectory is applied as reference.

In figure 7.17, the chamber pressures obtained during simulation are given as well. Here it is seen that the piston side pressure is held in the vicinity of the reference at 25 bar. The rms pressure error is 3.73 bar, which is expected due to the low bandwidth of the closed pressure loop and the controller design making the open loop system type 0. This results in a steady state error, which also is reflected in the rms error. The maximum pressure error is 8 bar, which can be accepted as a pressure level of exactly 25 bar, is not crucial. The important thing is to maintain a relatively stiff system (high bulk modulus), with an acceptable pressure level.

Furthermore, the control input $\omega_{ref,m}$ should be noted from figure 7.17. The control input is continuous and never saturated, meaning that the anti windup system is inactive.

In figure 7.18, the control system is simulated with the ramp trajectory applied as input reference. Here, the the control input $\omega_{ref,m}$, is saturated and the anti windup system is active. The saturation of control input results in a decreased tracking performance. The rms position error is 2.46 mm and the rms velocity error is 34.59 mm/s. The position- and velocity errors occur during the transient periods, as a result of the low bandwidth in the closed loop system. At steady state, both errors are zero. Considering the pressure control, this is not the case. The rms pressure error is 3.83 bar and there is always a steady state error, as the open pressure loop is a type 0 system.

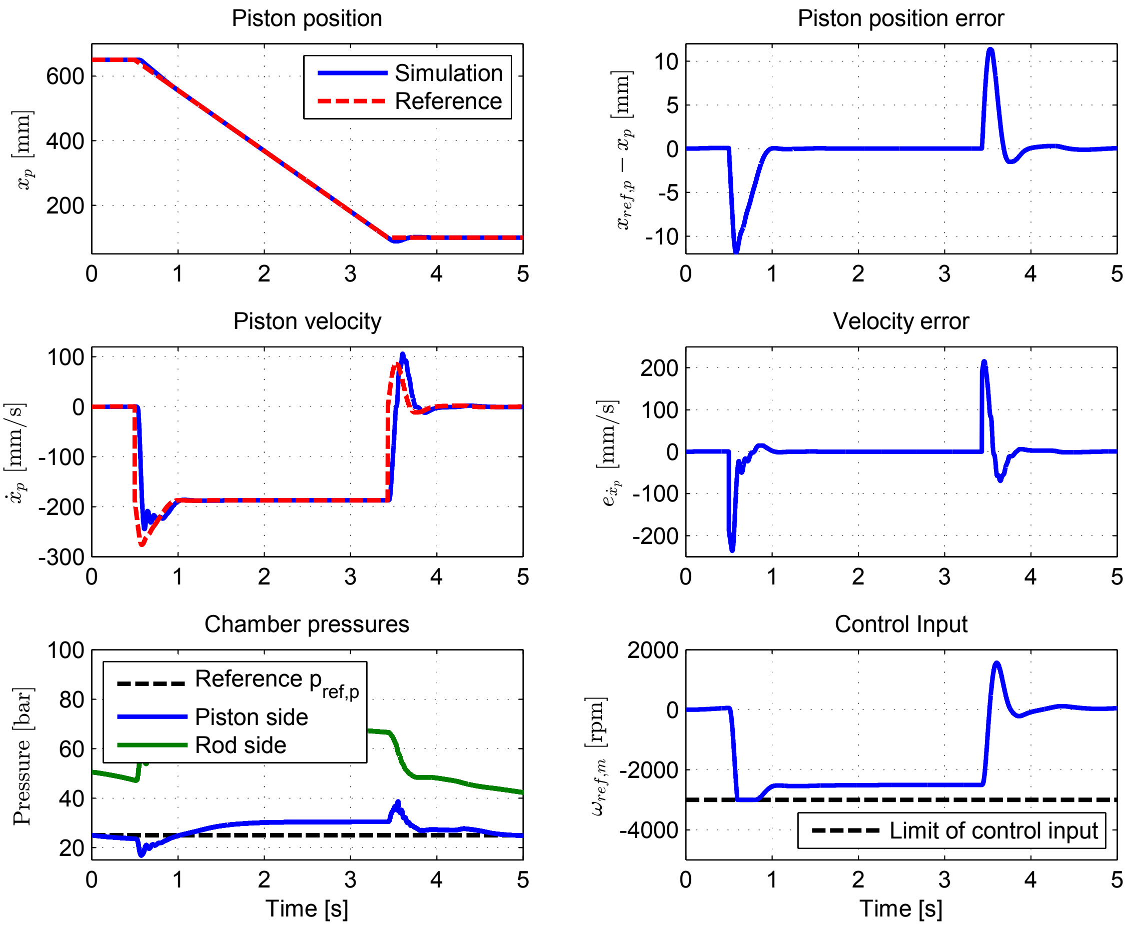

Figure 7.18. Simulation of the system controlled by the controllers designed for negative velocity. The ramp trajectory is applied as reference.

Throughout the evaluation of the controller designs, is it evident that low bandwidth of the control system, limits the tracking performance. This was necessary, to obtain a set of controllers that can successfully be tested in the laboratory. In the following section, controllers are designed for the purpose of high tracking performance. These controllers can not be tested in the physical test setup, due to limitations in the velocity estimate that is utilized as feedback. The controllers, designed in the following, are therefore only evaluated from simulations, but can be applied to the system if the setup is changed such that a good velocity estimate is available as feedback.

7.3 High Performance Controller Design with Active Damping

Active damping is introduced to increase the tracking performance of the system. Active damping means that a "leakage flow" is injected into the system, using a feedback of the *virtual* load pressure through a gain. Thereby fictive leakage flow is "injected" in the system, to increase the leakage coefficients and achieve increased damping of the system. If the virtual load pressure is fed back through a high pass filter, the active damping does not influence the DC-gain of the system. In this section, an estimation of the leakage coefficient is derived, followed by designs of controllers for positive and negative velocity.

7.3.1 Estimation of active damping coefficient

To estimate the active damping coefficient C_L (shown in figure 7.19 on the following page), which is introduced to increase the damping of the system, a simplified system is derived in the following. The original system from equations (5.1), (5.5) and (5.6) on page 45, are expressed in terms of a virtual load pressure p_L. This substitution yields a system with two states, where an analytical transfer function from the input $\omega_{ref,m}$ to the output $\dot{x}_p$, can be obtained. From the analytical expression of the transfer function, the active damping coefficient C_L can be determined, such that a desirable damping ratio is obtained. When C_L is estimated, the effect is checked in the original system.

The virtual load pressure is defined in equation (7.14), where the piston area ratio is given by $\alpha = A_r/A_p$. Substituting equation (7.14) into the force balance from equation (5.1) on page 44, yields the rewritten force balance in equation (7.15).

$$p_L = p_p - \alpha \cdot p_r \tag{7.14}$$

$$\Downarrow$$

$$\Delta\ddot{x}_p \cdot M_{eq0} = A_p \cdot \Delta p_L - B_v \cdot \Delta\dot{x}_p \tag{7.15}$$

The gradient of the virtual load pressure is given by $\dot{p}_L = \dot{p}_p - \alpha \cdot \dot{p}_r$. To find $\dot{p}_L$ the pressure gradients of the chamber pressures, from equations (5.5) and (5.6) on page 45, are simplified such that they can be subtracted and collected in terms of the variables ω_m and $\dot{x}_p$. In equation (7.16) the change in the piston side pressure gradient is simplified by assuming that the leakage flow of the chamber is zero. This is necessary to obtain an expression for the gradient of the virtual load pressure, that is independent of the chamber pressures. Furthermore, the valve flow is assumed to be zero, as it is the transfer function from $\omega_{ref,m}$ to $\dot{x}_p$ that is of interest.

$$\Delta\dot{p}_p = \frac{\beta_{p0}}{V_{p0}} \cdot (K_{qpP\omega} \cdot \Delta\omega_m - K_{pleak} \cdot \Delta p_p - K_{qp} \cdot \Delta x_{pV} - A_p \cdot \Delta\dot{x}_p)$$

$$\Downarrow \text{Simplify assuming } K_{pleak} = 0 \text{ and } x_{pV} = 0$$

$$\Delta\dot{p}_p = \frac{\beta_{p0}}{V_{p0}} \cdot (K_{qpP\omega} \cdot \Delta\omega_m - A_p \cdot \Delta\dot{x}_p) \tag{7.16}$$

The same procedure is applied to the rod side pressure gradient from equation (5.6) on page 45. This is shown in equation (7.17), where the rod side area is substituted by $A_r = \alpha \cdot A_p$. Furthermore, the rod side pump flow is expressed in terms of the piston side pump, using the pump ratio δ, given in equation (3.2) on page 23. This yields the substitution $K_{qrP\omega} = \delta \cdot K_{qpP\omega}$.

$$\Delta\dot{p}_r = \frac{\beta_{r0}}{V_{r0}} \cdot (-K_{qrP\omega} \cdot \Delta\omega_m - K_{rleak} \cdot \Delta p_r + A_r \cdot \Delta\dot{x}_p)$$

$$\Downarrow \text{Simplify assuming } K_{rleak} = 0 \text{ , } A_r = \alpha \cdot A_p \text{ and } K_{qrP\omega} = \delta \cdot K_{qpP\omega}$$

$$\Delta\dot{p}_r = \frac{\beta_{r0}}{V_{r0}} \cdot (-\delta \cdot K_{qpP\omega} \cdot \Delta\omega_m + \alpha \cdot A_p \cdot \Delta\dot{x}_p) \tag{7.17}$$

To collect the terms in $\dot{p}_p$ and $\dot{p}_r$, such that $\dot{p}_L$ can be obtained, it is assumed that the pump ratio δ equals the area ratio α. Substituting the chamber pressure gradients into $\dot{p}_L = \dot{p}_p - \alpha \cdot \dot{p}_r$, yields the virtual load pressure gradient in equation (7.18).

$$\Delta\dot{p}_L = \dot{p}_p - \alpha \cdot \dot{p}_r = \left(\frac{\beta_{p0}}{V_{p0}} + \frac{\beta_{r0} \cdot \alpha^2}{V_{r0}}\right) \cdot (K_{qpP\omega} \cdot \Delta\omega_m - A_p \cdot \Delta\dot{x}_p) \tag{7.18}$$

Introducing the active damping coefficient, C_L, yields the virtual load pressure gradient in equation (7.19), where the coefficient Φ is also introduced.

$$\Delta\dot{p}_L = \underbrace{\left(\frac{\beta_{p0}}{V_{p0}} + \frac{\beta_{r0} \cdot \alpha^2}{V_{r0}}\right)}_{\Phi} \cdot (K_{qpP\omega} \cdot \Delta\omega_m - A_p \cdot \Delta\dot{x}_p - C_L \cdot \Delta p_L) \tag{7.19}$$

The system equations (7.15) and (7.19) are Laplace transformed, assuming zero initial conditions. The block diagram of the system is given in figure 7.19, where it is illustrated how the virtual load pressure is fed back.

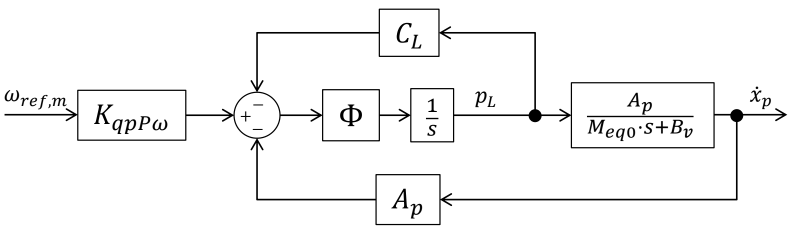

Figure 7.19. Block diagram of simplified system, with feedback of the virtual load pressure though the damping coefficient C_L.

The simplified analytical transfer function from the input $\omega_{ref,m}$ to the output $\dot{x}_p$, is given in equation (7.20).

$$\frac{\dot{x}_p}{\omega_{ref,m}} = \frac{\frac{\Phi}{M_{eq0}} \cdot A_p \cdot K_{qpP\omega}}{s^2 + \left(\frac{B_v}{M_{eq0}} + \Phi \cdot C_L\right) \cdot s + \frac{\Phi}{M_{eq0}} \cdot \left(C_L \cdot B_v + A_p^2\right)} \tag{7.20}$$

From the analytical transfer function in equation (7.20), the gain, natural frequency and damping ratio of the system, is obtained. These are given as:

$$K = \frac{K_{qpP\omega} \cdot A_p}{C_L \cdot B_v + A_p^2} \tag{7.21}$$

$$\omega_n = \sqrt{\frac{\Phi}{M_{eq0}} \cdot \left(C_L \cdot B_v + A_p^2\right)} \tag{7.22}$$

$$\zeta = \frac{\frac{B_v}{M_{eq0}} + \Phi \cdot C_L}{2 \cdot \sqrt{\frac{\Phi}{M_{eq0}} \cdot \left(C_L \cdot B_v + A_p^2\right)}} \tag{7.23}$$

In the following, the analytical result is examined at the critical operation points for positive- and negative velocity. This is utilized to determined the size C_L, such that a desirable damping ratio is obtained. In the introduction to this section, it was discussed that the virtual load pressure should be fed back though a high pass filter, such that the active damping does not affect DC-gain of the system. Regarding implementation, it would be an advantage if differentiation of the virtual load pressure can be avoided, as noise is present in the measurements. The consequence of implementing C_L as a static gain is therefore also evaluated in the following.

- **Active Damping Coefficient at Positive Velocity**
  Evaluating the transfer function in equation (7.20), at the critical operation point for positive velocity, yield equation (7.24), which is compared to the original transfer function from equation (5.26) on page 58. The natural frequency of the simplified system is 50.7 rad/s, which is the same as the original system. The damping ratio is also the same as the original 0.11.

  $$\frac{\dot{x}_p}{\omega_{ref,m}} = \frac{1.81}{s^2 + 11.35 \cdot s + 2568} \tag{7.24}$$

  It is decided to manipulate the system, such that a damping ratio of $1/\sqrt{2}$ is obtained, as this yields the lowest time constants of a second order system (Philips and Parr, 2011). Solving equation (7.23) equal to $1/\sqrt{2}$, with respect to the damping coefficient, yields $C_L^+ = 1.215 \cdot 10^{-9}$. The superscript + is utilized to indicate that the damping coefficient is obtained for positive velocity.

  To determine the effect of a high pass filter on the virtual load pressure feedback, the DC-gain is evaluated from equation (7.21). With a high pass filter, the DC-gain remains the same as in the original system, which is equal to $703 \cdot 10^{-6}$. Without a high pass filter on the pressure feedback, the DC-gain is $536 \cdot 10^{-6}$. This is a 31% decrease, corresponding to 2.4dB, meaning that the controller gain must be 2.4dB higher, than if it is designed to control the system where high pass filter is included in the pressure feedback. It is assessed that this increase can be accepted, without saturating the control input, and C_L is therefore implemented as a static gain. This assessment also applies for negative velocity, which is examined next.

- **Active Damping Coefficient at Negative Velocity**
  At the critical operation point for negative velocity equation (7.25) is obtained. This is compared to the original transfer function G^-_{s11}, from equation (5.27) on page 60. The natural frequency of the simplified system is 84.2 rad/s, which is the same as the original system. The damping ratio is 0.135 which is almost the same as the original 0.138.

$$\frac{\dot{x}_p}{\omega_{ref,m}} = \frac{4.98}{s^2 + 22.71 \cdot s + 7075} \tag{7.25}$$

  The system is manipulated, such that a damping ratio of $1/\sqrt{2}$ is obtained. This yields a damping coefficient $C_L^- = 727.5 \cdot 10^{-12}$ for negative piston velocity.

When implementing active damping, the system is rearranged such that the pressure feedback yields a flow rate in terms of a shaft revolution. This yields the velocity control problem illustrated in figure 7.20.

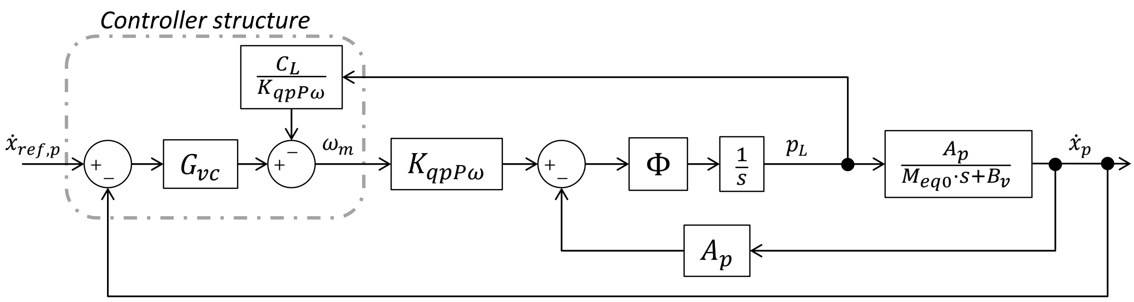

Figure 7.20. Block diagram of the controlled simplified system, with pressure feedback.

In the following subsections, the consequence of active damping is evaluated in the original systems and controllers are designed for controlling the velocity. Furthermore, position controllers are designed to evaluate the performance in the same manner as previously.

7.3.2 Controller Design for Positive Velocity

The Bode diagram of the open loop velocity system, is given in figure 7.21 on the next page. Here the original system is illustrated with- and without active damping. From figure 7.21, it clear that active damping has changed the characteristics, such that higher damping in the system is obtained. The damping ratio is 0.71 and the natural frequency is 58.1 rad/s.

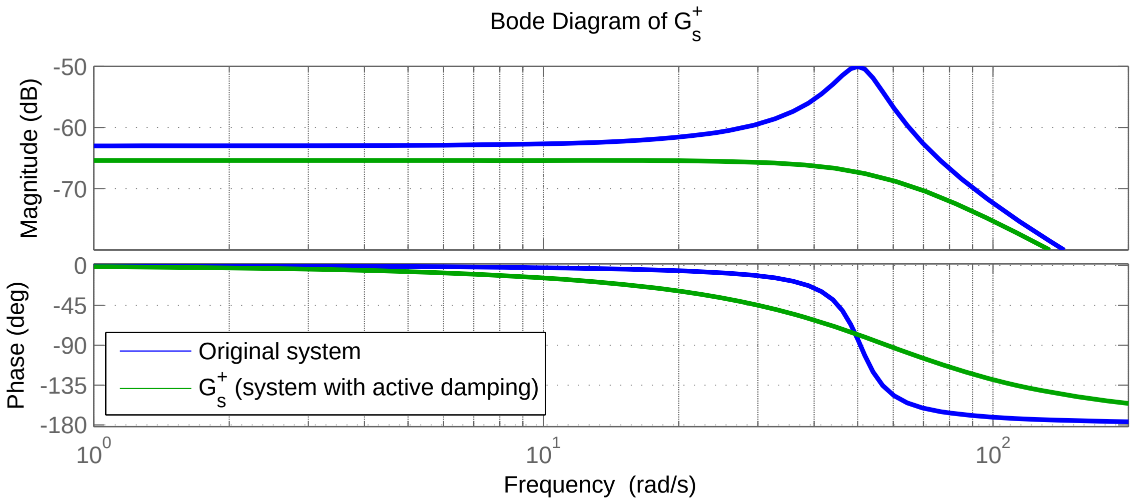

Figure 7.21. Bode diagram of G_s^+ i.e. the transfer function from ω_m to $\dot{x}_p$, with- and without active damping.

As the original 13 dB resonance peak has been suppressed, it is not necessary to low pass filter the control input as previously in section 7.1, where controllers were designed for the system without pressure feedback. A PI-controller is suitable for controlling the system with pressure feedback (green curve in 7.21), as it increases the system type by one and includes high frequency gain. The controller G_{vc}^+, is tuned such that a low rise time-, an overshoot of 10 %- and a phase margin $> 45°$ is obtained. The controller is given in equation (7.26).

$$G_{vc}^+ = \frac{3000 \cdot (s+30)}{s} \tag{7.26}$$

The Bode diagram of the open velocity loop is given to the left in figure 7.22, showing a phase margin of 52.1° at the crossover frequency 68.9 rad/s. The closed loop step response is given to the right.

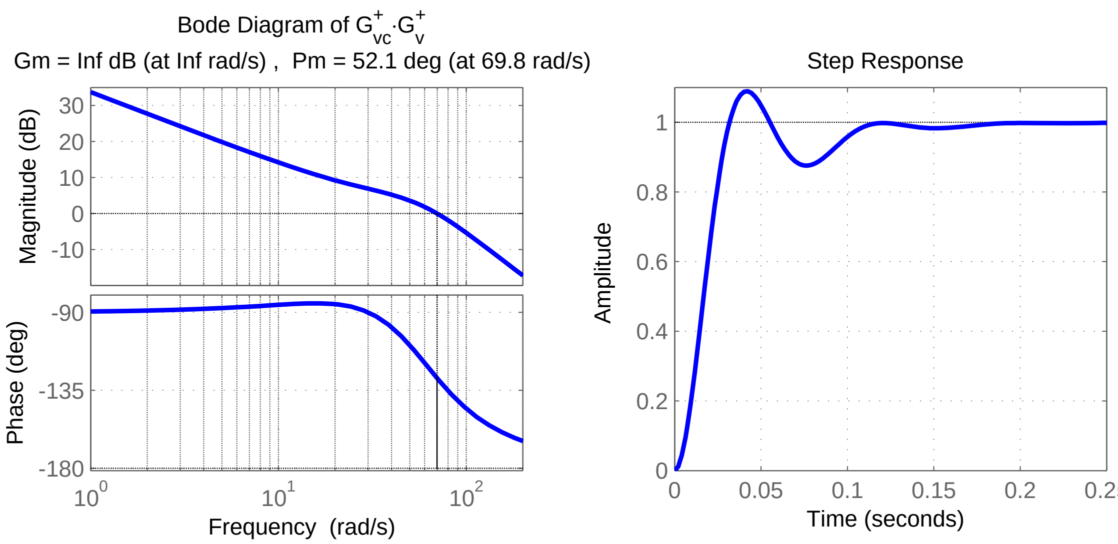

Figure 7.22. Left: Open loop Bode diagram of $G_{vc}^+ \cdot G_v^+$ with active damping. Right: Step response of closed velocity loop.

The bandwidth of the velocity loop is 108.6 rad/s (17.3 Hz), which is a considerable improvement compared to the system without pressure feedback. In subsection 7.1.1 on page 65, it was shown that the obtained closed loop bandwidth is 18.7 rad/s in this case. It is therefore expected that the tracking performance is increased significantly, which is confirmed by simulations shown later.

For evaluation purposes a proportional controller is designed to regulate the position error. The gain is determined such that the crossover frequency of the position loop is 10 times lower than the bandwidth of the velocity loop i.e. 10.9 rad/s. This results in the position controller given in equation (7.27), which result in a closed position loop bandwidth of 13.5 rad/s.

$$G_p^+ = 11.2 \tag{7.27}$$

The controller structure is implemented as previously in sections 7.1 and 7.2, with velocity feedforward and anti windup of the integrator. A simulation with the quintic trajectory as input, is given in figure 7.23.

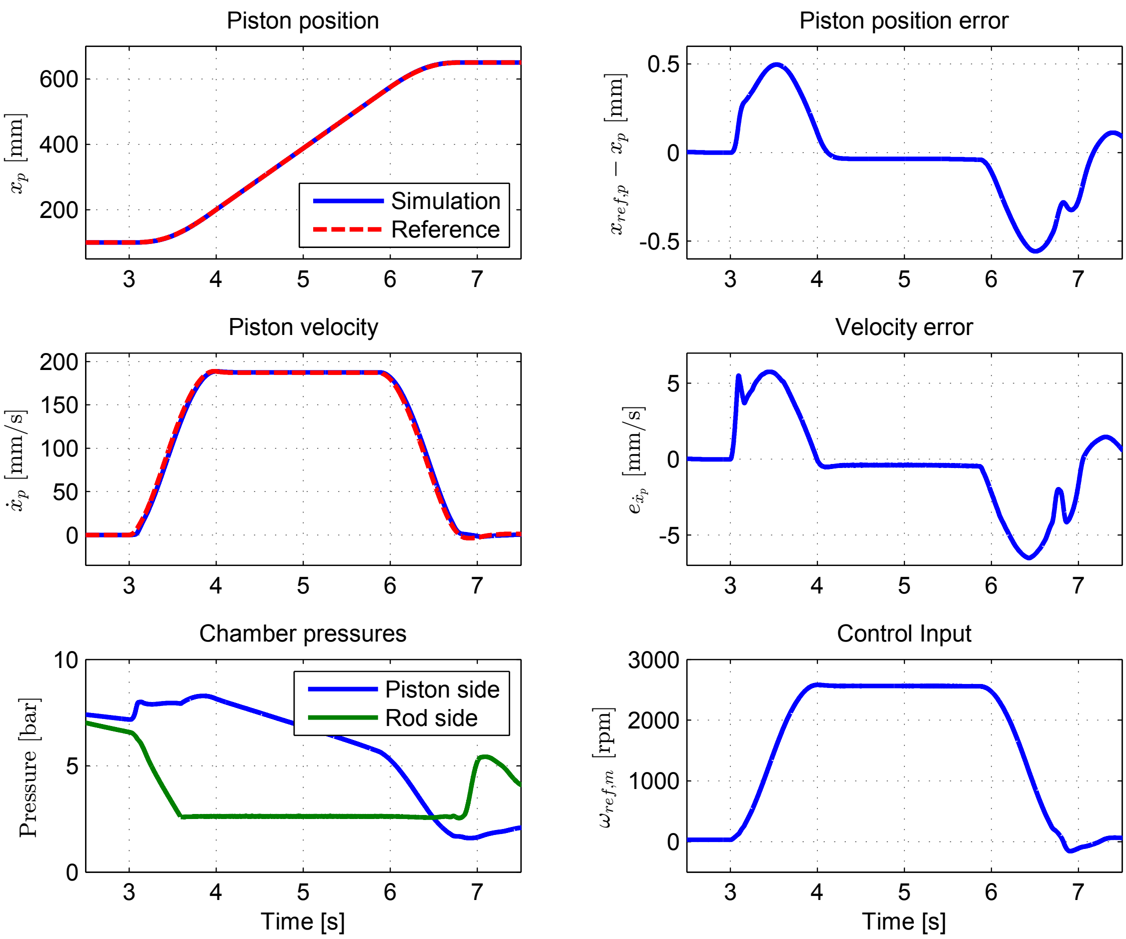

Figure 7.23. Simulation of the system response with pressure feedback in the control structure. The quintic trajectory with positive velocity is applied as reference.

The simulation results in figure 7.23 reveal a significant improvement of the tracking performance, compared to the system without pressure feedback. The rms position error is 0.19 mm, where it previously, in subsection 7.1.3, was 2.68 mm. With pressure feedback, the rms velocity error is 2.45 mm/s, while it previously was 15.44 mm/s. The significant improvement is caused by the increased bandwidth, which is obtained as the damping ratio of the hydro-mechanical system is raised from 0.11 to 0.71.

The active damping adjusts the control input i.e. the pump speed, such that the a “virtual leakage flow” is induced, resulting in greater damping of the system. If the control input is saturated, the pressure feedback does not work and the system characteristics, used in the process of the designing controller, become invalid. The consequences of a saturated control input (inactive pressure feedback) is lower damping of the system, which may lead to instability if not taken into account during controller design.

In figure 7.24 a simulation is given with the ramp trajectory applied as reference. The trajectory requires a step in velocity, which makes the control input saturate. This results in oscillation of the pressure levels and the control input. The oscillations level out and the system responds as intended when the control input reaches a magnitude where it is not saturated and the pressure feedback can influence the input.

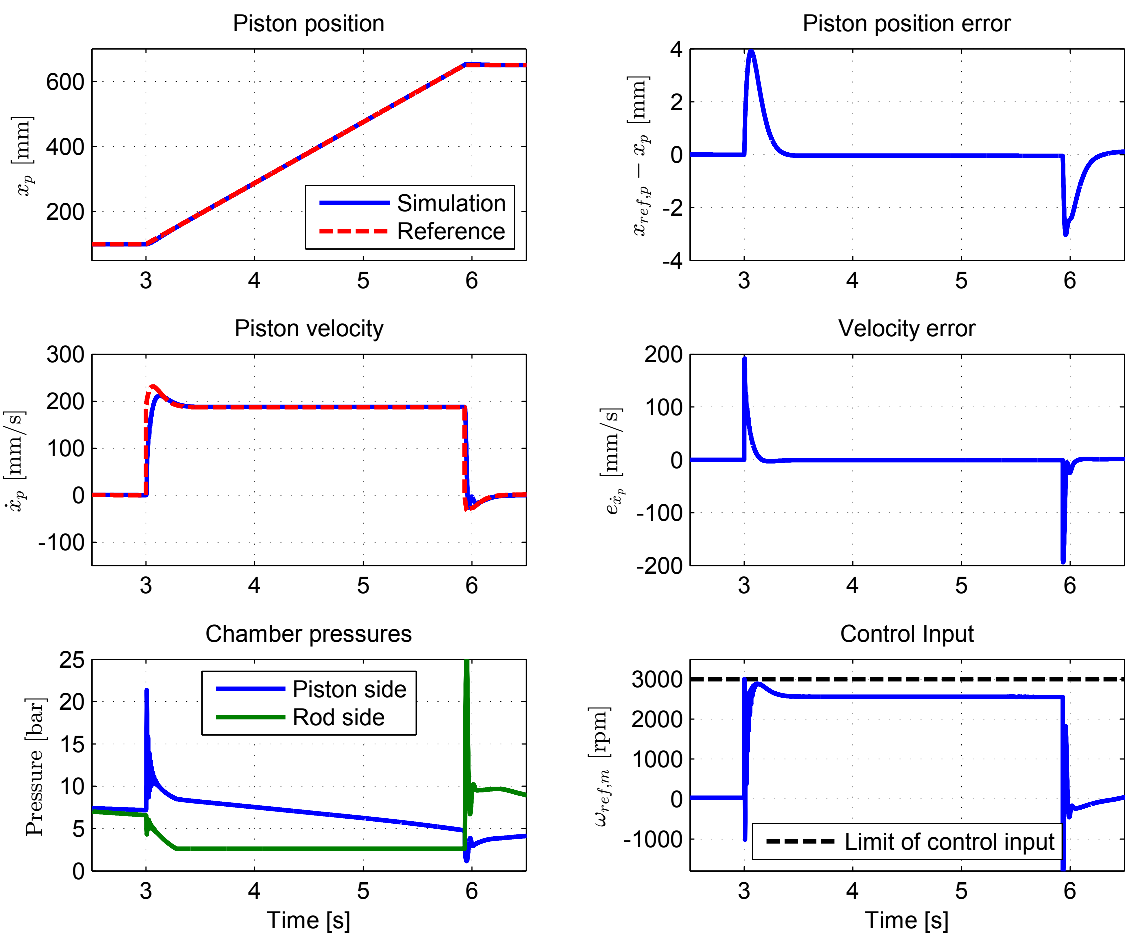

Figure 7.24. Simulation of the system response with pressure feedback in the control structure. The ramp trajectory with positive velocity is applied as reference.

Despite the oscillating behavior of the system, when the control input is saturated, the tracking performance is increased compared to the results in subsection 7.1.3. The rms position error is 0.70 mm and the rms velocity error is 15.18 mm/s.

The ramp trajectory should not be applied in the physical setup, due to the oscillation control signal. This will cause unnecessary stress of the system, as the control strategy does not behave as intended when the control signal is saturated. The same result, with saturation of the control signal, is obtained when applying the ramp trajectory to the control system designed for negative velocity. The controller designs for negative velocity are elaborated in the following.

7.3.3 Controller Design for Negative Velocity

At negative piston velocity, the piston side pressure and the piston velocity need to be controlled. Controller designs are presented in the following for the system where active damping is included. Using pressure feedback a damping ratio of 0.71 is obtained in the velocity plant. The transfer function, describing the relation between the valve input and the piston side pressure, is more complicated due to the presence of two complex conjugated zeros. The Bode diagram of the two transfer functions, for which controllers are designed in the following, are given in figure 7.25. Here, the original transfer function (without active damping), is compared to the "new" system, which is damped by feedback of the virtual load pressure multiplied by the gain C_L^-, determined on page 84.

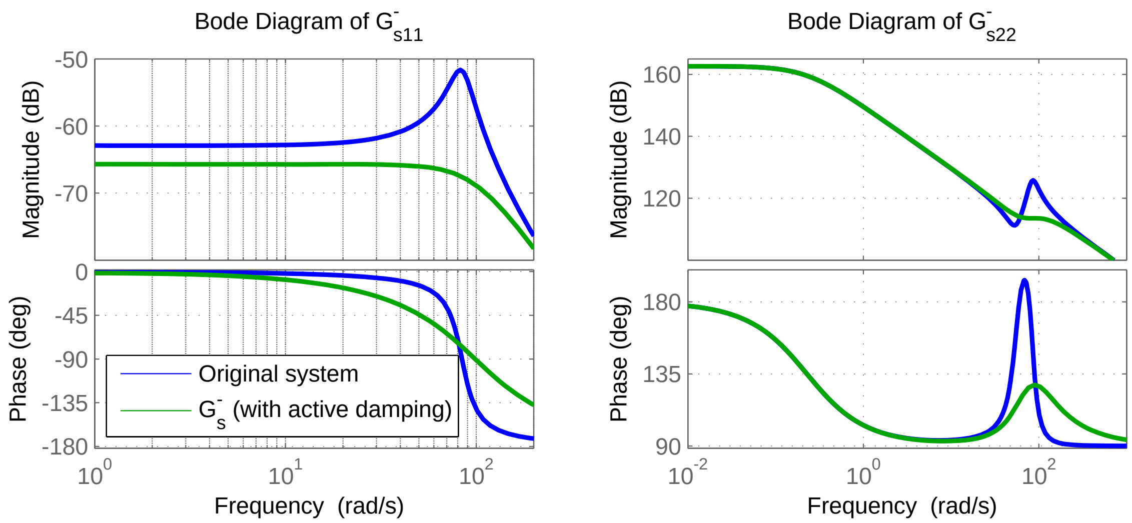

Figure 7.25. Left: Bode diagram of G_{s11}^- - transfer function from $\omega_{ref,m}$ to $\dot{x}_p$. Right: Bode diagram of G_{s22}^- - transfer function from $x_{pV,ref}$ to p_p. Illustrated with- and without active damping.

As the virtual load pressure is fed back though a pure gain, the steady state gain is reduced by 2.4 dB, compared to the original transfer function. Furthermore, the active damping has reduced the resonance peak in both cases, which increases the achievable bandwidth compared to the controller designs in section 7.2.

Pressure Controller

As elaborated in section 7.2, the pressure control is secondary. The pressure controller G^-_{ppc} is therefore designed using the same criteria. Later it is shown that a bandwidth of 174.3 rad/s is achived for the velocity and the pressure controller is therefore designed for a crossover frequency at 17.4 rad/s. The controller is designed as a pure gain, as a steady state error can be accepted. Furthermore, the controller gain is chosen as negative, to compensate for the 180° phase shift. The pressure controller is given in equation (7.28).

$$G^-_{ppc} = -5.8 \cdot 10^{-7} \tag{7.28}$$

The open loop Bode diagram of the compensated pressure plant is given in figure 7.26, showing a crossover frequency of 17.4 rad/s. It is also illustrated, that the remaining resonance peak is suppressed by 10 dB. The closed loop step response is given to the right in figure 7.26, showing a steady state error of 2 %.

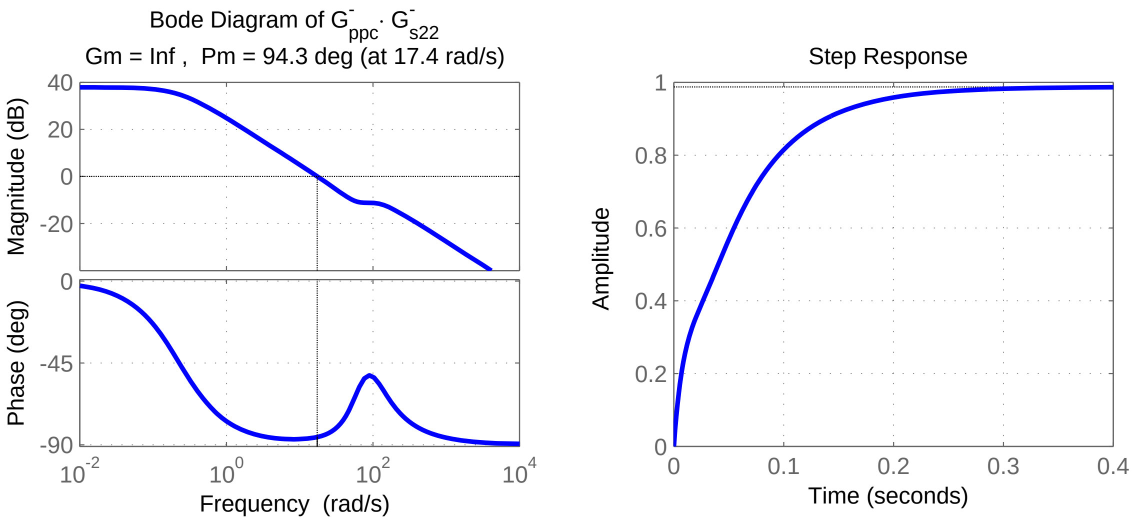

Figure 7.26. Left: Open loop Bode diagram of $G^-_{ppc} \cdot G^-_{s22}$ with active damping. Right: Step response of closed pressure loop.

Velocity Controller

For controlling the velocity plant, a PI-controller is designed, such that the system type is increased by one to remove the steady state error at step inputs, and include high frequency gain. The controller G^-_{vc}, is tuned to obtain a low rise time of the system, an overshoot of 10 % and a phase margin $> 45°$. The controller is given in equation (7.29).

$$G^-_{vc} = \frac{2750 \cdot (s + 60)}{s} \tag{7.29}$$

The Bode diagram of the open velocity loop is given to the left in figure 7.27 on the following page, showing a phase margin of 52.1° at the crossover frequency 111 rad/s. The closed loop step response is given to the right. Having established the velocity control, with a closed loop bandwidth of 174.3 rad/s (27.7 Hz), a position controller is designed, to evaluate the tracking performance in the physical test setup.

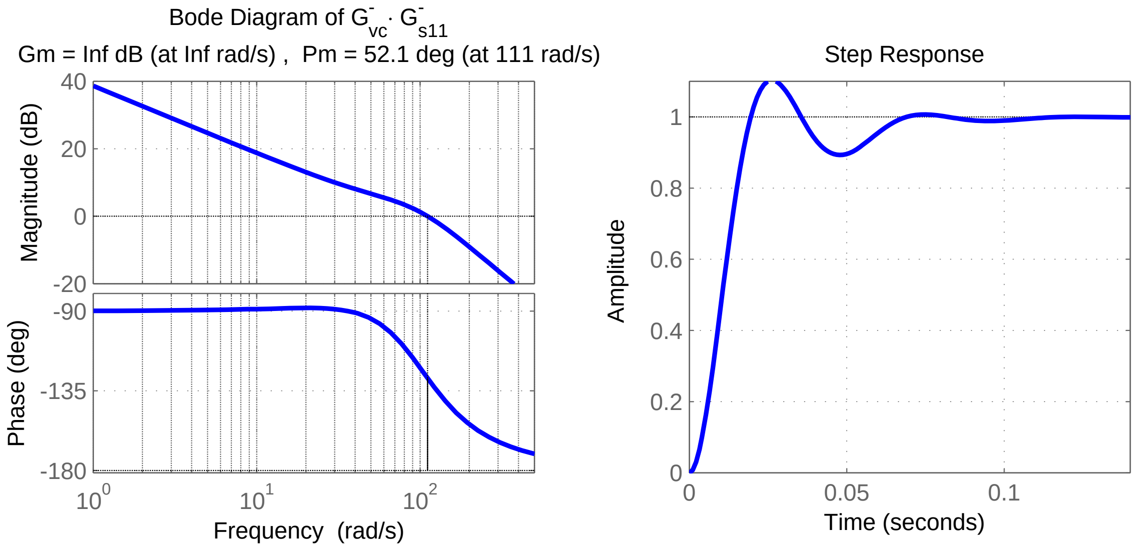

Figure 7.27. Left: Open loop Bode diagram of $G_{vc}^{-} \cdot G_{s11}^{-}$. Right: Step response of closed velocity loop.

Position Controller

The position plant, to be controlled, is given by the closed velocity loop multiplied by an integrator, making the system a type 1 system. The position is therefore designed as a pure gain, given in equation (7.30). The gain is determined such that the crossover frequency is 10 times lower than the bandwidth of the velocity loop i.e. 17.4 rad/s.

$$G_p^{-} = 17.8 \tag{7.30}$$

With all controllers designed for negative velocity, the tracking performance is evaluated in the following, with a simulation of the quintic trajectory applied as reference to the system. A simulation with the ramp trajectory is omitted, as the control input saturates, which causes failure of the active damping. This was shown and discussed from a simulation at positive velocity on page 87.

Simulation of Control System with Active Damping at Negative Velocity

A simulation of control system with active damping is given in figure 7.28 on the next page, where a part of the quintic trajectory is applied as reference. Only the part with negative velocity is utilized. The simulation reveals, that good tracking performance is obtained, where the rms velocity error is only 1.27 mm/s. The maximum error is 4 mm/s and there is no steady state error. The good velocity tracking also results in good tracking of the position. The rms position error is 0.07 mm and the maximum error is 0.2 mm. Thereby the goal of high tracking performance is fulfilled, but can not be verified in the laboratory without reconfiguration of the test setup, such that a good velocity estimate can be obtained, or a velocity sensor is mounted.

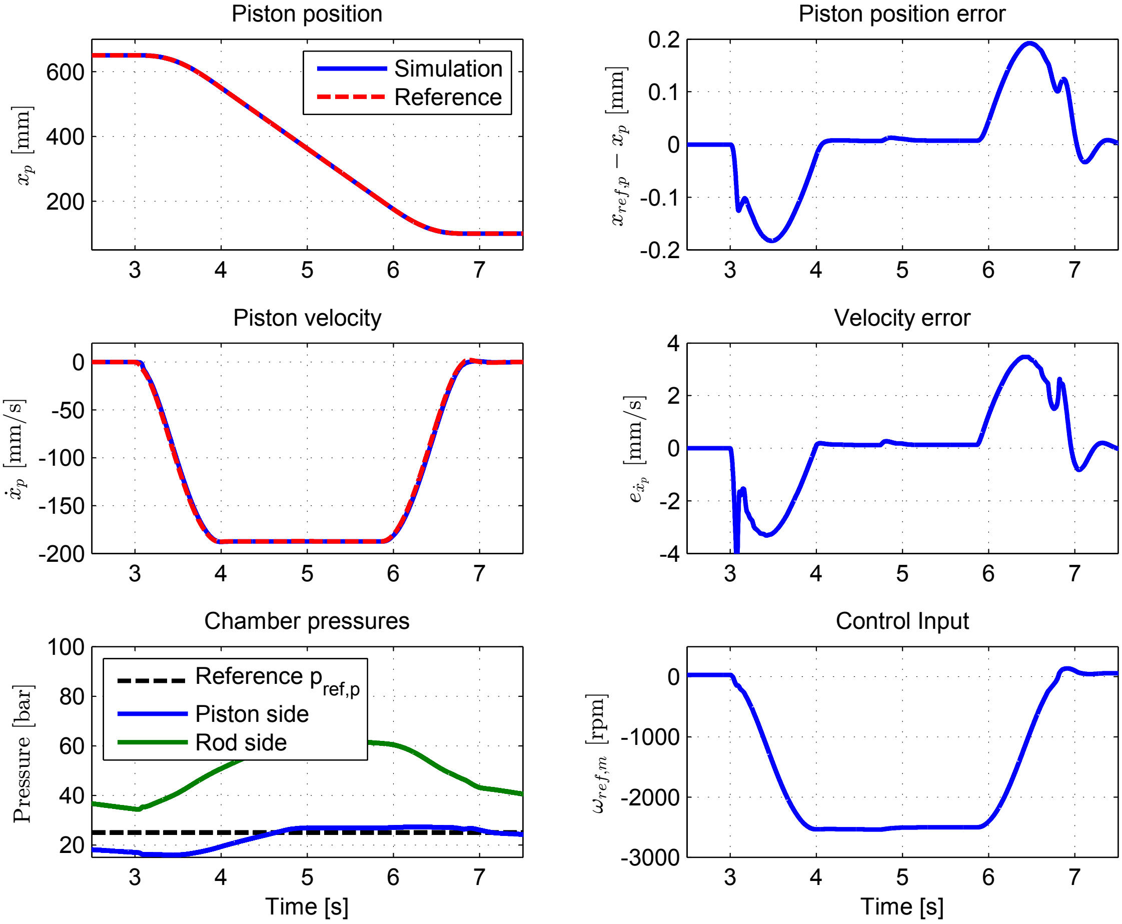

Figure 7.28. Simulation of the system response with pressure feedback in the control structure. The quintic trajectory with negative velocity is applied as reference.

To utilize the control system, designed throughout this chapter, for an application in the industry, a controller switching strategy is needed. The tracking performance was evaluated based on parts of the trajectories from chapter 4, as different controllers are needed for positive- and negative velocity. To test the performance over the entire trajectory, an automated switching strategy is needed. Such strategy is discussed in the following section.

7.4 Switching Strategy

Development of a switching strategy has not been prioritized in this thesis. Only the need for a switching strategy and the requirements for such, are elaborated is this section.

The characteristic of the SvDP-concept changes with the direction of movement, wherefore a set of controllers are designed for each case. This improves the overall performance of the system, as the controllers are designed for the specific characteristics in each case. Alternatively, one set of controllers could be utilized to regulate the system in the entire operation range. In such case, the controllers should be designed for the most critical operation point, to guarantee stability of the system. For the SvDP-concept mounted in the test setup, such a design would result in a very conservative control system which does not represent the potential of the system, as the achievable bandwidth is significantly larger at negative velocity compared to the situation where the system is operated at positive velocity.

Using the property that the system characteristic changes significantly with the sign of the velocity, two sets of controllers can be utilized to improve the overall performance. However, this requires an automated strategy which can switch between the two controller sets, depending on the direction of motion. Requirements for such strategy could be: the control inputs must remain continuous, windup of inactive integrators must be avoided, hysteresis switching between the controllers should be avoided etc. A proposal for switching, between the two high performance controllers, is illustrated in figure 7.29. Note that this proposal is not tested, nor is the stability the system proved to be guaranteed. It is simply an idea that is being presented.

The two sets of high performance controllers have the same control structure: a gain is present in the pressure feedback, a gain is utilized in the position control and a PI-controller is used to regulate the velocity. The idea is to utilize a hyperbolic tangent function to switch between the gains, depending on direction of motion, which is illustrated in figure 7.29. Using the hyperbolic tangent, abrupt changes are avoided in the controller gains and the control signal remains continuous.

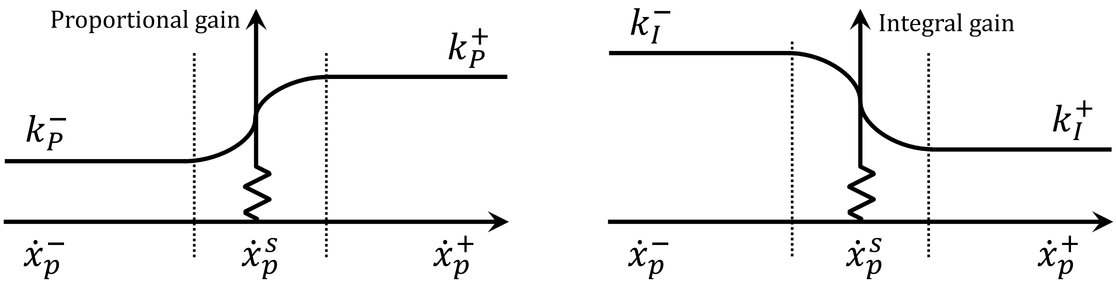

Figure 7.29. Idea for switching controller gain during operation, using the hyperbolic tangent function to avoid abrupt changes in the controller gains such that the regulator output remains continuous.

The proposed idea, presented in figure 7.29, contains several tuning parameters. One is the velocity $\dot{x}_p^s$, at which the gains should change. Another tuning parameter is the switching margin, determining the gradient of the hyperbolic tangent. These can be adjusted such that a desirable response is obtained. If the proposed switching strategy is implemented, the control system is altered from a linear system to a nonlinear system. This means that the system cannot be proven stable using classic control theory, but must be proven stable using nonlinear methods, e.g. Lyapunov theory.

7.5 Summary of Decentralized Control Strategy

The SvDP-concept is divided into two control systems with different characteristics depending on the direction of movement. During positive velocity, the system is reduced to a SISO system, while the system is a MIMO system at negative piston velocity. A decentralized control strategy is designed for the two systems. In order to design a decentralized controller for the system at negative piston velocity, the system is assumed decoupled, resulting in two SISO systems. Two controller design approaches are selected: a conservative and robust controller design and a design where the goal is high tracking performance. The conservative design approach is included, such that experimental results can be obtained. Noisy signals prevent a good velocity estimation, wherefore proportional gain of the velocity error should be avoided in the implemented controllers.

The conservative controller for positive velocity is designed as a cascaded controller, with an inner loop controlling the velocity and an outer loop controlling the position. The velocity controller consists of a second order input filter combined with an integrator. A closed loop bandwidth of 18.65 rad/s is obtained for controlling the velocity. This controller is implemented and tested in section 8.3.1.

Before designing controllers for the case where the piston velocity is negative, the level of interaction between the in- and outputs is determined from an RGA analysis, as the system consists of two in-and outputs. The RGA analysis shows that the diagonal pairing of the system is strongest at low frequencies, wherefore it is decided to couple the piston velocity with the pump speed and the piston pressure with the valve input. The structure of the position controller at negative velocity is identical to the controller utilized for positive velocity control, however, the gains and poles are altered to suit the faster system. A closed loop bandwidth of 34.77 rad/s is obtained for controlling the velocity. The pressure controller is designed as a proportional controller, which regulates the piston side pressure with a closed loop bandwidth of 6.2 rad/s.

Controllers are designed for high tracking performance to reveal the potential of the SvDP-concept, provided that a good piston velocity estimate/measurement is available in the test setup. To improve the damping ratio of the system and thereby the achievable bandwidth, active damping is designed to induce ”virtual leakage” in the system. The system is simplified using a *virtual* load pressure to determine the magnitude of the active damping controller. The pressure feedback is designed such that the system obtains a damping ratio of $1/\sqrt{2}$, as this yields the lowest time constants of a second order system (Philips and Parr, 2011). With active damping included in the controller structure, PI-controllers are tuned to obtain a fast system response. A bandwidth of 108.6 and 174.3 rad/s is obtained for the positive- and negative velocity control loop, respectively. The controllers are tested in the simulation model, revealing that an rms velocity error of 2.45 mm/s is obtained at positive velocity and 1.27 mm/s at negative velocity, when tested with the quintic trajectory.

Controller Implementation and Evaluation 8

In this chapter, the decentralized control strategy, designed in chapter 7, is implemented and evaluated in the test setup. Initially, in section 8.1, the practical implementation of the controllers is reviewed. In section 8.2, estimation of the piston velocity is discussed. Here, problems related to velocity estimation from measurements of the piston position, are elaborated and different estimation techniques are compared. Finally, in section 8.3, the performance of the conservatively designed controllers from sections 7.1 and 7.2, is evaluated.

8.1 Controller Implementation

In this section, considerations regarding implementation of the controllers and filters, designed in this project, are reviewed. The control of the system is implemented on a PLC controlling the servo motor, as illustrated in Appendix B, figure B.1, where a complete description of the test setup is provided.

The PLC is programmed using structured text, which operates at a sampling frequency of 1 kHz. As the controllers are designed in the continuous time domain, they must be discretized in order to be implemented on the PLC. The controllers are discretized using the bilinear transform, where the Laplace variable s is substituted with Tustin's formula, given in equation (8.1). (Glad and Ljung, 2010)

$$s = \frac{2}{T_s}\frac{z-1}{z+1} \tag{8.1}$$

In equation (8.1), T_s is the sampling time of the system. The z-transformed transfer functions are converted into difference equations before being implemented in the PLC. An example is given in equation (8.2), where the velocity controller G_{vc}^{+}, from equation (7.2) on page 66, is z-transformed with T_s equal to 1 ms. The corresponding difference equation is given in equation (8.3).

$$G_{vc}^{+}(z) = \frac{\omega_{ref,m}(z)}{e_{\dot{x}_p}(z)} = \frac{1.9\text{e-}3 \cdot z^3 + 5.7\text{e-}3 \cdot z^2 + 5.7\text{e-}3 \cdot z + 1.9\text{e-}3}{z^3 - 2.9 \cdot z^2 + 2.9 \cdot z - 0.9} \tag{8.2}$$

$$\begin{aligned}\omega_{ref,m}[n] =& 2.9 \cdot \omega_{ref,m}[n\text{-}1] - 2.9 \cdot \omega_{ref,m}[n\text{-}2] + 0.9 \cdot \omega_{ref,m}[n\text{-}3] + ... \\ & 1.9\text{e-}3 \cdot e_{\dot{x}_p}[n] + 5.7\text{e-}3 \cdot e_{\dot{x}_p}[n\text{-}1] + 5.7\text{e-}3 \cdot e_{\dot{x}_p}[n\text{-}2] + 1.9\text{e-}3 \cdot e_{\dot{x}_p}[n\text{-}3]\end{aligned} \tag{8.3}$$

Similar transformation is performed on the remaining controllers from sections 7.1 and 7.2, which are implemented in the PLC.

To determine the velocity error, the actual piston velocity is needed. In the test setup, only a position sensor is available. Differentiation of the piston position yields the piston velocity, but noisy signals complicates the determination of piston velocity from the measurements. In the following, considerations on the problem are reviewed.

8.2 Estimation of Piston Velocity

In order to control the piston velocity, as required by the designed controllers, it must be determined from the piston position as a velocity sensor is not available. This means that the piston position must be differentiated. When the position measurements contain noise, differentiation of the signal may lead to a poor approximation of the velocity as the noise distorts the desired output.

To determine the frequency range of the noise, contained in the position signal, a Fast Fourier Transform (FFT) analysis is performed on a measurement, given in the top of figure 8.1. The result of the FFT analysis is shown in the bottom figure 8.1, where the DC-component is subtracted from the analyzed measurements.

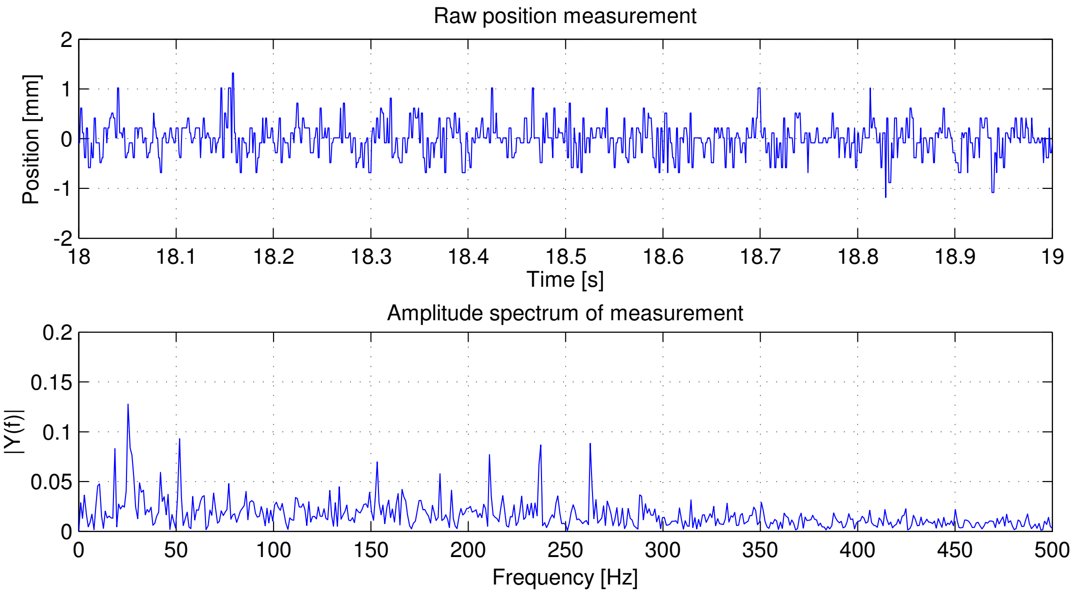

Figure 8.1. Top: Measurement of the piston position. Bottom: FFT analysis of the measurement, showing the frequency spectrum of the signal. The DC-component is subtracted from the analyzed measurement.

As seen in the bottom of figure 8.1, the frequency spectrum of the signal does not clearly consist of one frequency component. The spectrum of the signal resembles the spectrum of white noise, which has a constant amplitude spectrum. This means that it is impossible to filter out all the noise, using for example a low pass filter. Furthermore this means that differentiation of the signal will amplify the noise, leading to a very noisy velocity estimate. This is clearly illustrated later, in the top of figure 8.2 on page 98, where the signal is differentiated.

The noise in the position measurements, is expected to origin from the hardware in the test setup. Here, a signal splitter is utilized to convert and divide the signal into two, providing both the data- and servo PLC with the position measurement. In the signal splitter, the 4-20 mA signal, from the position sensor, is converted into a voltage signal. It is expected that the noise originates from this conversion and splitting, and can not be avoided in the current configuration of the hardware.

To determine/estimate the velocity from the position measurements, three techniques are tested and the outputs are compared in figure 8.2 on the following page. In the following the three techniques are elaborated. Initially, the conventional differentiation is presented. This is followed by two nonlinear methods for differentiating signals, proposed by Schmidt et al. (2013) and Levant (2003). These techniques are based on sliding control.

- **Conventional differentiation:** Ideally, differentiation of the position signal yields the velocity signal. In the continuous frequency domain, this is done by utilizing the differentiating transfer function "s", however, this is not a realizable transfer function. In order to make a realizable differentiator, a first order low pass filter is introduced, giving the differentiating transfer function in equation (8.4).

  $$H_{diff}(s) = \frac{\omega_c \cdot s}{s + \omega_c} \tag{8.4}$$

  The filter shown in equation (8.4) differentiates the input signal, i.e. the filter amplifies changes in the input and suppresses the steady state value. This means that the change in position is given as output, but the noise of the signal is also amplified. Depending on the noise level, this may become the dominating part of the velocity estimate, which is undesirable. Finally, when utilizing classic differentiating filters, an unwanted phase shift is introduced in the control system if the real pole is placed too closed to the eigenfrequency of the system.

- **Second Order Sliding Algorithm (SA2):** In order to avoid introducing unwanted phase shift and amplification of the noise when differentiating the position signal, other methods for differentiating signals are investigated. Schmidt et al. (2013) describes a second order Sliding Algorithm (SA2) for differentiation. This algorithm is given in equation (8.5), where x_p is the measured position. $\hat{x}_p$ is the estimated position and $\dot{\hat{x}}_p$ is the estimated velocity. $\dot{z}$ can be considered as the estimated acceleration.

  $$\begin{aligned} \dot{\hat{x}}_p &= -1.5 \cdot \delta^{1/2} \cdot |\hat{x}_p - x_p|^{1/2} \cdot \mathrm{sign}(\hat{x}_p - x_p) + z \\ \dot{z} &= -1.1 \cdot \delta \cdot \mathrm{sign}(\hat{x}_p - x_p) \end{aligned} \tag{8.5}$$

  As seen in equation (8.5), the algorithm approximates the piston velocity and acceleration, where the approximated piston velocity $\dot{\hat{x}}_p$ is utilized as the output. The proposed differentiator only has one design parameter δ, making it fairly simple to implement and tune. By selecting $\delta > |\ddot{x}_{p,max}|$, finite time convergence is ensured.(Schmidt et al., 2013) The SA2 differentiator is utilized on a noisy signal and the output is shown in the top of figure 8.2.

- **Third Order Sliding Algorithm (SA3):** The differentiator proposed by Levant (2003) is in principal the same differentiator as the SA2 algorithm, presented in equation (8.5). However, Levant (2003) proposes a third order Sliding Algorithm (SA3), given in equation (8.6).

$$\begin{aligned}\dot{\hat{x}}_p &= -3 \cdot L^{1/3} \cdot |\hat{x}_p - x_p|^{2/3} \cdot \mathrm{sign}(\hat{x}_p - x_p) + z_1 \\ \dot{z}_1 &= -1.5 \cdot L^{1/2} \cdot \left|z_1 - \dot{\hat{x}}_p\right|^{1/2} \cdot \mathrm{sign}(z_1 - \dot{\hat{x}}_p) + z_2 \\ \dot{z}_2 &= -1.1 \cdot L \cdot \mathrm{sign}(z_2 - \dot{z}_1)\end{aligned} \tag{8.6}$$

  As seen in equation (8.6), the last two states of the algorithm are similar to the states in the SA2 algorithm, shown in equation (8.5). Where SA2 estimates the velocity and acceleration, SA3 also estimates the jerk, $\dddot{x}_p$. Similar to the SA2 algorithm, SA3 also only has one design parameter L, making it easy to tune. The design parameter in SA2, δ, relates to the acceleration, whereas the design parameter of SA3 L relates to the jerk of the piston, and is selected such that $L \geq |\dddot{x}_{p,max}|$.(Levant, 2003) SA3 is implemented and compared to the other differentiators in the top of figure 8.2.

In attempt to filter out the high frequency noise, included in the pure differentiation of the signal (top of figure 8.2), a second order low pass filter is implemented. The cutoff frequency of the low pass filter is placed at 500 rad/s, in order to reduce the effect of phase shift. The results after filtering are shown in the bottom of figure 8.2.

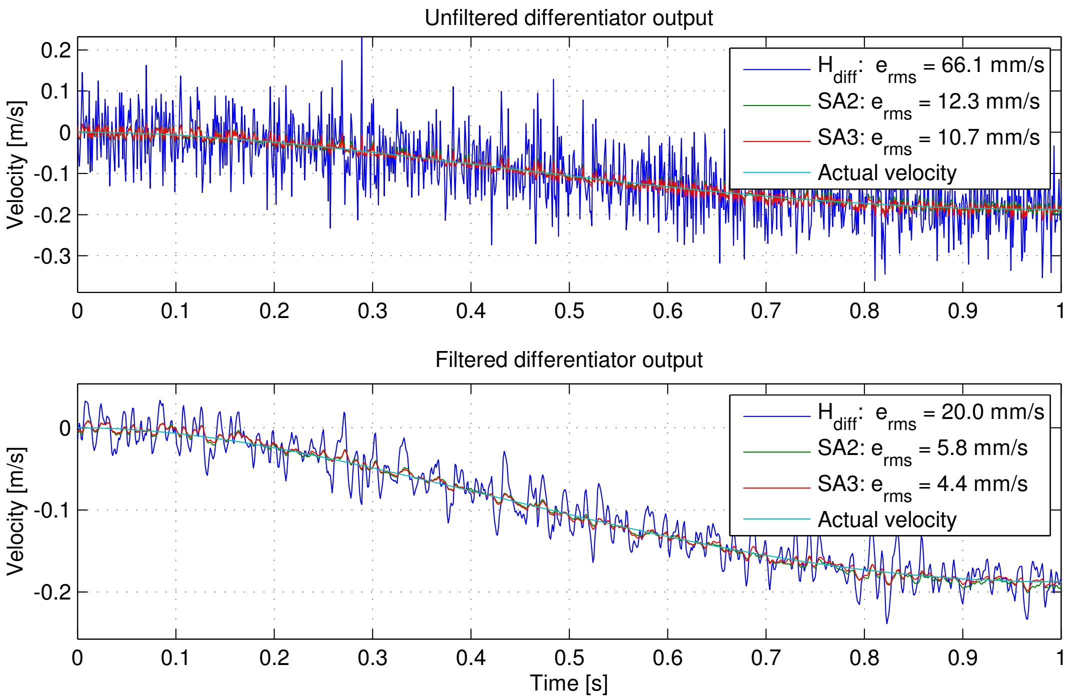

Figure 8.2. Top: An unfiltered comparison of the utilized differentiation methods. Bottom: Filtered output of the different differentiation methods.

As seen in figure 8.2, the filtered signal has a lower error than the unfiltered signal, while the phase of the signal seems unaffected. It is evident that the performance of the differentiating filter H_{diff} is far worse than the performance of the two sliding algorithm differentiators. Furthermore, figure 8.2 shows that the performance of SA3 is slightly better than the performance of SA2. However, as SA2 is much simpler to implement than SA3, it is assessed that the performance gained from SA3 is outweighed by the complexity. Therefore SA2 is utilized to differentiate the piston position online, providing a velocity estimate as feedback to the control system.

It should be noted that the signal is fluctuating with an average error of 5.8 mm/s, which leads to fluctuation control inputs if a proportional gain is utilized in the velocity controller. With the proportional gains, used in the controllers designed for high performance in section 7.3, an rms error in the velocity estimation of 5.8 mm/s will result in chattering of approximately 166 rpm on the control input. A chattering of this magnitude causes the system to shake, causing velocity spikes which are further amplified. This leads to behavior which stresses and potentially can damage the system. Therefore, only the conservative controllers, designed in sections 7.1 and 7.2, are tested in the laboratory, as the control input to the servo drive is input filtered. The results are presented and evaluated in the following.

8.3 Test of Decentralized Control Strategy

In this section, the two decentralized control strategies for positive- and negative velocity, are evaluated in the physical setup. The controllers are tested using the four trajectories, designed in chapter 4. Here, two types of trajectories were designed: a quintic- and a ramp trajectory, both starting at two different positions. This yields four test cases, shown in figures 4.1 and 4.4 on page 40→42:

- **Quintic trajectory**
    1. Start position at 100 mm - denoted positive quintic trajectory
    2. Start position at 650 mm - denoted negative quintic trajectory
- **Ramp trajectory**
    1. Start position at 100 mm - denoted positive ramp trajectory
    2. Start position at 650 mm - denoted negative ramp trajectory

In the following, the performance of both the positive- and negative velocity controller, from sections 7.1 and 7.2 respectively, are evaluated in the four test cases.

8.3.1 Positive Velocity Controller

The positive controller, designed in section 7.1, is evaluated using both quintic trajectories and ramp trajectories. This means, both the positive- and negative trajectories are tested i.e. start position at 100 mm and 650 mm, respectively. In all four cases, only the results, obtained during parts of the trajectories, where the velocity is positive, are presented, as the controller is only designed for this case.

- **Quintic Trajectories**

The results obtained in the laboratory, when applying both the positive- and negative quintic trajectories, are shown in figures 8.3 and 8.4 on the next page, respectively. In the two figures, the trajectories seem identical, however, it is seen that the performance in figure 8.4 is better than the performance, obtained from the experiment, presented in figure 8.3. This is despite the fact that the exact same controller is utilized. The different performance occurs, due to the fact that the pressure level in one test case is 5 bar higher than the other. In the following the difference is discussed, which reveals that the performance is significantly improved if the the pressure level is increased with only a few bar. Initially, both test results are presented, which is followed by a discussion of the performance.

1. **Positive Quintic Trajectory - Start Position at 100 mm:**
   In figure 8.3, a test is presented, where the initial piston position is 100 mm. This means, the system system is started from rest at this position. Hereafter the trajectory is completed, but only the part, where the velocity is positive, is given in figure 8.3.

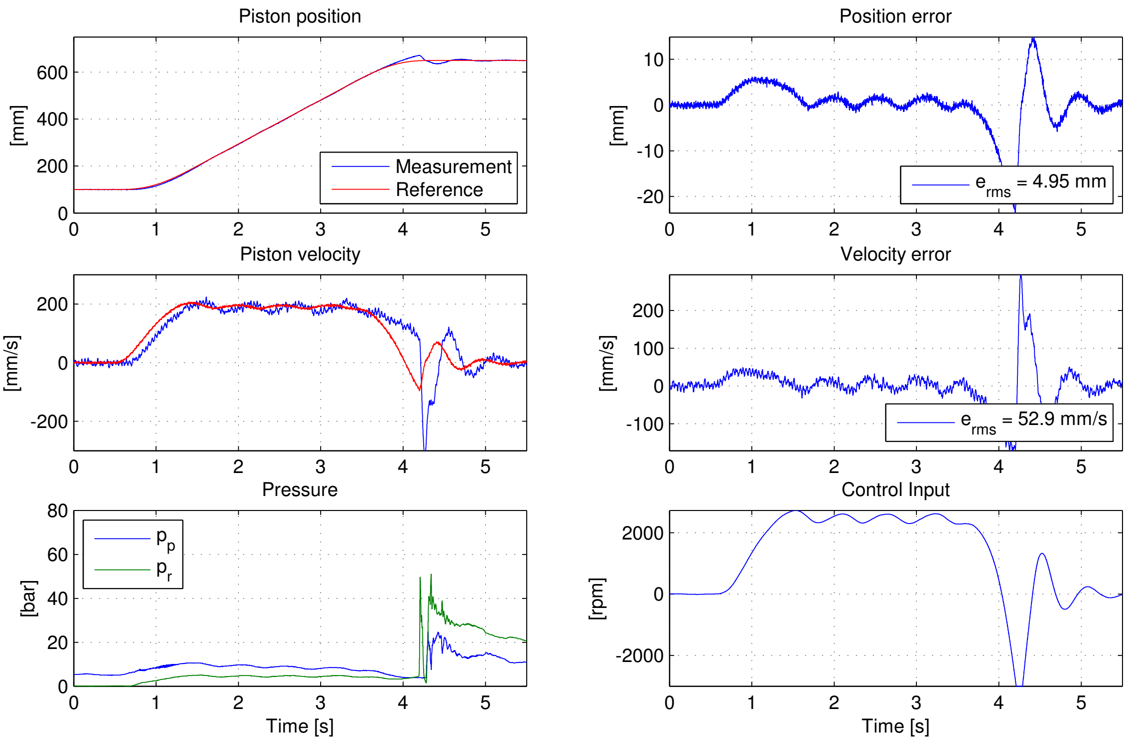

Figure 8.3. Experimental results obtained using the positive velocity controller, when applying the positive quintic trajectory.

The rod side pressure measurement in figure 8.3, starts at 0 bar, and even becomes slightly negative during the first second. Due to the configuration of the system (the anti cavitation system), it is not possible for the pressure to be 0 bar or negative. The fact that the system is in steady state at zero velocity, means it is highly unlikely that the pressure is 0 or negative. This indicates, there is an offset in the pressure measurements, however, as this is difficult to verify, and the fact that a slight offset of the pressure measurements does not greatly deteriorate the system performance, this has not been investigated further.

It is seen in figure 8.3 that the position drifts away from the reference when the position reaches approximately 600 mm. This is due to the change in load direction which occurs at 600 mm, as seen in figure 2.11 on page 18. Here it is shown that the load changes from a pushing- to pulling load, causing overrun due to the low pressure in the chambers. This leads to a large spike in the position error, yielding a poor performance of the system.

2. **Negative Quintic Trajectory - Start Position at 650 mm:**
In this test, the trajectory starts with an initial piston position of 650 mm. This means, the system is initially actuated with negative velocity, followed by an actuation with positive velocity, when the position has reached 100 mm. The measurements obtained during the part of the trajectory, where the velocity is positive, are depicted in figure 8.4. As the actuation is initially negative, the pressure has built up, resulting in a higher pressure level (on average 5 bar) during this test compared to the test depicted in figure 8.3 on the facing page.

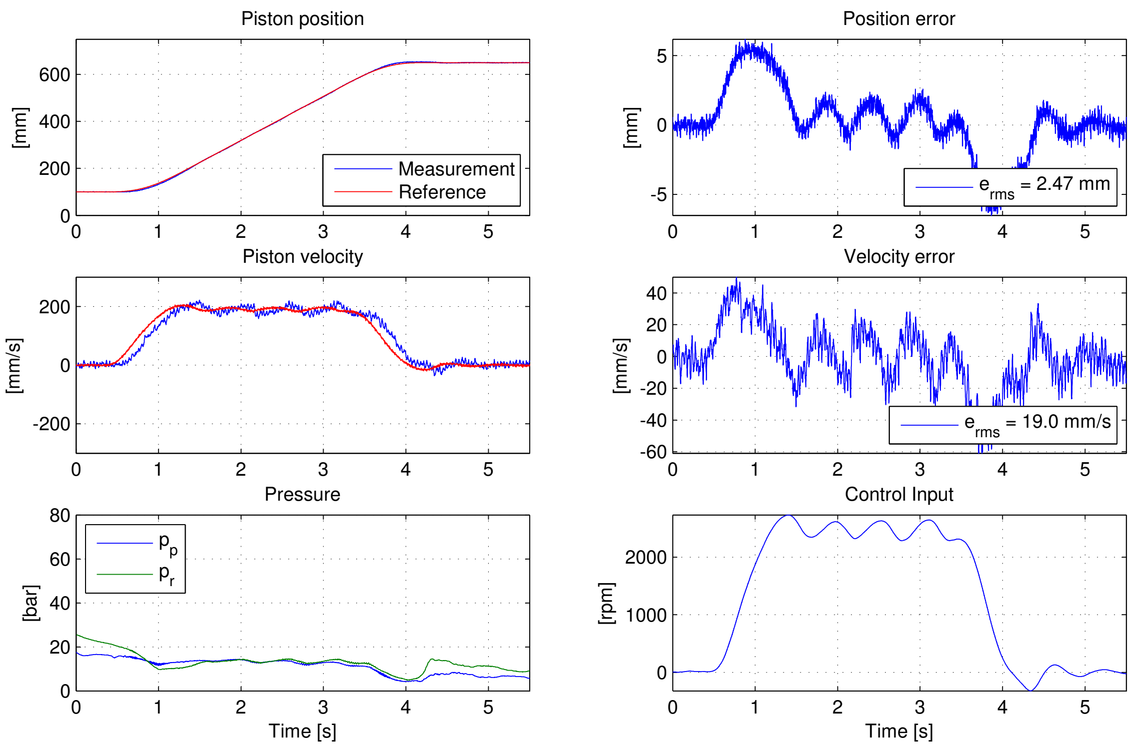

Figure 8.4. Experimental results obtained using the positive velocity controller, when applying the negative quintic trajectory.

The higher pressure level during this test results in an increased performance, compared to the test depicted in figure 8.3 on the preceding page. This is discussed next.

The 5 bar higher pressure level, in the test with the negative quintic trajectory, leads to a better performance of the system, compared to the test with the positive quintic trajectory. This is clearly seen in the rms error of the piston position and velocity. The rms position errors are 4.95 and 2.47 mm for the positive- and negative quintic trajectory, respectively. The same result is obtained when considering the tracking performance. The rms velocity errors are 52.9 and 19.0 mm/s, respectively. This leads to the observation that the performance can be increased by more than 100 % if the virtual tank pressure is raised from 2.5 to 7.5 bar. This is due to the fact that the stiffness of the oil increases dramatically in this pressure range.

A low frequent oscillation can be seen in the error measurement along with the control input in both figure 8.3 and 8.4. This is likely due to the second order low pass filter implemented to filter the noisy position signal, causing phase shift. It seems as if the slight phase shift induced by the second order filter causes the velocity loop to have a slight oscillation. However due to the relative low error induced by this, the effect is not investigated further.

Finally, it is seen that the control input to the system is fairly well behaved, meaning that the signal does not chatter due to noise, and that the signal is never saturated. However, this is expected as the control input is filtered through a second order low pass filter, attenuating all high frequency outputs there might be.

- **Ramp Trajectories**

As mentioned in section 4.2, the ramp trajectory is intentionally designed to be impossible to track, but is used to push the system to test the robustness of the system to extreme inputs.

1. **Positive Ramp Trajectory - Start Position at 100 mm:**
   The results from the laboratory, when applying a positive ramp to the positive velocity controller, are shown in figure 8.5 on the facing page.

   The measured response of the piston position in figure 8.5 shows the same tendencies of position overshoot, as in figure 8.3, when the piston position is approximately 600 mm. This is due to the low pressure of the system and changing load, as discussed earlier. When the ramp starts an error of approximately 20 mm occurs, as the system cannot track the velocity reference, which is a step input. The steps in velocity lead to large velocity errors at the beginning and the end of the ramp of approximately ± 250 mm/s. This yields a poor performance of the positive controller when applying a ramp trajectory, as it has an rms error of 76 mm/s.

   The control input, shown in figure 8.5, is saturated when the ramp starts. However, the anti windup ensures that the piston velocity does not have a large overshoot on the velocity reference. The input filter on the control input ensures that the control input of the system is not noisy, however, it is evident that the input filter limits the performance of the system during acceleration of the piston and deceleration. Omitting the input filter would clearly speed up the acceleration of the piston, but this it not possible due to the velocity feedback, which is distorted by noise.

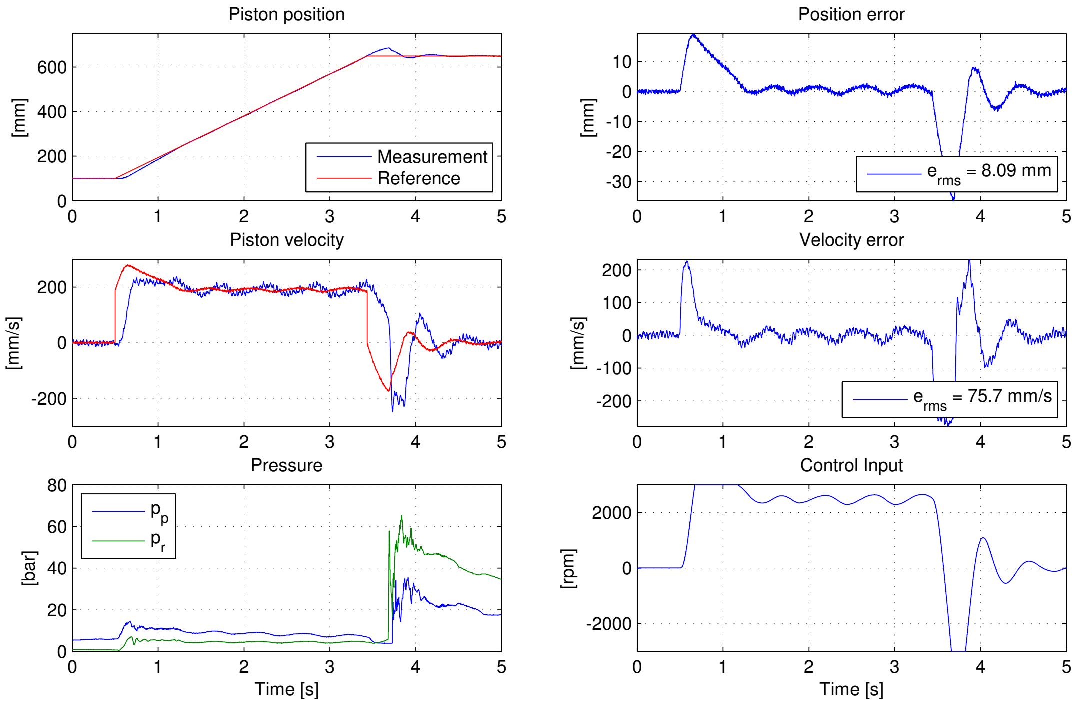

Figure 8.5. Experimental results obtained using the positive velocity controller, when applying the positive ramp trajectory.

2. **Negative Ramp Trajectory - Start Position at 650 mm:**
   The results from the laboratory, when applying a negative ramp to the positive velocity controller, are shown in figure 8.6.

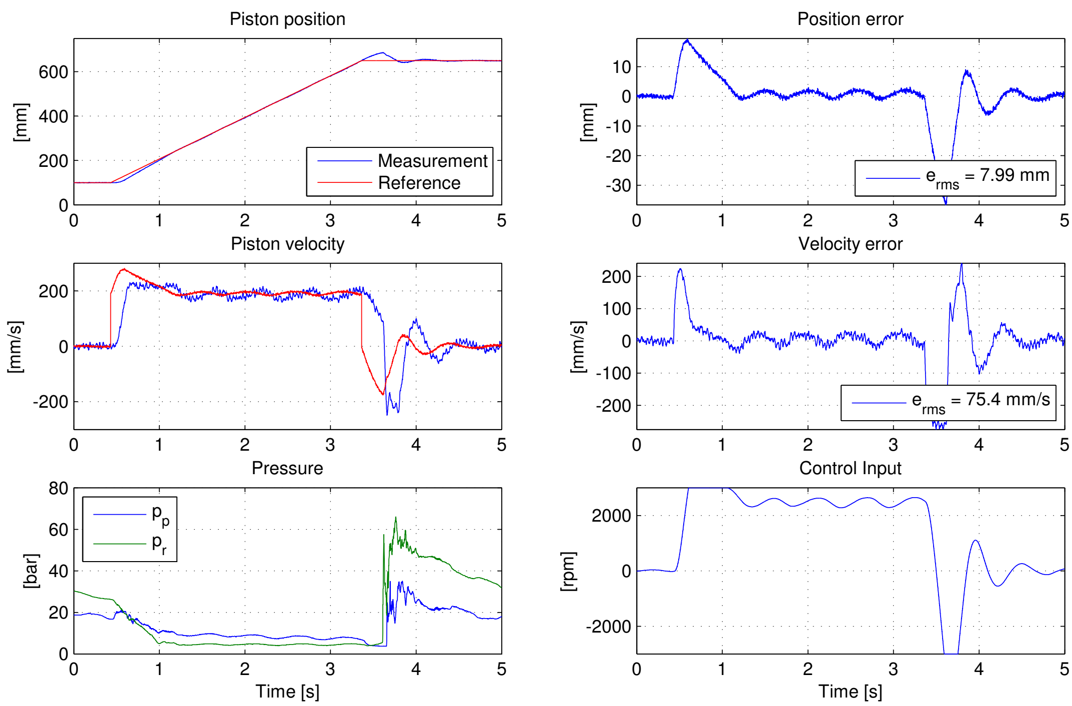

Figure 8.6. Experimental results obtained using the positive velocity controller, when applying the negative ramp trajectory.

Unlike the tests with the quintic trajectories, the two tests with the ramp trajectories are similar. Even though the pressure level initially is high in the test shown in figure 8.6, the pressure level drops to the same level after the first step in the velocity reference. The same observations, made with the positive ramp trajectory, therefore applies to the test with the negative ramp trajectory in figure 8.6.

8.3.2 Negative Velocity Controller

The set of controllers, designed for negative velocity in section 7.2, are evaluated using the quintic- and ramp trajectories. Unlike the positive controller, the negative controller structure also includes regulation of the piston side pressure. Both the positive- and negative trajectories are tested, however, only the results from the negative trajectories are presented, as the performance is similar in both cases.

- **Quintic Trajectory**

The results, obtained from experiments with the controllers designed for negative velocity, are shown in figure 8.7, where the quintic trajectory is applied as reference.

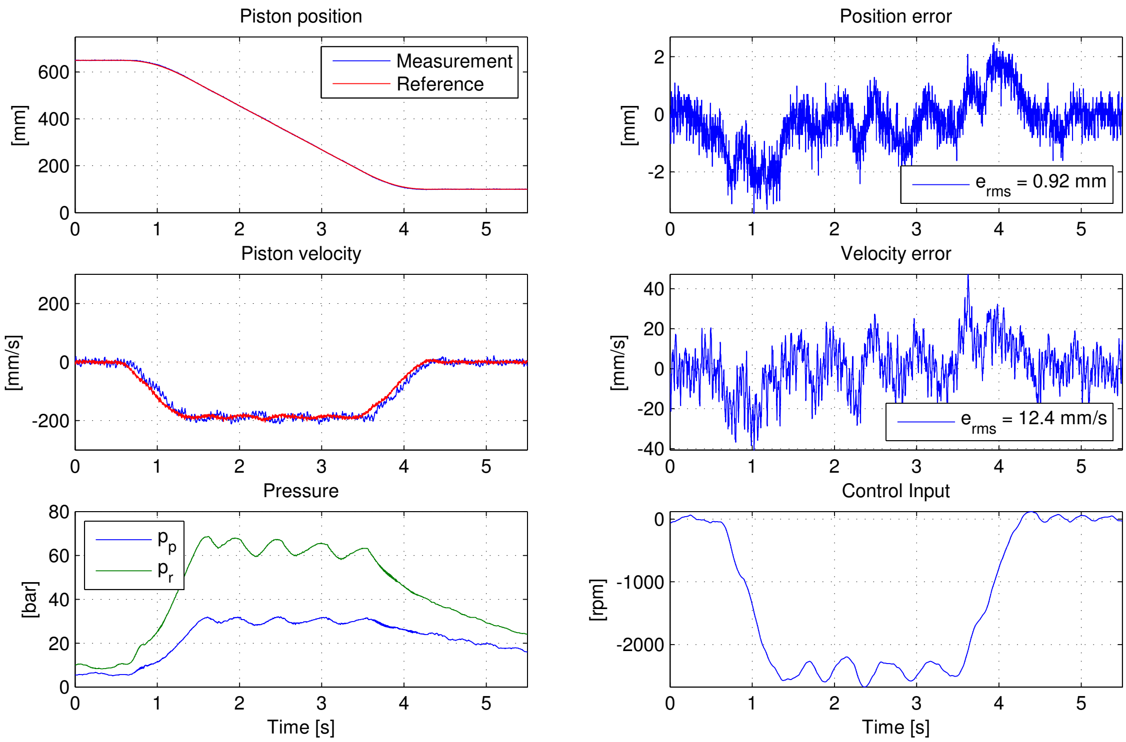

Figure 8.7. Experimental results obtained using the negative velocity controller, when applying the quintic trajectory.

It is immediately clear that the performance of the negative controller is superior to the performance of the positive controller. The rms position error is 2.5-5 times lower than the errors during positive velocity. This is due to the higher bandwidth of the system, which is obtained because the pressure levels increase when piston velocity is negative.

This results in increased stiffness of the system, which increases the achievable bandwidth of the control system.

In figure 8.7, it is seen that the pressure rises as the trajectory starts, which is expected from the steady state analysis in chapter 3. When the piston side pressure reaches 25 bar, the pressure controller is enabled, limiting the pressure around 30 bar. This means that there is an error of approximately 5 bar. This is expected as the pressure controller is a P-controller, resulting in a type 0 system. This will result in steady state error when a step input is applied. Comparing the pressures in figure 8.7 to the pressures, measured during the initial trajectory test, in figure 4.3 on page 41, where no pressure control is utilized, it is clear to see that the pressure has been limited when utilizing the negative velocity controller.

- **Ramp Trajectory**

The results, obtained from experiments with the controllers designed for negative velocity, are shown in figure 8.8, where the ramp trajectory is applied as reference.

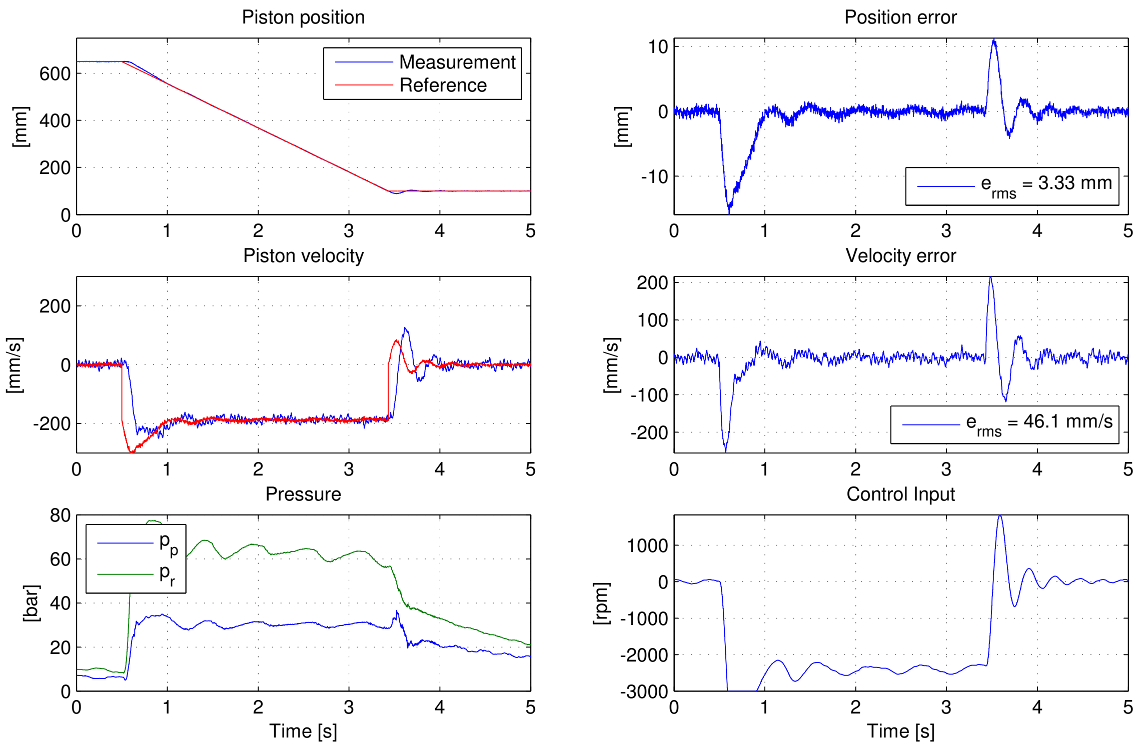

Figure 8.8. Experimental results obtained using the negative velocity controller, when applying the negative ramp trajectory.

The observations made when the quintic trajectory was utilized as reference, also applies to the test shown in figure 8.8. The results in figure 8.8 also shows improved performance, compared to the ramp trajectory applied to the positive controller. As previous, when the ramp trajectory is utilized, the control input saturates when the velocity step is applied. However, in this case, the saturation time is lower due to the increased system response.

8.4 Summary of Controller Implementation and Evaluation

The controllers, designed in sections 7.1 and 7.2, have been discretized and implemented in the test setup. To realize the controllers the piston velocity is needed, but only position measurements are available in the setup. Three different techniques of determining the velocity, from the position measurements, have therefore been compared. Traditionally, the velocity is obtained by differentiating the position signal, but noise results in a distorted output.

An analysis of a position measurement was carried out, showing that the frequency spectrum of the measurement resembles the spectrum of white noise. This complicates the problem, as the noise can not be filtered, without loosing the information about the velocity. Therefore, two techniques of differentiation proposed by Schmidt et al. (2013) and Levant (2003), based on sliding mode, was compared with the conventional differentiation. The sliding mode estimators, provided a velocity estimation, less distorted by the noise and it was decided to implement the second order Sliding Algorithm proposed by Schmidt et al. (2013).

Despite the improved velocity estimate, the noise still prevented implementation of velocity controllers containing a proportional gain, as it results in chattering control input to the servo drive. Therefore only the conservative controller designs from sections 7.1 and 7.2, have been tested. The controllers have been tested with the quintic- and ramp trajectories.

Tests of the controller designed for positive velocity, revealed that the tracking performance is sensitive to the pressure level in the system. During the movement of the piston, the velocity error was reduced to 50 %, in the case where the chamber pressure was 7.5 bar compared to the case where it was 2.5 bar. The minimum rms velocity error was 19.0 mm/s for the quintic trajectory and 75.4 mm/s when applying the ramp trajectory.

Tests of the controller designed for negative velocity, revealed significant improvements of the tracking performance, compared to the positive velocity controllers. The rms velocity error was 12.4 mm/s for the quintic trajectory and 46.1 mm/s for the ramp trajectory. The increased tracking performance, compared to the positive velocity controllers was expected, as the increased pressure level allowed a controller design, resulting in an increased bandwidth of the system. During tests the pressure was also controlled, where a steady state error of 5 bar was present.

Conclusion 9

In this thesis a new concept for actuating a hydraulic cylinder is studied. The new concept consists of two fixed displacement pumps, matched to the area ratio of the piston in the cylinder, and driven by a single speed-variable servo drive. Furthermore, over pressure valves, an anti-cavitation system and two proportional valves to control the pressure levels, are included in the concept. The concept was develop and created in a collaboration between Bosch Rexroth A/S and the M.Sc. students Bertelsen and Madsen (2013).

A nonlinear simulation model of the hydro-mechanical actuation system is derived and validated from experiments preformed on the test setup provided by Bosch Rexroth A/S. The validation reveals that some nonlinearities are not captured in the simulation model, resulting in an underestimation of the pressure levels. Despite this deviation, it is concluded that the simulation model provides a sufficiently accurate representation of the test setup.

An analysis of the system, actuated at steady piston velocity, is performed to examine the characteristics of the system. Initially, a general analysis of the system is carried out to outline the properties of the concept. This is followed by a more detailed analysis, in order to determine the characteristics of the specific system available in the laboratory. The analysis reveals that the system pressure is highly dependent on the direction of movement: When the direction of movement is positive, the system pressure drops, and when the direction of movement is negative, the system pressure increases. It is concluded that pressure control is only required when the direction of movement is negative. In the laboratory setup it is only needed to perform pressure control on the piston side chamber, as the two chambers are coupled and the piston side pressure is always lowest when the desired minimum pressure of 25 bar is reached.

Two types of trajectories are designed to test the system: a quintic- and a ramp trajectory. The quintic trajectory is designed to ensure that the velocity and acceleration demands are achievable by the control system. The ramp trajectory is designed to excite the system dynamics. Initially, both a slow trajectory and a fast trajectory is designed, however an initial test reveals that the slow trajectory does not result in a sufficient pressure rise for pressure control to be required, wherefore it is discarded. The fast trajectories are designed for a servo speed of ± 2500 rpm and a piston position ranging from 100-650 mm.

The nonlinear model is simplified and a linear model is derived. The eigenvalues of the linear model are examined and two critical operation points are determined; one for positive velocity and one for negative velocity. The linear model describing the system at positive piston velocity results in a single transfer function, while the linear model describing the system at negative velocity is a MIMO system with two in- and outputs. The linear models are simplified, by neglecting the valve- and servo drive dynamics, and is verified by comparison with the simulation model.

Two sets of decentralized controllers are designed for different purposes: A set of conservative controllers and a set of high performance controllers. The conservative controllers are designed for implementation in the test setup, where a poor velocity feedback is available. If not designed conservatively, the noise in the velocity estimate, results in chattering of the control input and thereby stressing the system. The high performance controllers are designed to reveal the potential of the SvDP-concept, but are unable to be tested in the laboratory without an improved velocity measurement.

The controllers are designed as a cascaded structure, containing an inner velocity control loop and an outer position control loop. The positive velocity system is a SISO system, wherefore a set of SISO controller are designed directly. The controller is designed as a second order input filter combined with an integrator to suppress the resonance peak in the system and filter the control signal. At negative pump speed, the system is a MIMO system, which requires a set of controllers. The system is analyzed using RGA to determine the level of interaction between the in- and outputs, which reveals a strong diagonal coupling in the frequency range where the system is to be controlled. The off-diagonal coupling is weak and negative at steady state, wherefore it is assessed that the MIMO system can be treated as two SISO systems without taking the cross-coupling into consideration in the design process. The negative velocity controller is designed identically to the positive velocity controller, while the pressure controller is designed as a proportional controller.

The high performance controllers are designed using pressure feedback, which induces virtual leakage in the system, resulting in a higher damping ratio. The pressure feedback is designed such that the system obtains a damping ratio of 0.71. PI-controllers are hereafter designed to obtain a fast velocity response of the system. The closed loop bandwidths of the inner velocity loop, obtained with the different controllers, are given in table 9.1, which show a significant difference between the conservative- and high performance controllers.

	Closed loop bandwidth	
Controller	Conservative	High performance
Positive velocity	18.65 rad/s	108.6 rad/s
Negative velocity	34.77 rad/s	174.3 rad/s

Table 9.1. Closed loop bandwidth of the designed velocity controllers.

The controllers are tested and the performance is evaluated in the simulation model prior to experimental tests. The tracking performances, obtained during simulations, are given in table 9.2 for the quintic trajectory. The performance of tracking the ramp trajectory is omitted, as the high performance controllers failed due to saturation of the control input, resulting in failure of the active damping. The results presented in table 9.2, show that the tracking performance of the piston velocity, is increased by a factor of approximately six, when active damping is utilized in the control structure.

	Simulated velocity error (e_{rms})	
Controller	Conservative	High performance
Positive velocity	15.4 mm/s	2.5 mm/s
Negative velocity	8.0 mm/s	1.3 mm/s

Table 9.2. Simulated velocity error when applying the quintic trajectory, using both the conservative controllers, from sections 7.1 and 7.2, and the high performance controllers, obtained in section 7.3

Due to poor quality of the velocity feedback (elaborated below), only the conservative controllers are discretized, by bilinear transformation, and implemented in the test setup. To estimate the velocity from the measured position, three differentiation methods are compared: A differentiating filter and two different methods based on sliding mode algorithms. A second order sliding algorithm, proposed by Schmidt et al. (2013), is selected and implemented, due to the simplicity and quality of the estimate. The noise, present in the position signal, results in poor quality of the velocity estimate, which prevents a successful implementation of the high performance controllers. This is due to the proportional gain, in the PI-controllers, which amplifies the chattering of the velocity feedback, resulting in a chattering control input to the servo drive. The rms value of this chattering control input, due to noise, is 166 rpm, which is unacceptable.

The conservative controller designs are implemented and tested in the laboratory. The measured rms velocity errors obtained, when applying the quintic- and ramp trajectories as reference, are given in table 9.3.

	Measured velocity error (e_{rms})	
Trajectory	Quintic	Ramp
Positive velocity	19.0 mm/s	75.4 mm/s
Negative velocity	12.4 mm/s	46.1 mm/s

Table 9.3. Minimum rms velocity error for the four trajectories with corresponding controller.

The poor tracking of the ramp trajectory, compared to the quintic, is caused by the different demands. The quintic trajectory is designed with a smooth velocity command and finite acceleration, while the ramp trajectory is designed to require infinite acceleration. It is concluded from the experimental results, that the control systems are able to track the trajectories, but the performance is poor due to low closed loop bandwidths.

Prior to experimental tests, the controllers were evaluated in the simulation model. Here it was shown that the performance can be increased by a factor of six, when utilizing the high performance controllers, compared to the conservative controllers. Provided that a good velocity estimate can be obtained, or a velocity sensor is mounted in the test setup, it is expected that results, similar to those obtained in the simulation model, can be obtained in the laboratory. If this hypothesis is true, the velocity rms error can be reduced to 2-3 mm/s, which is considered good tracking performance. It is thereby concluded that the SvDP-concept can be an alternative to the traditional valve-cylinder configuration.

Perspectives of the SvDP-concept 10

In this chapter, perspectives of the SvDP-concept are discussed. Initially, in section 10.1, suggestions are made for improving the the test facilities, such that the potential of the system, with the high performance control, can be verified in by experimental results. This is followed by a discussion, in section 10.2, of the perspectives and the application of the SvDP-concept in its current design. Finally, in section 10.3, a suggestion for improving the SvDP-concept is presented. The suggestion is made based on the experience, obtained through analysis of the system properties in steady state and the dynamic characteristics.

10.1 Improvements of the Test Facility

To validate and evaluate the potential of the SvDP-concept, though test with the high performance controllers, improvements of the test setup are needed:

10.1.1 Improved Velocity Estimation or Installation of Velocity Sensor

As discussed in section 8.2 on page 96, the piston velocity is estimated using a noisy position signal, presumably due to a signal splitter. This leads to a noisy velocity estimate, making an unfiltered proportional gain impossible to implement. By improving the position measurement, i.e. removing the noise, a better velocity estimate could be obtained. Alternatively, a dedicated speed sensor could be implemented to directly obtain the piston velocity. This would enable implementation of the high performance controller utilizing pressure feedback, reviewed in section 7.3.

To assess the potential performance of the system with a proper velocity estimate, the simulation results of the high performance controllers are compared to the simulations of the conservative controllers. Experimental results for the conservative controllers are also available. A comparison of the simulated performance, of the high performance controllers and the conservative controllers, is shown in table 10.1 on the next page.

	Simulated velocity error (e_{rms})	
Controller	Conservative	High performance
Positive velocity	15.4 mm/s	2.5 mm/s
Negative velocity	8.0 mm/s	1.3 mm/s

Table 10.1. Simulated velocity error when applying the quintic trajectory, using both the conservative controllers, from sections 7.1 and 7.2, and the high performance controllers, obtained in section 7.3

Assuming that the performance of the actual system has the same drop in performance, as when implementing the conservative controllers, an expected performance can be calculated based on the experimental results shown in table 9.3 on page 109. This yields an expected performance when implementing the high performance controller, using a quintic trajectory, of approximately 3.1 mm/s and 2.0 mm/s for the positive and negative controller, respectively. With an improved velocity signal, this hypothesis can be tested and the tracking performance validated.

10.2 Perspectives of the current Design

10.2.1 Altered Displacement/Area Ratio

In the system, examined in this thesis, the displacement ratio δ and the area ratio α, are intended to be matched. However, the analysis of the system reveals that the system behaves as if the two ratios are mismatched, yielding a system where the pressure rises during negative velocity, while the pressure drops during positive velocity. As outlined in section 3.1 on page 23, the behavior of the system corresponds to a system where $\delta > \alpha$, even though δ and α are almost intended to be equal. This means that the system may be sensitive to minor changes in the piston area or pump displacement/efficiency. If one pump is worn faster than the other, the α/δ-ratio may be altered, such that the performance of the system is altered drastically. Worst case scenario, the ratios change such that $\delta < \alpha$, resulting in increasing pressure levels in the oppesite direction of motion, compared to the system for which controllers are designed. This could lead to instability and failure of the system.

In order to guarantee that the system behavior is consistent, the α/δ-ratio could be intentionally mismatched. This would yield a similar performance as the current system, however, a thorough analysis of the system would not be required to determine the performance of the system. This means that the system can be intentionally designed such that the pressure increases when traveling in a certain direction, and the pressure decreases in the other direction. The two configurations are outlined below:

- $\delta < \alpha$
    - Positive velocity $\rightarrow$ Increasing pressure
    - Negative velocity $\rightarrow$ Decreasing pressure

- $\delta > \alpha$
  - Positive velocity $\rightarrow$ Decreasing pressure
  - Negative velocity $\rightarrow$ Increasing pressure

A system with a mismatched α/δ-ratio yields better performance in one direction, as described in this thesis. This could be desired in a system which performs a task which requires high tracking performance in one direction, while the performance of the system in the other direction does not matter. A system which could have similar performance requirements could be a manipulator in an industrial automation system, where the requirements of the tracking performance on a return route could be low.

10.3 Suggestion for Improving the SvDP-concept

10.3.1 Increased Virtual Tank Pressure

From analysis and tests with the SvDP-concept, it is found that the tracking performance can be increased considerably by increasing the minimum pressure of the system. In the following it is discussed how an increased virtual tank pressure can raise the minimum pressure. The consequence of increased virtual tank pressure can not be determined in general without further analysis, but an example is given, based on the test setup utilized throughout this thesis. The advantage and disadvantage of modifying the virtual tank pressure are listed below. These statements are based on an analysis carried out on the test setup. The analysis is given after the advantage and disadvantage of modifying the virtual tank pressure:

- **Advantage of Increasing the Virtual Tank Pressure:**
  The system can be dimensioned for a minimum steady state pressure in the two chambers, which alters the minimum eigenfrequency of the hydro-mechanical system. Chosen wisely, the minimum eigenfrequency of the hydro-mechanical system, at positive- and negative velocity, can be matched, such that only one control strategy is needed to obtain an acceptable tracking performance of the system.

- **Disadvantage of Increasing the Virtual Tank Pressure:**
  Re-design of pumps: The low pressure side of the external gear pumps, need to be re-designed, such that a higher suction pressure can be handled. In the current design, the low pressure side can not exceed 3 bar. Presumably because a higher pressure will press the gasket into the pump, causing failure. This problem need to be solved before increasing the virtual tank pressure above 3 bar.

To illustrate and clarify the consequences of increasing the virtual tank pressure, an analysis is carried out. The analysis is carried out based on the properties of the test setup.

Example with SvDP-concept where $\delta > \alpha$

This example is given based on the properties of the test setup at steady state piston velocity. This yields the governing force balance given in equation (10.1), which is utilized throughout the example. The terms collected in the parameter F_L, are denoted the load acting on the piston.

$$\underbrace{F_g + B_v \cdot \dot{x}_p + F_c}_{F_L} = A_p \cdot (p_p - \alpha \cdot p_r) \tag{10.1}$$

The system analysis is divided into two cases: positive- and negative servo speed. In each case, the hydraulic diagram of the system, given in figure 2.1 on page 5, is simplified to only include the active check valves. The overpressure valves are assumed inactive and the proportional valves are neglected, as these are considered inactive. The consequences of changing the magnitude of the virtual tank pressure (VTP), are elaborated in the following. The VTP is adjusted by the crack pressure of the spring loaded check valves.

- **Positive servo speed:**
  At positive servo speed, the hydraulic diagram is given in figure 10.1, which only includes valves that are/might be active. Activation of the anti cavitation valve, with the flow denoted Q_{p2}, depends on the magnitude of the load F_L. The remaining valves are always active and the flow directions are illustrated with the arrows.

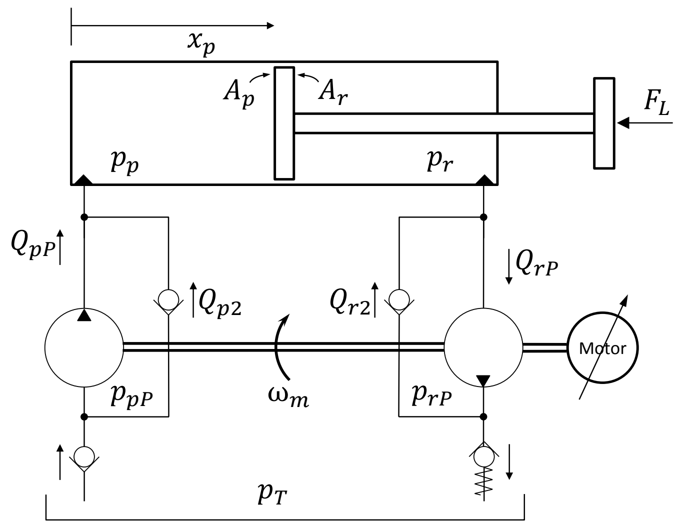

Figure 10.1. Hydraulic diagram of active components in the system at positive servo speed.

Assuming the anti cavitation system is inactive i.e. the flow $Q_{p2} = 0$, the condition $\delta > \alpha$ results in $Q_{pP} < \frac{Q_{rP}}{\alpha}$. This means that the weighted pump flow balance in the system is negative, as a greater flow is pumped out- than in to the system. This results in decreasing chamber pressures. When reaching tank pressure in the piston side chamber, the flow rate $Q_{p2} \neq 0$ and balances the weighted flow, such that p_p settles at the tank pressure. This consideration is made under the assumption that all the rod side flow goes to tank i.e. the crack pressure of the spring loaded valve is exceeded and $Q_{r2} = 0$.

The crack pressure of the spring loaded valve guarantees a minimum pressure in the rod side p_r, as the flow $Q_{r2} \neq 0$ if the crack pressure is not exceeded, resulting in a pressure build up, which results in the crack pressure being reached.

The guaranteed minimum pressure in the rod side p_r is increased, by increasing the crack pressure of the spring loaded valve i.e. the virtual tank pressure at the rod side p_{rP}. With a guaranteed minimum of p_r, the minimum pressure at the piston side can be determined by rearranging equation (10.1):

$$p_p = \frac{F_L}{A_p} + \alpha \cdot p_r \tag{10.2}$$

From equation (10.2), the piston side pressure can be determined. Assuming steady state of the system, at constant positive velocity, the rod side pressure is constant at the crack pressure. Thereby, the minimum piston side pressure can be determined from the minimum load acting on the system, using equation (10.2).

Example with the test setup: The minimum load, acting on the piston in the test setup, occurs at the position $x_p = 750$ mm, where the combined gravitational force and Coulomb friction is -200 N at positive velocity (shown in figure 2.11 on page 18). The minimum viscous friction is obtained at $\dot{x}_p = 0$, resulting in the minimum $F_L = -200$ N. In table 10.2, the minimum steady state pressures, in the test setup, are tabulated for different virtual tank pressures at rod side i.e crack pressure of the spring loaded valve. If the operation point is changed, it results in an increased p_p e.g. if the piston speed is increased, or the load becomes pushing.

	Virtual tank pressure at rod side			
Minimum p_r / Crack pressure	2.5 bar	5 bar	10 bar	20 bar
Minimum steady state p_p	0.93 bar	2.18 bar	4.68 bar	9.68 bar

Table 10.2. Minimum pressures at steady positive velocity (in the test setup).

In the test setup, the crack pressure is set to 2.5 bar, which can result in cavitation, as seen in table 10.2, where the minimum p_p is lower than the tank pressure of 1 bar. If the crack pressure can be increased (different or re-designed gaskets for the pumps), the minimum steady state pressure is increased, resulting in increased stiffness of the hydro-mechanical system. This results in an increased eigenfrequency of the system, at positive velocity, increasing the achievable bandwidth of the closed loop control system. This is illustrated in figure 10.2, where the linear system G_p^+ is evaluated using the virtual tank pressure (VTP) at rod side listed in table 10.2. The system is linearized around a servo speed of 250 rpm ($\dot{x}_p = 15.6$ mm), as this is the lowest speed for which pump data is available (elaborated in section 5.2). The linear characteristics of the system at positive velocity and at the different virtual tank pressures, are compared with the system at the critical operation point for negative velocity G_{s11}^- in figure 10.2 on the following page.

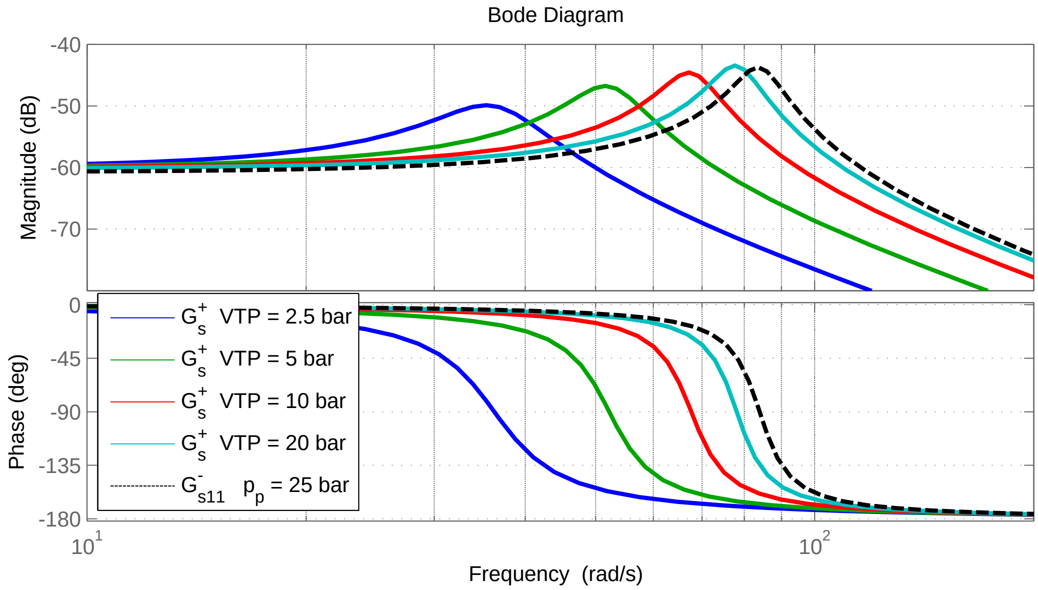

Figure 10.2. Bode diagram of G_s^+ with varying Virtual Tank Pressures (VTP) at the rod side. G_{s11}^- from figure 7.25 on page 88 is included for comparison.

In figure 10.2, it is seen that the eigenfrequency of G_s^+, is increased significantly, by increasing the guaranteed minimum pressure at the rod side i.e. increasing the crack pressure of the spring loaded check valve. When VTP = 20 bar, the characteristics of the system, at positive- and negative velocity, are almost the same. Thereby one set of controllers can be designed for controlling the system, throughout the entire operation range, instead of switching controller depending on direction of movement. The steady state gains of the two systems, are almost identical, as δ and α are almost matched. If this is not the case, the gain will dependent on the motion direction.

Increasing the VTP at the rod side therefore results in an increased eigenfrequency of the system at positive velocity and thereby an increased achievable closed loop bandwidth. The gain of the piston side pressure can not be determined without knowing the load acting on the piston. It should therefore be noted that the results presented here, only applies to the specific test setup, provided for experiments during this dissertation and can not be generalized. The minimum pressure at the piston side is dependent on the load and the area ratio, as shown in (10.2), and is only the guaranteed minimum pressure during steady state. It can be noted though, that this correlation can be utilized in a dimensioning process for obtaining a guaranteed minimum pressure at steady velocity.

- **Negative servo speed:**
  For negative servo speed, the hydraulic diagram is given in figure 10.3 on the next page, which only include valves that are/might be active. Activation of the check valve, with the flow denoted Q_{p2}, depends on the chamber pressure and the crack pressure of the spring loaded valve. The remaining valves are always active and the flow directions are illustrated with the arrows.

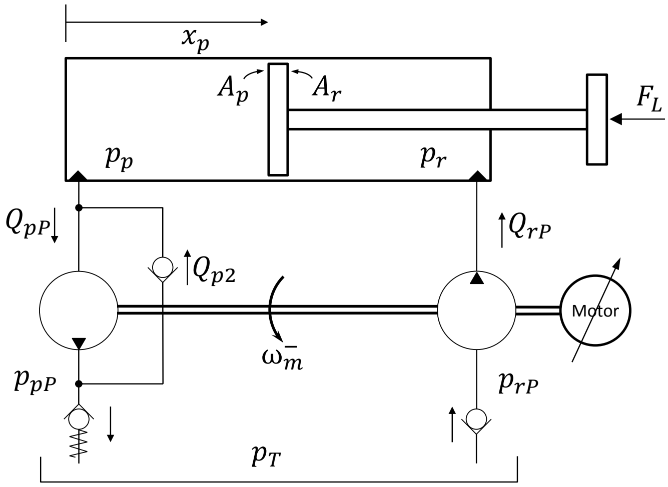

Figure 10.3. Hydraulic diagram of active components in the system at negative servo speed.

With $\delta > \alpha$ the pump flow $Q_{pP} < \frac{Q_{rP}}{\alpha}$, using the sign convention in figure 10.3. This means that the weighted pump flow balance in the system is positive, as a greater flow is pumped into than out off the system. This causes the pressure in the system to increase. The spring loaded valve at the piston side only determines the minimum pressure of p_p at steady velocity. Since the pressure is always increasing, the magnitude of the virtual tank pressure does not contribute with any advantages in the case where the velocity is negative. Despite this, it could be an advantage to set the VTP at the piston side equal to the VTP at the rod side. Doing this, the system may still be stable even if the the δ/α-ratio changes during operation, due to wear and tear of the pumps. To guarantee this, the system must be analyzed further.

The results, obtained throughout this example, can be applied to the case where $\delta < \alpha$ by substituting positive- with negative servo speed i.e. the results for positive servo speed becomes the results for negative servo speed and visa versa. This was shown in section 10.2.

Bibliography

Andersen, 2003. Torben Ole Andersen. *Fluid Power Systems - Modelling and Analysis.* Institute of Energy Technology - 2nd edition, 2003.

Bertelsen and Madsen, 2013. Dennis Bertelsen and Thomas H. Madsen. *Development of an Servo variable Differential Pump (SvDP)-Concept.* Master's thesis, Aalborg University, 2013.

Glad and Ljung, 2010. Torkel Glad and Lennart Ljung. *Control Theory - Multivariable and Nonlinear Methods.* CRC Press - Taylor & Francis Group, 2010.

Levant, 2003. Arie Levant. *Higher-Order Sliding Modes, Differentiation and Output-Feedback Control.* International Journal of Control, 2003.

Philips and Parr, 2011. Charles L. Philips and John M. Parr. *Feedback Control Systems 5. edition.* Pearson Education Inc., 2011.

Rexroth, 2006. Bosch Group Rexroth. *Check valve - Type S.* RE 20375/12.06, 2006.

Rexroth, 2012. Bosch Group Rexroth. *External Gear Pumps Series F - Type AZPF-...* RE 10 089/02.12, 2012.

Rexroth, 2009. Bosch Group Rexroth. *Wirkungsgrad 3Pumpen 12 Drehzahlen mit Streubereichen-14ccm-50°.* Last modified: 22-07-2009, 2009.

Rexroth, 2010. Bosch Group Rexroth. *Wirkungsgrad AZPF28cm*^{3}*-50° C-v6.* Last modified: 27-10-2010, 2010.

Rexroth, 2005. Bosch Group Rexroth. *2/2 proportional directional valve, direct operated - Type KKDS (High-Performance).* RE 18139-06/06.05, 2005.

Rexroth, 1998. Mannesmann Rexroth. *Pressure Relief Valve, Direct Operated Model DBD (Series 1X).* RA 25 402/06.98, 1998.

Schmidt, 2013. Lasse Schmidt. *Robust Control of Industrial Hydraulic Cylinder Drives - with Special Reference to Sliding Mode- & Finite-Time Control.* PhD thesis - Aalborg University, 2013.

Schmidt, Andersen, and Pedersen, 2013. Lasse Schmidt, Torben O. Andersen, and Henrik C. Pedersen. *Robust Non-Chattering Observer Based Sliding Control Concept for Electro-Hydraulic Drives.* The International Federation of Automatic Control, 2013.

Skogestad and Postlethwaite, 2001. Sigurd Skogestad and Ian Postlethwaite. *Multivariable Feedback Control - Analysis and Design, 2^{nd} edition.* John Wiley & Sons, 2001.

Appendices

Parameters of the SvDP-concept A

Description	Symbol	Value	Unit
Manipulator parameters:			
Piston area ratio	α	0.5	[-]
Area of the piston side in the cylinder	A_p	6.2e-3	$[m^2]$
Area of the rod side in the cylinder	A_r	3.1e-3	$[m^2]$
Stroke length of cylinder	L_c	863e-3	$[m]$
Viscous friction coeff. at positive velocity	B_v^+	9.9e3	$[Ns/m]$
Viscous friction coeff. at negative velocity	B_v^-	19.8e3	$[Ns/m]$
Coulomb friction coefficient	F_c	450	$[N]$
Leakage coefficient at piston side	C_{pLeak}	2.25e-12	$[m^3/s \cdot Pa]$
Leakage coefficient at rod side	C_{rLeak}	0.24e-12	$[m^3/s \cdot Pa]$
Hose volume of the piston side lines	V_{pline}	1.11e-3	$[m^3]$
Hose volume of the rod side lines	V_{rline}	1.11e-3	$[m^3]$
Parameters of pumps and servo drive:			
Pump displacement ratio ($\eta_v = 1$)	δ	0.52	[-]
Displacement of piston side pump	D_p	28e-6	$[m^3/rev]$
Displacement of rod side pump	D_p	14.7e-6	$[m^3/rev]$
Natural frequency of servo drive	$\omega_{n,m}$	100	[Hz]
Damping ratio of servo drive	ζ_m	0.35	[-]
Parameters of the valves:			
Pressure relief valve flow gain	k_{PRV}	166.7e-6	$[m^3/s \cdot Pa]$
Pressure relief valve time constant	τ_{PRV}	2.0e-3	$[s]$
Crack pressure of PRV	p_{crack}	200e5	$[Pa]$
PDV time constant	τ_{PDV}	16e-3	$[s]$
Check valve flow gain	k_{CV}	13.2e-6	$[m^2 \cdot \sqrt{m^3/kg}]$
Check valve time constant	τ_{CV}	1.0e-3	$[s]$
Crack pressure of spring loaded CV	p_{spring}	2.5e5	$[Pa]$
Fluid parameters:			
Stiffness of pure oil	β_F	5000e5	$[Pa]$
Volumetric ratio of air content in the fluid	η_A	0.5	[%]
Adiabatic constant of air	c_{ad}	1.4	[-]
Atmospheric pressure	p_{atm}	1.0e5	[Pa]

Table A.1. Parameters and constants used to model the SvDP-concept.

Experiments for Validation of the Simulation Model B

In this chapter, a brief description of the test setup is given. Furthermore, the experiments, performed to validate the simulation model, are presented. The measurements obtained during these experiments are also reviewed.

B.1 Description of the Test Setup

The experimental test setup consists of the components listed below:

- Outer link of a backhoe loader
- Servo motor driving the pumps
- Hydraulic circuit - SvDP-concept
- PLC to control the servo drive
- PLC for data acquisition

An overview of the system configuration is provided in figure B.1, where a schematic of the system is given to the left. To the right, an illustration of the outer link of the backhoe loader is given.

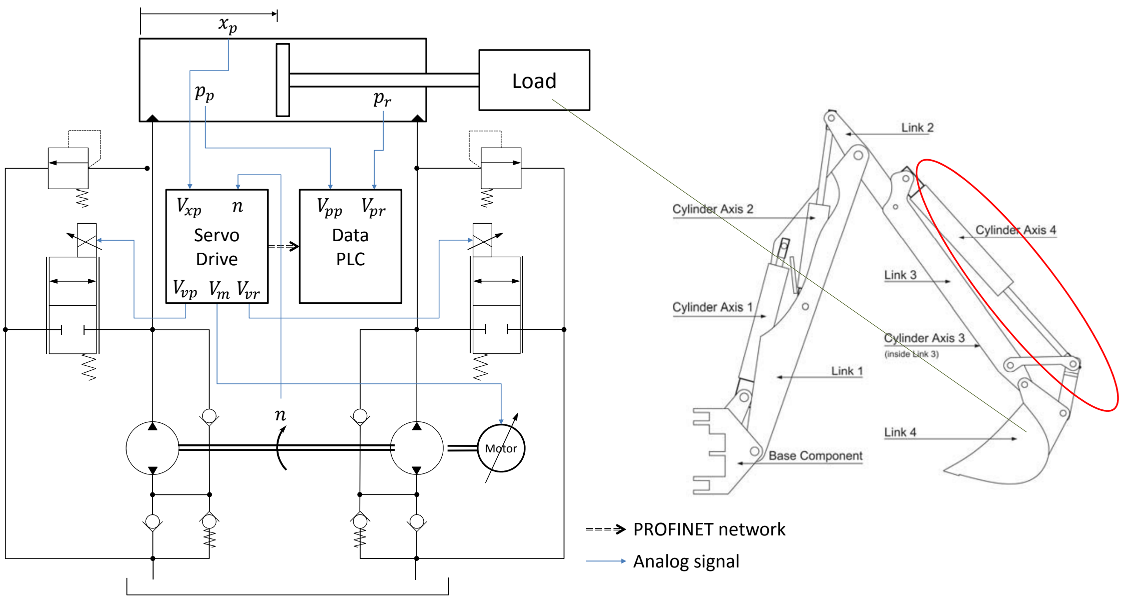

Figure B.1. Schematic overview of the test setup utilized in the laboratory.

The blue lines, in figure B.1 on the previous page, illustrate the analog signals, while the dashed line illustrates a PROFINET network signal. In the test setup, sensors are available for measuring the pressure levels, denoted p_i and the piston position x_p. The signals denoted V_{xx}, indicates that the signal is a voltage signal.

The backhoe loader contains four cylinders, where cylinder 4 is utilized as load for the hydraulic circuit. The servo drive PLC is provided by Bosch Rexroth and is utilized to control the servo motor. This PLC is a standard setup for controlling servo motors. The PLC contains all the control structures, required to drive an AC motor. The servo drive PLC has an internal loop running at 8 kHz, which controls the servo motor, whereas the control loop for controlling the hydraulic components runs at 1 kHz.

The Data PLC was originally utilized to control the backhoe loader, when utilizing the "classic" valve configuration of the backhoe loader (Bertelsen and Madsen, 2013). In this project the PLC is designated to data acquisition. The PLC receives data from the servo drive PLC via the PROFINET network, established between the two PLCs. In addition to the equipment described above, two PCs are required to communicate with the two PLCs.

In the following sections, the experiments preformed on the test setup are documented. These tests are used to establish- and validate the nonlinear simulation model in chapter 2.

B.2 Estimation of Servo Drive Dynamics

As described in section 2.1.4 - equation (2.15) on page 12, the dynamics of the servo drive, driving the pumps, is approximated by a second order system. This yields two parameters, which have to be determined; the natural frequency of the servo system, $\omega_{n,m}$ and the damping ratio, ζ_m. The system response is acquired by applying steps in the interval $\pm[100\ ,\ 300]$ rpm as the reference speed for the motor and then measure the actual motor speed. The measurements are shown in figure B.2 on the facing page.

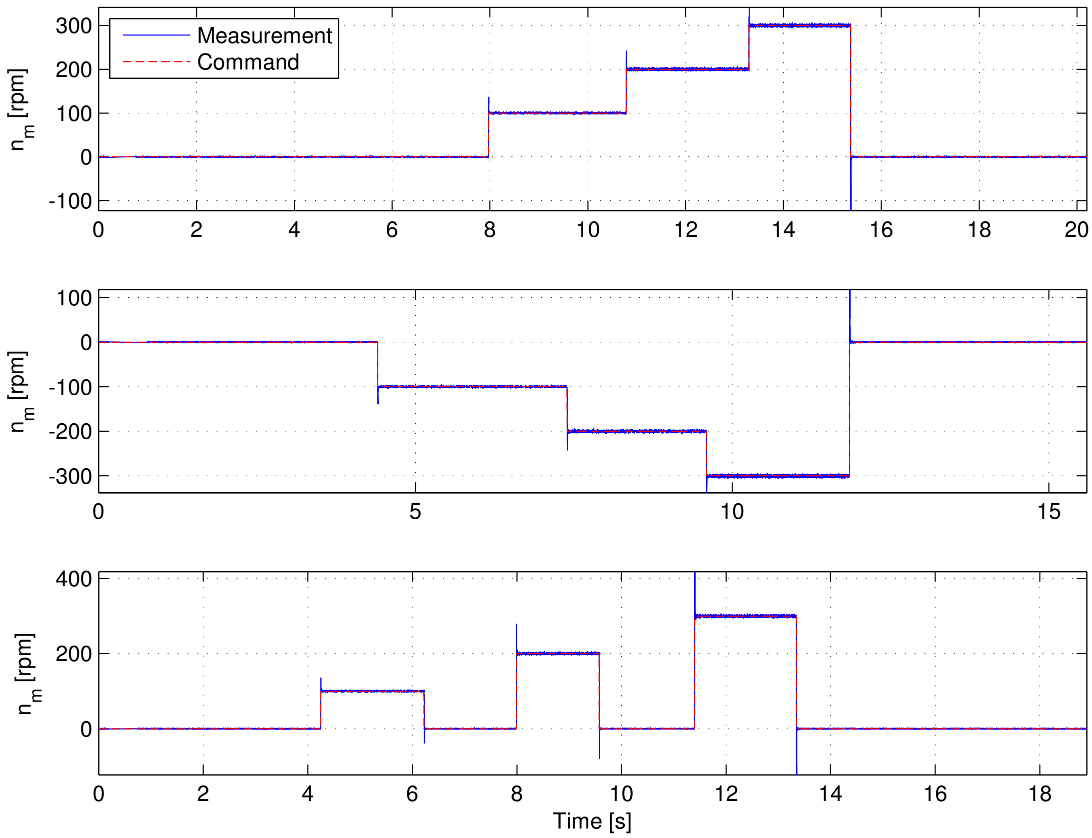

Figure B.2. Measurements of the servo drive response, when applying steps as reference speed.

To compare the measured step responses and obtain an approximation of the dynamics, the measurements are normalized. The result of the normalization is given in figure B.3, along with an approximation of the dynamic. The dynamics are approximated by a second order system.

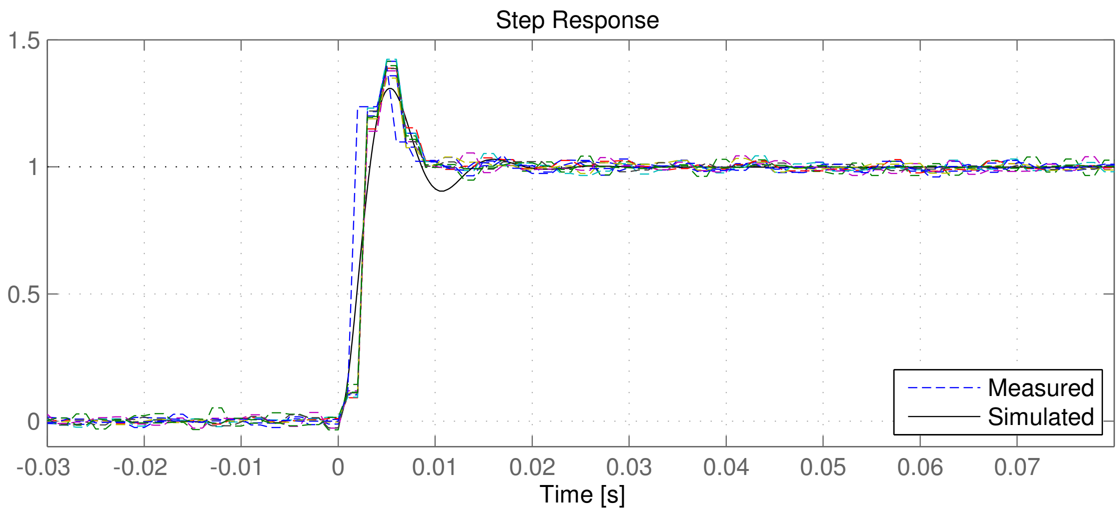

Figure B.3. Normalized measured responses of the servo drive along with the simulated response, obtained from the fitted transfer function.

The simulated response, shown in figure B.3 on the preceding page, is obtained by applying a unit step to a the second order transfer function. The parameter values are listed in table B.1.

Parameter	Value
$\omega_{n,m}$	100 [Hz]
ζ_m	0.35 [-]

Table B.1. Parameters for describing the servo drive dynamic.

As seen in figure 2.10 on page 17, the simulated response has a slightly larger undershoot than the measured responses, however, the approximation is assessed as a sufficient representation of the servo drive dynamic.

B.3 Determination of Gravitational Load and Coulomb Friction

The purpose of this test is to determine the external forces, such that a mathematical description of the forces acting on the piston can be obtained. The external forces of interest, in this experiment, are the gravitational force and the Coulomb friction. The piston is actuated as steady and slowly as possible, in order to minimize the effects of viscous friction and acceleration of inertia load. The gravitational force and the Coulomb friction are determined by measuring the pressures in the two chambers and calculating the equivalent force acting on the piston. This can be seen from equation (2.1) on page 6, which is repeated here for clarity:

$$\underbrace{M_{eq} \cdot \ddot{x}_p + B_v \cdot \dot{x}_p}_{\approx 0} + F_c + F_{ext} = A_p \cdot p_p - A_r \cdot p_r \tag{B.1}$$

When the piston acceleration and velocity are low, equation (B.1) shows that:

$$A_p \cdot p_p - A_r \cdot p_r \approx F_c + F_{ext}, \tag{B.2}$$

Assuming that the external force F_{ext} is only given by the gravitational force F_g, the gravitational force can be determined from the measured chamber pressures. The results of two experiments, performed with the lowest possible piston velocity, are shown in figure B.4 on the next page. One experiment is performed with positive velocity and one with negative. In figure B.4, the measured pressures are given. p_p denotes piston side pressure and p_r denotes the rod side pressure.

As seen in figure B.4 on the facing page, two measurements are made: one in each motion direction. Furthermore, it can be seen that nonlinear friction occurs when the velocity is positive i.e. $x_p \rightarrow L_c$, resulting in pressure oscillations.

Equation (B.2) is utilized to determine the gravitational force of the load. This results in two curves, shown in figure B.5 on the next page.

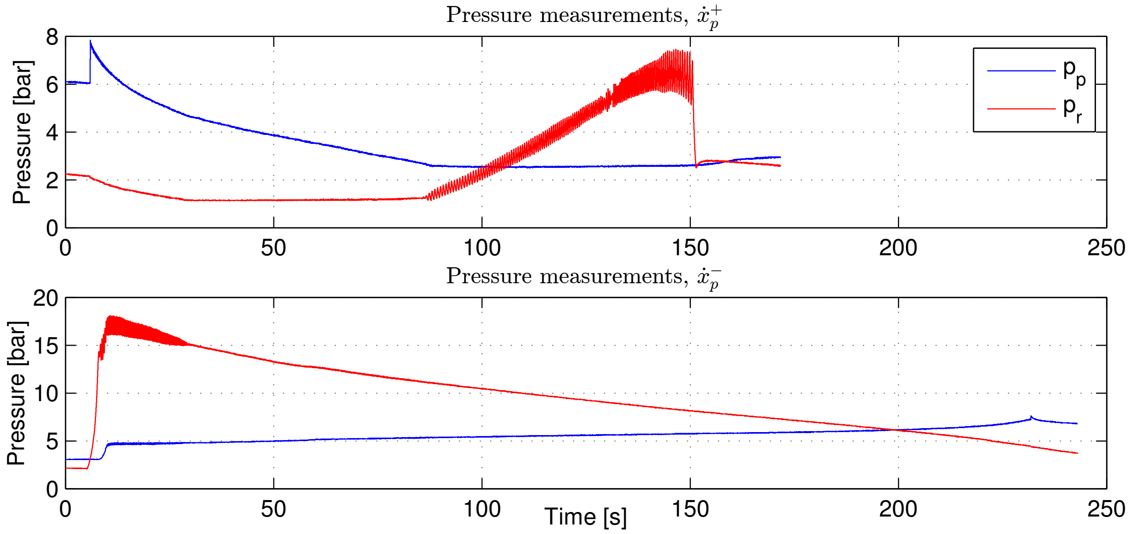

Figure B.4. Measured pressure levels obtained by actuating the piston at low steady speed, such that acceleration of the inertia load and the viscous friction are negligible in the force balance. In the top, measurement are given for a positive velocity. In the bottom, measurement of the pressures are given for a negative velocity.

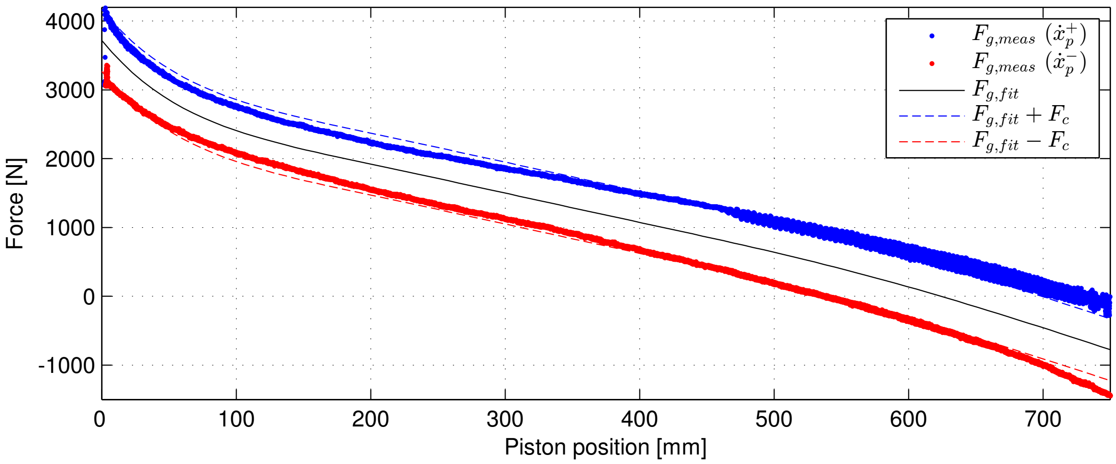

Figure B.5. Gravitational load in both directions obtained from measurements given in figure B.4, along with the fitted polynomial describing the gravitational load.

The gravitational load is determined by fitting a 7th order polynomial with the two data sets. The two data sets are weighted using the time difference apparent in figure B.4, in order to center the fitted polynomial. The fitted polynomial is given in equation (2.21) on page 18. The Coulomb friction is determined as half of the difference between the two curves resulting in $F_c = 450$ N. Hereby, a mathematical description of the gravitational load is obtained and the Coulomb friction is determined.

B.4 Measurements for Validation of Complete Simulation Model

In order to validate the complete simulation model, two tests are performed: One test, where steps of ±2250 rpm are applied as reference speed to the servo drive and another test, where steps of ±1000 rpm are applied. In both tests, the position of the piston is sampled along with the pressure level of the two chambers. Furthermore, the rotational velocity of the servo drive is measured.

Test case # 1 - step ±2250 rpm

In this test, steps of ±2250 rpm are applied as reference speed to the servo drive. The initial piston position is 750 mm, where a negative step is given such that the piston position goes towards 0 mm. After 2 seconds a positive step of 2250 rpm is applied. During the test, the piston is positioned in the interval 400-750 mm, providing significant parameter variations, such that the simulation model can be validated. A comparison and adjustment of the simulation model is performed in section 2.2, using the measurements illustrated in figure B.6.

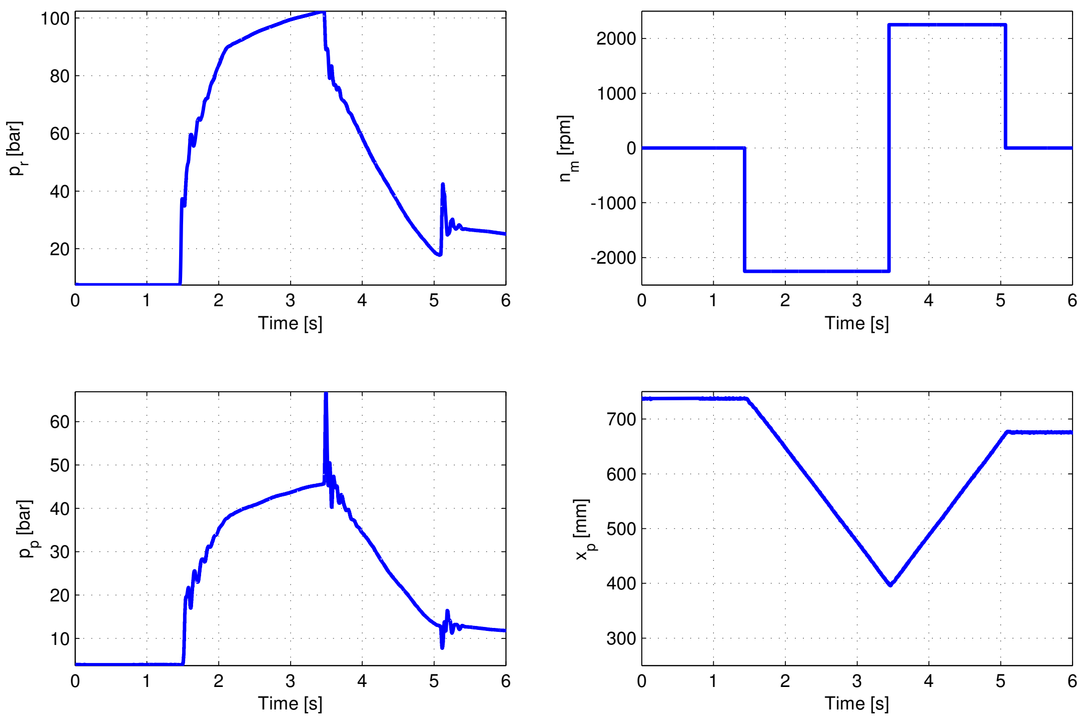

Figure B.6. Measurements obtained when applying steps of ±2250 rpm as reference speed to the servo drive. (Top left): Rod side pressure (Top right): Servo motor command (Bottom left): Piston side pressure (Bottom right): Piston position

Test case # 2 - step ±1000 rpm

During this test, steps of ±1000 rpm are applied as reference speed to the servo drive. The initial piston position is 620 mm, where a negative step is given such that the piston moves towards 0 mm. After 5.5 seconds, a positive step of 1000 rpm is applied. During the test, the piston is in moving in the interval 250-620 mm, which also provides significant parameter variations for validation of the simulation model. The comparison and adjustment of the simulation model is performed in section 2.2, using the measurements illustrated in figure B.7.

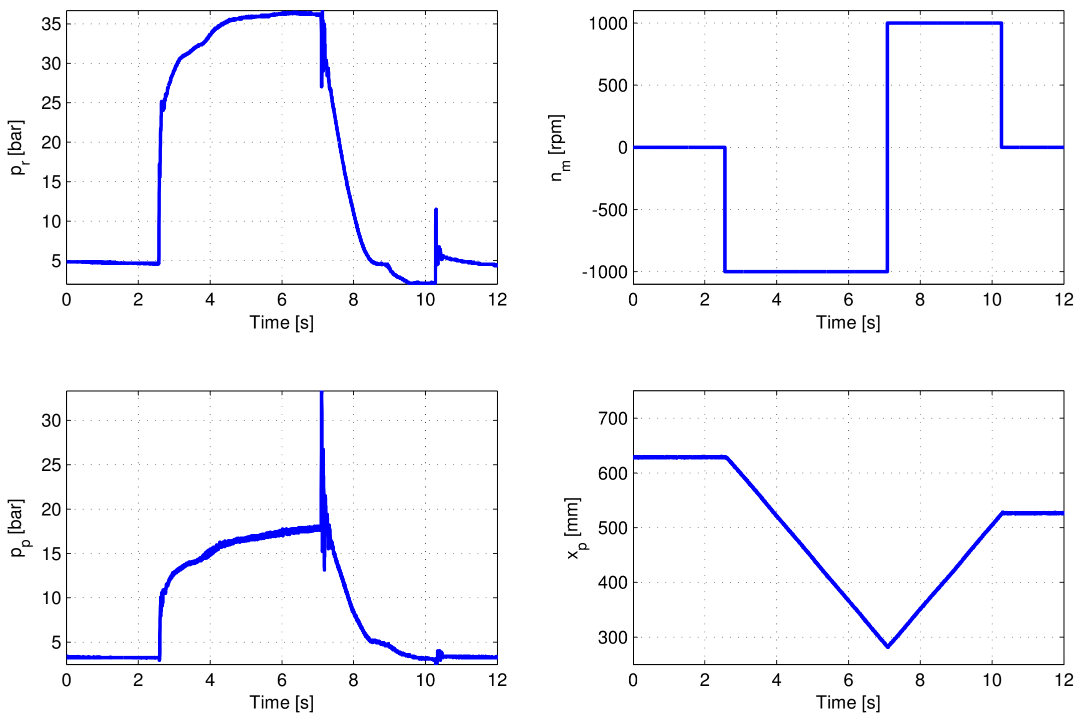

Figure B.7. Measurements obtained when applying steps of ±1000 rpm as reference speed to the servo drive. (Top left): Rod side pressure (Top right): Servo motor command (Bottom left): Piston side pressure (Bottom right): Piston position

This concludes the tests, performed to validate and adjust the simulation model in section 2.2.

Derivation of Linear Model C

The model of the SvDP-concept contains several nonlinear terms. This appendix provides a derivation of how the nonlinear model is linearized, such that a linear model is obtained. The linear model is reviewed in chapter 5, where it is used for analysis of the system characteristics. Initially, an analysis is performed to show that the inertia load and bulk modulus should be considered constant when linearizing the system.

C.1 Linearization of Inertia Load & Bulk Modulus

Prior to linearizing the system, it is investigated how to deal with composite functions during linearization of the system. Recall that the force balance of the cylinder, given in equation (2.1) on page 6, is a function of the inertia load $M_{eq}(x_p)$, which is a function of the piston position. $M_{eq}(x_p)$ is shown in figure 2.9 on page 16, where it is evident that the gradient dM_{eq}/dx_p is rather high towards the end positions. Similar circumstances apply to the continuity equations (2.5) and (2.6) on page 7. These depend on bulk modulus $\beta(p)$, which is a function of the pressure level. In figure 2.7 on page 15 is was shown that the gradient $d\beta/dp$ is relatively high at low pressure. It is therefore expected that these gradients have significant influence on the system characteristics and should be included in the linear model. This is investigated in the following.

For transparency, in the characteristics of the system, a simplified system is analyzed. The system consists of a cylinder with one chamber connected to a pump and an inertia load. An illustration of the system is given in figure C.1.

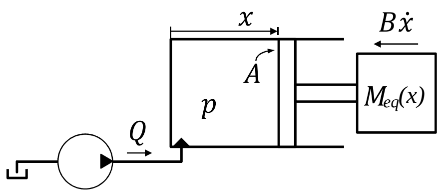

Figure C.1. Schematic of the simplified hydraulic system.

The only friction present in the system is viscous friction. The governing equations of the system are given by the force balance, equation (C.1) and the continuity equation (C.2).

$$M(x) \cdot \ddot{x} = A \cdot p - B \cdot \dot{x} \tag{C.1}$$

$$D \cdot \omega - A \cdot \dot{x} = \frac{V}{\beta(p)} \cdot \dot{p} \tag{C.2}$$

Considerations on Linearization of Inertia Load

Initially, the force balance is considered, where the position dependent inertia load is chosen equal to the one of the backhoe loader, shown in figure 2.9 on page 16. Here it is shown, that the gradient of the inertia load changes sign throughout the operating range of the piston and has a relatively large amplitude at the end positions. A derivation of the linear force balance is given below. When taking the partial derivative of the force balance, with respect to the position x, the chain rule is applied, as the inertia load is a function of the position. The notation $_0$ means that the partial derivatives are evaluated at a given operation point. Finally the linear equation is Laplace transformed in equation (C.3), assuming zero initial conditions.

$$
\begin{aligned}
M(x) \cdot \ddot{x} &= A \cdot p - B \cdot \dot{x} \\
&\Downarrow \text{Linearization} \\
\Delta\ddot{x} &= \left.\frac{\partial f}{\partial p}\right|_0 \cdot \Delta p + \left.\frac{\partial f}{\partial \dot{x}}\right|_0 \cdot \Delta\dot{x} + \left.\frac{\partial f}{\partial x}\right|_0 \cdot \Delta x \\
&\Downarrow \\
\Delta\ddot{x} &= \frac{A}{M(x_0)} \cdot \Delta p - \frac{B}{M(x_0)} \cdot \Delta\dot{x} - \underbrace{\frac{\left.\frac{dM(x)}{dx}\right|_0 \cdot (A \cdot p_0 - B \cdot \dot{x}_0)}{M(x_0)^2}}_{K_m} \cdot \Delta x \\
&\Downarrow \text{Laplace transformation} \\
\dot{x}(s) &= \frac{\frac{A \cdot s}{M(x_0)}}{\left(s^2 + s \cdot \frac{B}{M(x_0)} + K_m\right)} \cdot p(s)
\end{aligned}
\tag{C.3}
$$

The sign of K_m is determined by two terms: the gradient of the inertia load and the sum $A \cdot p_0 - B \cdot \dot{x}_0$. To validate the linear model, an imbalance of $A \cdot p_0 - B \cdot \dot{x}_0$ is generated such that K_m takes positive and negative sign. The linear model is compared with a simulation of the nonlinear model, by applying a step of 1 bar as input to the system. The parameters used for evaluation are listed in table C.1.

x_0	$\dot{x}_0$	p_0	$M(x_0)$	$\left.\frac{dM(x)}{dx}\right\|_0$	A	B
0.05 m	0.2 m/s	[9.3, 10.1] bar	802 kg	$-7.15e3$ kg/m	$6.2e{-3}$ m^2	30 kNs/m

Table C.1. Linearization points and parameters used for validation of linear force balance.

When $K_m = 0$, the force balance reduces to a first order system. The step responses of the linear system, in the three different cases, are given in figure C.2 on the next page together with the nonlinear model.

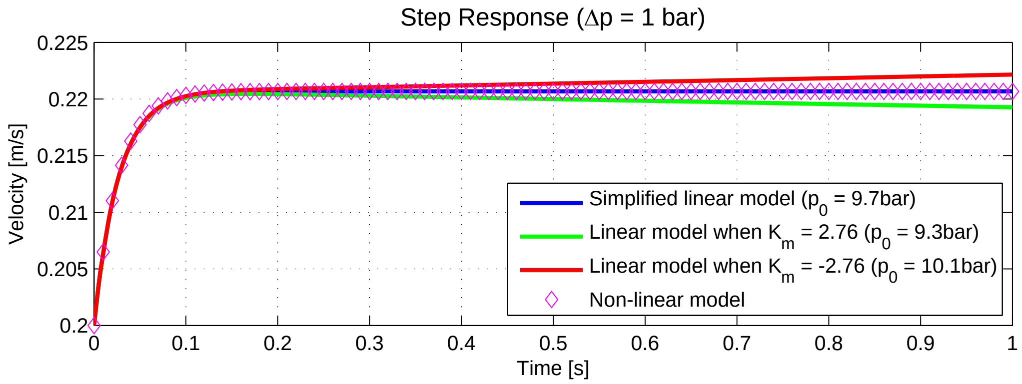

Figure C.2. Step responses when $K_m = 0$, $K_m > 0$ and $K_m < 0$ compared to the nonlinear model.

From figure C.2 it is clear that the linear representation of the system yields a good approximation of the nonlinear model in all cases, during the first 0.2 sec. Hereafter, the linear model starts deviating when $K_m \neq 0$. This means that the linearization is only valid, when the system is very close to the operating point in the cases where $K_m \neq 0$. It is therefore assessed that the position dependent gradient of the inertia load can be omitted in the linear model i.e. $K_m = 0$ and linear force balance is given by equation (C.4).

$$\dot{x}(s) = \frac{\frac{A}{M(x_0)}}{\left(s + \frac{B}{M(x_0)}\right)} \cdot p(s) \tag{C.4}$$

This concludes that a good linear approximation can be obtained by considering the inertia load constant around the linearization point.

Considerations on Linearization of Bulk Modulus

Similarly, the continuity equation from (C.2) is considered, as the bulk modulus is a function of the pressure in the chamber. The continuity equation is linearized below, with respect to the velocity of the piston and pump, along with the pressure to account for the changes in bulk modulus. The Laplace transformed linear equation is given in equation (C.5).

$$
\begin{aligned}
&\frac{V}{\beta(p)} \cdot \dot{p} = D \cdot \omega - A \cdot \dot{x} \\
&\qquad\qquad \Downarrow \text{Linearization} \\
&\Delta \dot{p} = \left.\frac{\partial \dot{p}}{\partial \dot{x}}\right|_0 \cdot \Delta \dot{x} + \left.\frac{\partial \dot{p}}{\partial \omega}\right|_0 \cdot \Delta \omega + \left.\frac{\partial \dot{p}}{\partial p}\right|_0 \cdot \Delta p \\
&\qquad\qquad \Downarrow \\
&\Delta \dot{p} = \frac{\beta_0}{V_0} \cdot (D \cdot \Delta\omega - A \cdot \Delta\dot{x}) + \underbrace{\frac{\left.\frac{\partial \beta}{\partial p}\right|_0 \cdot (D \cdot \omega_o - A \cdot \dot{x}_0)}{V_0}}_{K_\beta} \cdot \Delta p \\
&\qquad\qquad \Downarrow \text{Laplace transformation} \\
&p(s) = \frac{\beta_0}{V_0 \cdot (s - K_\beta)} \cdot (D \cdot \omega(s) - A \cdot \dot{x}(s))
\end{aligned} \tag{C.5}
$$

As seen in equation (C.5), the chamber pressure depends on the piston- and pump velocity at the operation point. The two inputs are applied to a filter with a pole equal to K_β. This means that the linearized system is unstable when K_β is positive. As $d\beta/dp$ is always positive, $A \cdot \dot{x}_0 > D \cdot \omega_0$ is the sufficient condition for a stable filter. To determine the effect of the filter, a simulation is carried out where K_β is included, compared to a linear model where K_β is neglected i.e. bulk modulus is assumed constant. These simulations are compared to the nonlinear model in figure C.3. The parameters and operation points used in the evaluation, are listed in table C.2.

V_0	$\dot{x}_0$	$\dot{\omega}_0$	p_0	$\beta(p_0)$	$\left.\frac{d\beta(p)}{dp}\right\|_0$	A	D
3.1 l	0.08 m/s	1000 rpm	10 bar	4965.1 bar	586.9	$6.2e{-3}$ m^2	28 cm^3/rev

Table C.2. Linearization points and parameters used for validation of linear continuity equation.

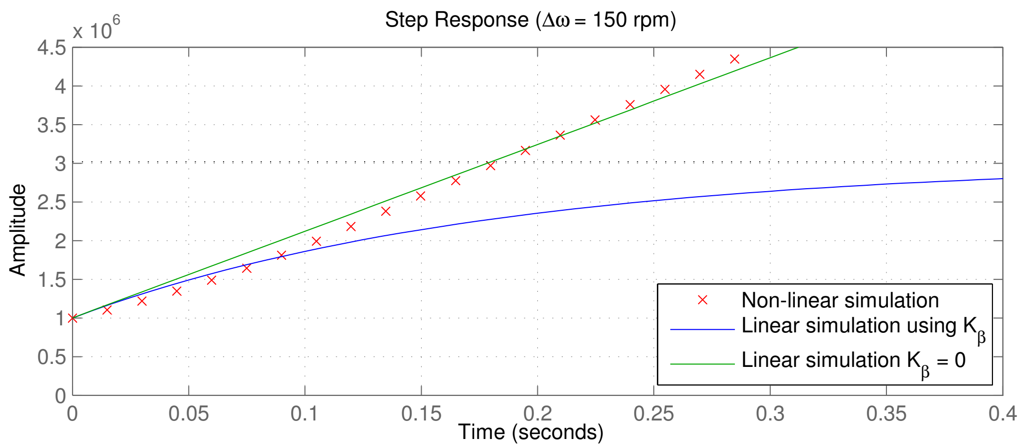

Figure C.3. Step response of the continuity equation, when using K_β and when $K_\beta = 0$, compared to simulation of the nonlinear model.

As seen in figure C.3 on the preceding page, the linear model, which does not utilize K_β, is a more accurate representation of the system. Therefore K_β is disregarded, which means that the gradient of the bulk modulus should be neglected in the linear model. When K_β is zero, the linear system in equation (C.5) reduces to a free integrator with a gain.

The results, showing that bulk modulus and the inertia load should be considered constant in the vicinity of the operation point, are utilized when establishing a linear model of the SvDP-concept in the following.

C.2 Linearization of the Nonlinear Model

In this section, the individual equations in nonlinear model of the SvDP-concept, given in chapter 2, are linearized:

Linear Model of the Piston Force Balance

In equation (C.6), a linear model of the piston force balance is derived. The first equation is from the nonlinear model, equation (2.1) on page 6. Next, the model is linearized by taking the partial derivatives in each variable direction. It should be noted that the equivalent mass is a function of the piston position, but is considered constant in the vicinity of the operation point, in accordance with the result found in section C.1. The partial derivatives are evaluated at an operation point denoted with the subscript $_0$ i.e. the linear force balance is a function of the operation point x_{p0}.

$$
\begin{aligned}
M_{eq}(x_p) \cdot \ddot{x}_p + B_v \cdot \dot{x}_p + F_c + F_{ext} &= A_p \cdot p_p - A_r \cdot p_r \\
&\Downarrow \text{Linearizing model} \\
M_{eq0} \cdot \Delta\ddot{x}_p \approx \left.\frac{\partial f}{\partial p_p}\right|_0 \cdot \Delta p_p &+ \left.\frac{\partial f}{\partial p_r}\right|_0 \cdot \Delta p_r + \left.\frac{\partial f}{\partial \dot{x}_p}\right|_0 \cdot \Delta\dot{x}_p \\
&\Downarrow \text{Linear model} \\
M_{eq0} \cdot \Delta\ddot{x}_p = (A_p \cdot \Delta p_p &- A_r \cdot \Delta p_r - B_v \cdot \Delta\dot{x}_p)
\end{aligned}
\tag{C.6}
$$

Linearization of the Continuity Equation at the Piston Side

The continuity equation at the piston side, given in equation (2.5) on page 7, is repeated in the top of equation (C.7). Applying the system simplifications listed in chapter 5, yields the simplified model in the second line of (C.7), where the PRV is considered inactive along with the anti-cavitation system.

The stiffness of the fluid β_p is a nonlinear quantity, that is a function of the pressure in the control volume. It was shown in section C.1 that linearization of the bulk modulus, with respect to the pressure, does not yield a good approximation of the system and should be considered constant in the vicinity of the operation point p_{p0}. The partial derivatives are then evaluated at a given operation point $_0$. This yields the last equation in (2.5), concluding the linear model of the pressure in the piston side control volume. Note that the coefficient V_{p0} is introduced, which is the chamber volume in the vicinity of the operation point. At the end of this appendix is given a summary of the linear model, where the linear pump- and valve flow are substituted into the continuity equation.

$$\dot{p}_p = \frac{\beta_p\left(p_p\right)}{A_p \cdot x_p + V_{pline}} \cdot \left(Q_{pP} + Q_{p2} - Q_{pV} - Q_{p1} - Q_{pL} - A_p \cdot \dot{x}_p\right)$$

$\Downarrow$ Simplified model

$$\dot{p}_p = \frac{\beta_p}{A_p \cdot x_p + V_{pline}} \cdot \left(Q_{pP} - Q_{pV} - C_{pLeak} \cdot p_p - A_p \cdot \dot{x}_p\right)$$

$\Downarrow$ Linearizing model

$$\Delta\dot{p}_p \approx \left.\frac{\partial f}{\partial Q_{pP}}\right|_0 \cdot \Delta Q_{pP} + \left.\frac{\partial f}{\partial Q_{pV}}\right|_0 \cdot \Delta Q_{pV} + \left.\frac{\partial f}{\partial p_p}\right|_0 \cdot \Delta p_p + \left.\frac{\partial f}{\partial \dot{x}_p}\right|_0 \cdot \Delta\dot{x}_p$$

$\Downarrow$ Linear model

$$\Delta\dot{p}_p = \frac{\beta_{p0}}{V_{p0}} \cdot \left(\Delta Q_{pP} - \Delta Q_{pV} - C_{pLeak} \cdot \Delta p_p - A_p \cdot \Delta\dot{x}_p\right) \tag{C.7}$$

Linearization of the Continuity Equation at the Rod Side

The continuity equation at the rod side, given in equation (2.6) on page 7, is repeated in the top of equation (C.8). Applying the assumptions of inactive PRV, PDV and anti-cavitation system, yield the simplified system in the second line. Similar to the piston side, the stiffness of the fluid in the control volume is considered constant in the vicinity of the operation point p_{r0}. This yield the linear model in the last line of (C.8).

$$\dot{p}_r = \frac{\beta_r\left(p_r\right)}{A_r \cdot \left(L_c - x_p\right) + V_{rline}} \cdot \left(-Q_{rP} + Q_{r2} - Q_{rV} - Q_{r1} - Q_{rL} + A_r \cdot \dot{x}_p\right)$$

$\Downarrow$ Simplified model

$$\dot{p}_r = \frac{\beta_r}{A_r \cdot \left(L_c - x_p\right) + V_{rline}} \cdot \left(-Q_{rP} - C_{rLeak} \cdot p_r + A_r \cdot \dot{x}_p\right)$$

$\Downarrow$ Linearizing model

$$\Delta\dot{p}_r \approx \left.\frac{\partial f}{\partial Q_{rP}}\right|_0 \cdot \Delta Q_{rP} + \left.\frac{\partial f}{\partial p_r}\right|_0 \cdot \Delta p_r + \left.\frac{\partial f}{\partial \dot{x}_p}\right|_0 \cdot \Delta\dot{x}_p$$

$\Downarrow$ Linear model

$$\Delta\dot{p}_r = \frac{\beta_{r0}}{V_{r0}} \cdot \left(-\Delta Q_{rP} - C_{rLeak} \cdot \Delta p_r + A_r \cdot \Delta\dot{x}_p\right) \tag{C.8}$$

Linearized Pump Flow at the Piston Side

The general pump flow equation, introduced in (2.16) on page 13, is applied to the piston side of the system and given in the first line of equation (C.9). The pump flow is a function of the rotational velocity of the shaft and the differential pressure over the pump. Assuming the back pressure of the pump is constant, the differential pressure is only a function of the chamber pressure p_p. The linear model of the piston side pump flow is obtained in the third line of (C.9), by taking the partial derivatives with respect to ω_m and p_p. The volumetric efficiency of the pump is mapped by (Rexroth, 2010) from experimental test. The value of $\eta_{pv}\left(p_p, \omega_m\right)$ and the gradients are evaluated numerically, in the applied operation points, using MATLAB®, where interpolation between the measured data is utilized and the gradient is calculated numerically. To shorten the notation, the coefficients $K_{qpP\omega}$ and K_{qpPp} are introduced, containing the partial derivatives, in the linear model.

$$
\begin{aligned}
Q_{pP} &= D_p \cdot \eta_{pv}\left(p_p, \omega_m\right) \cdot \omega_m \\
&\quad \Downarrow \text{Linearizing model} \\
\Delta Q_{pP} &\approx \left.\frac{\partial Q_{pP}}{\partial \omega_m}\right|_0 \cdot \Delta\omega_m + \left.\frac{\partial Q_{pP}}{\partial p_p}\right|_0 \cdot \Delta p_p \\
&\quad \Downarrow \text{Linear model} \\
\Delta Q_{pP} &= \underbrace{D_p \cdot \left(\left.\frac{\partial \eta_{pv}}{\partial \omega_m}\right|_0 \cdot \omega_{m0} + \eta_{pv0}\left(p_{p0}, \omega_{m0}\right)\right)}_{K_{qpP\omega}} \cdot \Delta\omega_m + \underbrace{D_p \cdot \left.\frac{\partial \eta_{pv}}{\partial p_p}\right|_0 \cdot \omega_{m0}}_{K_{qpPp}} \cdot \Delta p_p \\
&\quad \Updownarrow \\
\Delta Q_{pP} &= K_{qpP\omega}\left(p_{p0}, \omega_{m0}\right) \cdot \Delta\omega_m + K_{qpPp}\left(p_{p0}, \omega_{m0}\right) \cdot \Delta p_p
\end{aligned} \tag{C.9}
$$

Linearized Pump Flow at the Rod Side

Similar to the piston side, the general pump flow in equation (2.16) from page 13, is applied to the rod side of the system. This is given in the first line of equation (C.10). The procedure, utilized to obtain the linear model, is the same as for the piston side. The partial derivatives are expressed using the coefficients $K_{qrP\omega}$ and K_{qrPp}.

$$
\begin{aligned}
Q_{rP} &= D_r \cdot \eta_{rv}\left(p_r, \omega_m\right) \cdot \omega_m \\
&\quad \Downarrow \text{Linearizing model} \\
\Delta Q_{rP} &\approx \left.\frac{\partial Q_{rP}}{\partial \omega_m}\right|_0 \cdot \Delta\omega_m + \left.\frac{\partial Q_{rP}}{\partial p_r}\right|_0 \cdot \Delta p_r \\
&\quad \Downarrow \text{Linear model} \\
\Delta Q_{rP} &= \underbrace{D_r \cdot \left(\left.\frac{\partial \eta_{rv}}{\partial \omega_m}\right|_0 \cdot \omega_{m0} + \eta_{rv0}\left(p_{r0}, \omega_{m0}\right)\right)}_{K_{qrP\omega}} \cdot \Delta\omega_m + \underbrace{D_r \cdot \left.\frac{\partial \eta_{rv}}{\partial p_r}\right|_0 \cdot \omega_{m0}}_{K_{qrPp}} \cdot \Delta p_r \\
&\quad \Updownarrow \\
\Delta Q_{rP} &= K_{qrP\omega}\left(p_{r0}, \omega_{m0}\right) \cdot \Delta\omega_m + K_{qrPp}\left(p_{r0}, \omega_{m0}\right) \cdot \Delta p_r
\end{aligned} \tag{C.10}
$$

Linearization of the Valve Flow

The general valve flow equation is given in the first line of equation (C.11). The valve flow is mapped in Rexroth (2005) and no analytical expression is available. The flow rate is therefore determined using a look-up table. The valve flow is a function of the spool position and the differential pressure. Using the gradients in either direction of the variables, the linear model is obtained in the second line of (C.11). The partial derivatives are shortened to the coefficients K_{qp} and K_{qpp}. The linear representation of the valve flow is inserted in the linear piston side continuity equation in the summary given next.

$$Q_{pV} = Q\left(x_{pV}, p_p\right)$$

$$\Downarrow \text{Linearizing model}$$

$$\Delta Q_{pV} \approx \underbrace{\left.\frac{\partial Q_{pV}}{\partial x_{pV}}\right|_0}_{K_{qp}} \cdot \Delta x_{pV} + \underbrace{\left.\frac{\partial Q_{pV}}{\partial p_p}\right|_0}_{K_{qpp}} \cdot \Delta p_p$$

$$\Downarrow \text{Linear model}$$

$$\Delta Q_{pV} = K_{qp}\left(x_{pV0}, p_{p0}\right) \cdot \Delta x_{pV} + K_{qpp}\left(x_{pV0}, p_{p0}\right) \cdot \Delta p_p \tag{C.11}$$

Summary of Linear Model

The derivation of the linear model has revealed that the SvDP-concept is rather complex with regard to linearization variables. A summary of the linear model is therefore provided to simplify the equations by collecting coefficients that depends on the same variable.

In equation (C.12) the linear representation of the cylinder force balance is repeated. The linear force balance is only a function of the operation point x_{p0}.

$$\Delta \ddot{x}_p = \frac{A_p}{M_{eq0}} \cdot \Delta p_p - \frac{A_r}{M_{eq0}} \cdot \Delta p_r - \frac{B_v}{M_{eq0}} \cdot \Delta \dot{x}_p \tag{C.12}$$

The linear model of the pressure gradient at the piston side is given in equation (C.13). Equation (C.13) is obtained by substituting the piston side pump flow and the valve flow into equation (C.7) and hereafter collecting the terms with the same linearization variable. This reveals that the change in the pressure gradient is a function of four variables, namely the operation points x_{p0}, p_{p0}, ω_{m0} and x_{pV0}.

$$\Delta \dot{p}_p = \frac{\beta_{p0}}{V_{p0}} \cdot \left(K_{qpP\omega} \cdot \Delta\omega_m - \underbrace{\left(C_{pLeak} + K_{qpp} - K_{qpPp}\right)}_{K_{pleak}} \cdot \Delta p_p - K_{qp} \cdot \Delta x_{pV} - A_p \cdot \Delta \dot{x}_p \right) \tag{C.13}$$

The same procedure is utilized for the linear model of the pressure gradient at the rod side, which is given in equation (C.13). Equation (C.13) is obtained by substituting the rod side pump flow into equation (C.8) and collecting the terms. The change in the rod side pressure gradient is a function of three variables, namely the operation points x_{p0}, p_{r0} and ω_{m0}.

$$\Delta \dot{p}_r = \frac{\beta_{r0}}{V_{r0}} \cdot \left(-K_{qrP\omega} \cdot \Delta\omega_m - \underbrace{\left(C_{rLeak} + K_{qrPp}\right)}_{K_{rleak}} \cdot \Delta p_r + A_r \cdot \Delta \dot{x}_p \right) \tag{C.14}$$

The linear representation of the dynamics of the servo system is obtained by inverse Laplace transforming equation (2.15) on page 12. This is given in equation (C.15).

$$\Delta \ddot{\omega}_m = \omega_{n,m}^2 \cdot \Delta\omega_{ref,m} - 2 \cdot \zeta_m \cdot \omega_{n,m} \cdot \Delta\dot{\omega}_m - \omega_{n,m}^2 \cdot \Delta\omega_m \tag{C.15}$$

Similarly, the dynamics of the proportional directional valve is given by a first order system, as explained in section 2.1.2. The valve dynamic is given in equation (C.16).

$$\Delta\dot{x}_{pV} \cdot \tau_{PDV} = \Delta x_{pV,ref} - \Delta x_{pV} \tag{C.16}$$

This summary concludes the derivation of the linear model. The results are utilized in chapter 5, where the linear system is analyzed.